Traceable ^{89}Zr Imaging in Positron Emission Tomography

Andrew James Fenwick

A thesis presented to the Cardiff University School of Medicine

in candidacy for the degree of Doctor of Philosophy

March 2022

National Physical Laboratory

Wales Research and Diagnostic Positron Emission Tomography Imaging Centre

Canolfan Ymchwil a Diagnosteg Delweddu Tomograffeg Allyriad Positron Cymru

Summary

Positron emission tomography (PET) is a powerful diagnostic tool in the field of nuclear medicine. The use of novel radioisotopes has significantly increased in recent years and there has been an international drive for new standards of radioactivity for radioisotopes such as ^{89}Zr. To accurately quantify radioactivity distributions in PET images it is necessary to calibrate imaging equipment and perform verification measurements. This thesis presents results from the primary activity standardisation of ^{89}Zr, measurement of a new half-life and gamma emission probabilities, and evaluation of the quantitative accuracy of PET imaging systems used for activity measurement of ^{89}Zr. The measured half-life and gamma emission intensities were evaluated alongside existing work creating a new dataset with lower uncertainties. A methodology was developed for creating traceable imaging objects to be used for calibration and verification measurements in PET imaging. Uncertainties were estimated for each stage of the measurement chain and combined where appropriate to give overall uncertainty budgets. The results showed that traceable imaging measurements are achievable in both preclinical and clinical PET systems, but uncertainty assessment is challenging when dealing with proprietary acquisition and reconstruction algorithms. Several future projects are presented, and it is hoped these projects will further develop the metrology required for traceable PET imaging in the clinical environment and open the door to a new era of accuracy and precision in PET activity quantification.

Table of Contents

Acknowledgements

This work was funded by the UK Government's Department for Business, Energy and Industrial Strategy (BEIS) through the UK's National Measurement System programmes. This work would not have been possible without the overwhelming support I received from colleagues, friends, and family. I would particularly like to thank Lee Bartley, Sean Collins, Ana Denis-Bacelar, Daniel Deidda, Kelley Ferreira, Warda Heetun, Stephen Paisey, Natasha Ramirez, Ben Russell and Andrew Robinson for their help with laboratory work, technical discussions, and advice. I would like to thank Steven Judge and Julia Snaith for giving me the opportunity and resources to complete this PhD and my supervisors Andrew Robinson, Wil Evans and Chris Marshall for their support and discussions. Finally, I would like to thank my wife, Claire, for her patience, understanding and support during the PhD.

List of supporting publications

The following publications and abstract submissions relate to specific chapters of this thesis. The primary supporting publication was published in 2020 as a peer-reviewed journal article and relates to the primary standardisation and nuclear data measurements of ^{89}Zr. Publications where the author of this thesis is not the primary author are related to this thesis but do not contribute heavily to the outcomes and are listed for reference. Articles identified as 'Abstract in conference proceedings' relate to accepted peer-reviewed abstracts given as presentations or posters at UK and international conferences.

Chapter 2:

1. Michotte, C., Nonis, M., Alekseev, I.V., Kharitonov, I.A., Tereshchenko, E.E., Zanevskiy, A.V., Keightley, J.D., **Fenwick, A.J.**, Ferreira, K., Johansson, L., Capogni, M., Carconi, P., Fazio, A., De Felice, P., 2016. Comparison of ^{18}F activity measurements at the VNIIM, NPL and the ENEA-INMRI using the SIRTI of the BIPM. Applied Radiation and Isotopes 109, 17-23.
   Contribution: Data curation, Writing - original draft, Writing - review & editing, Investigation, Formal analysis.
2. Michotte, C., Nonis, M., Bergeron, D., Cessna, J., Fitzgerald, R., Pibida, L., Zimmerman, B., **Fenwick, A.J.**, Ferreira, K., Keightley, J., 2017. Activity measurements of the radionuclides ^{18}F and ^{64}Cu for the NIST, USA in the ongoing comparisons BIPM. RI (II)-K4. F-18 and BIPM. RI (II)-K4. Cu-64. Metrologia 54.
   Contribution: Data curation, Writing - original draft, Writing - review & editing, Investigation, Formal analysis.

Chapter 3:

1. **Fenwick, A.J.**, Collins, S.M., Evans, W.D., Ferreira, K.M., Paisey, S.J., Robinson, A.P., Marshall, C., 2020. Absolute Standardisation and Determination of the Half-life and Gamma Emission Intensities of ^{89}Zr. Applied Radiation and Isotopes. Volume 166.

   Contribution: Conceptualisation, Methodology, Data curation, Writing - original draft, Writing - review & editing, Investigation, Project administration, Funding acquisition, Resources, Formal analysis.
2. **Fenwick, A.J.**, Johansson, L., Spezi, E., Evans, W. and Marshall, C. 2015. Metrology for Zr-89 in the clinic [Abstract]. European Journal of Nuclear Medicine and Molecular Imaging 42, S342-S343. [Abstract in conference proceedings]

   Conceptualisation, Methodology, Data curation, Writing - original draft, Formal analysis.

Chapter 4:

1. **Fenwick, A.J.**, Marshall, C., Spezi, E., Evans, W. and Johansson, L.C., 2015. Quantitative imaging of Zr-89 on a pre-clinical PET/CT system. Eur. J. Nucl. Med. Mol. Imag., 42, p.S415. [Abstract in conference proceedings]

   Conceptualisation, Methodology, Data curation, Writing - original draft, Formal analysis.

Chapter 5:

1. **Fenwick, A.J.,** Bartley, L., Deidda, D., Evans, W., Ferreira, K.M., Paisey, S., Robinson, A.P. and Marshall, C., 2019. Quantitative clinical imaging of Zr-89: developing the patient pathway. European Journal of Nuclear Medicine and Molecular Imaging, 46(S1), p.S744. [Abstract in conference proceedings]

   Contribution: Conceptualisation, Methodology, Data curation, Writing - original draft, Formal analysis.

Chapter 1. Introduction

1.1 Rationale

Nuclear Medicine (NM) is a powerful tool for both diagnosing and treating disease due to the flexibility of its application and the ability to image the functional processes of the body using the emissions of a radiopharmaceutical (a radionuclide labelled to a targeting vector). Its use in the clinical setting is accompanied by a series of measurements that have been steadily improved over the years and this, in turn, has led to the introduction of new radionuclides and labelling agents for an increasing number of applications. At the core of nuclear medicine are the activity measurement and imaging devices, which are used to determine how much radioactivity is injected into a patient and where the activity has been distributed following injection. The accuracy of these devices, be it in terms of activity measurement or image quality and quantification, directly affects the patient treatment path and the radiation dose received by the patient. It is, therefore, critical that the measurement chain itself is analysed to establish robust calibration procedures, determine uncertainties, and optimise measurement techniques to ensure that patient outcomes are as favourable as possible. This thesis investigates the whole measurement process for PET/CT imaging with ^{89}Zr and brings together accurate and precise activity measurements and clinical practice in a way not considered previously. The work was performed at the National Physical Laboratory (NPL) in Teddington and the Wales Research and Diagnostic PET imaging Centre (PETIC) in Cardiff, which is associated with the University Hospital of Wales (UHW), Cardiff.

1.2 Standards and the need for traceability

Since the signing of the metre convention in 1875, standard units of measure have been used by participating countries to harmonise trade and commerce. At a far more primitive level, standard units of measure have been in existence in one form or another for thousands of years to allow distribution of food, supplies or wealth within local communities, as it was quickly realised that a comparative means of measurement was

required. These standards originally took the form of physical objects that would be prepared and distributed by an authorised provider, but advances in physics have gradually led to the redefinition of the 7 key measurement units in terms of physical constants. These key units are the: metre, second, mole, ampere, kelvin, candela and kilogram. National Metrology Institutes (NMIs) around the world, in collaboration with the international bureau of weights and measures (Bureau International des Poids et Measures, BIPM), maintain the core units of measurement known as the international system of units (Système International d'Unités with the international abbreviation SI). The core SI units are used to determine all the derived SI units and, therefore, each unit (derived or otherwise) is traceable back to a physical constant. The NMIs are responsible for maintaining a link to the international community and are the reference points within their host countries. Organisations performing measurements are responsible for calibration of their measurement equipment, and the accuracy and precision required differs depending on the application. Traceability does not enforce minimum accuracy or precision limits but ensures that there is knowledge of the link between measurements made and a central standard, including the uncertainties attributed to measured values.

In modern times, it may seem that these standards are detached from everyday life. There is a relentless quest by metrology organisations to improve measurements and reduce uncertainties, and thus increase the precision and accuracy of a value beyond meaning for most. However, the core aim remains the same and was summarised nicely by the Prince of Wales upon the official opening of the UKs National Physical Laboratory (NPL) in 1900:

> *"The object of the scheme is, I understand, to bring scientific knowledge to bear practically upon our everyday industrial and commercial life, to break down the barrier between theory and practice, to effect a union between science and commerce."*

1.3 Traceability in nuclear medicine

Traceability is maintained by the international cooperation between NMIs of participating countries, and in the case of radioactivity measurement this is done through international comparison exercises or by submission to the international reference system (Système International de Référence, with the acronym 'SIR') (Ratel, 2007). The SIR was established in 1976 to provide more flexibility to the international community as to how and when it can perform comparisons, a task particularly important when considering radionuclides with short half-lives. The system is based on an ionisation chamber and response per becquerel of each source submitted (as determined by the submitting laboratory) relative to the response of a long-lived ^{226}Ra source allows determination of a response factor (akin to a calibration factor) for each laboratory (Rytz, 1978; Rytz, 1983). Results from other international comparison exercises are typically also linked to the SIR by a participating laboratory submitting a sample of the solution. The results from both international comparison exercises and SIR submissions are averaged (using either weighted or non-weighted techniques) and a Key Comparison Reference Value (KCRV) is determined. All participating laboratories are then assigned degrees of equivalence relative to this value and this forms the basis of international equivalence and is the shackle on which the chain of traceability hangs.

The chain of traceability in quantitative nuclear medicine imaging is shown in Figure 1-1 and highlights the relationship between activity measurement, nuclear data and the various clinical imaging techniques.

The starting point of the chain of traceability in a hospital is the radionuclide calibrator which is used to measure activity prior to administration and for calibration of other instruments. Following this there are three main imaging modalities: Planar gamma camera imaging, Single Photon Emission Computed Tomography (SPECT), and Positron Emission computed Tomography (PET).

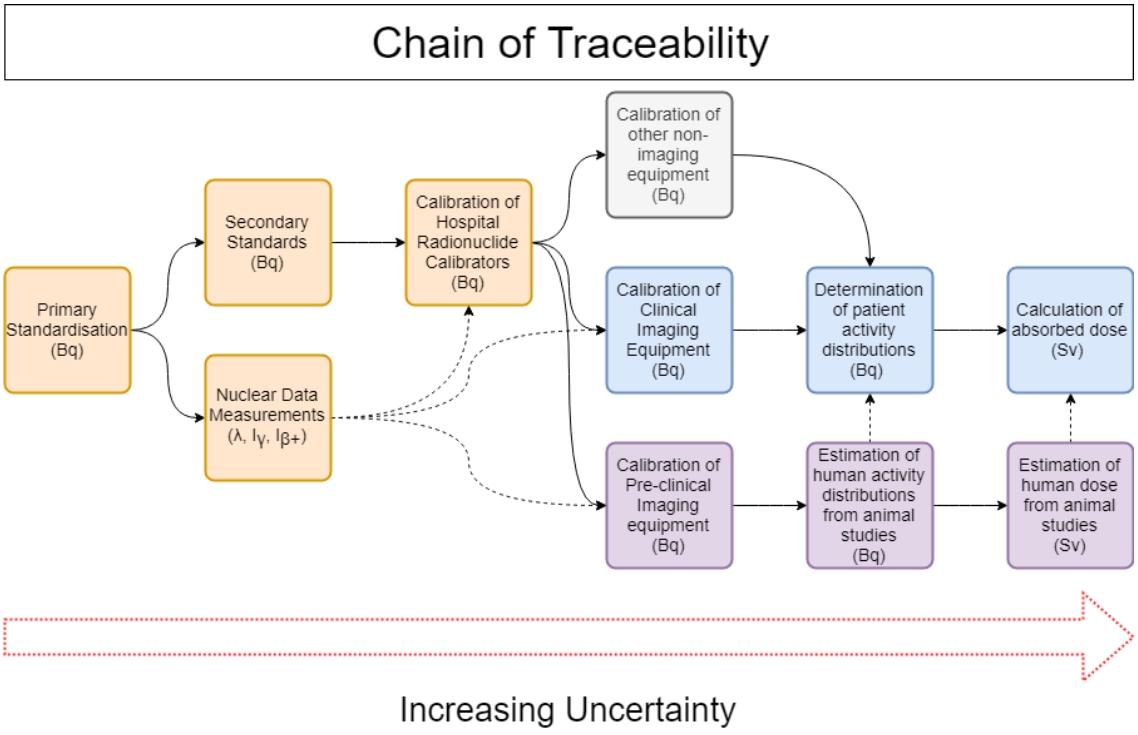

Figure 1-1: Chain of traceability in nuclear medicine

Planar gamma camera imaging, traditionally, relies on a large (approximately 0.4 m x 0.5 m) flat crystal detector optically coupled to an array of photomultiplier tubes with a lead parallel hole collimator between the detector and the object being imaged. Using Anger logic (Anger, 1958), it is possible to determine the position of interaction of incident photons on the detector and create a 2-dimensional image of the activity distribution.

SPECT uses the same detector setup and Anger logic as planar imaging but rotates the detector around the object to create a series of projections through 360º. The projections are reconstructed into a 3-dimensional representation of activity distribution using a mathematical algorithm. With SPECT it is common to include a 3-dimensional x-ray Computed Tomography (CT) image which allows visualisation of activity within the anatomy and provides information to correct the image for scatter and attenuation. To reduce measurement time, it is common for a SPECT camera to have 2 or more detectors. Both planer and SPECT imaging use single photon emitting radionuclides such as ^{99m}Tc.

PET uses a ring of scintillation crystals to detect the photon emissions generated during the annihilation of a positron and electron. Photons emitted during annihilation travel directly away from each other (at 180º angle) and therefore it is possible to identify lines of response (LORs) by looking at coincidence detections across the ring. The LORs can be combined to generate positional information. As with SPECT, a 3-dimensional activity distribution can be generated using mathematical reconstruction algorithms and combination with a CT enables anatomical visualisation and correction for attenuation and scatter.

In the case of all nuclear medicine imaging modalities it is common for calibration and quality assurance measurements to be performed using a single radionuclide. If other radionuclides are used, these typically rely on corrections derived from published nuclear data. The goal for diagnostic imaging techniques is, typically, to determine an activity distribution (or uptake) within a patient by imaging a radionuclide labelled to a specific targeting vector. The most used radioisotope in planar and SPECT imaging is ^{99m}Tc and in PET it is ^{18}F. The chain of traceability for these radionuclides up to the point of patient administration is well defined, with clinical sites performing calibrations of measurement equipment in a traceable manner. The traceability of imaging is less clearly defined with individual clinical sites devising in-house methods for image quantification. This break in the traceability chain continues through to patient dose calculations with no clearly defined standards or methodology for performing these measurements.

The goal with therapeutic nuclear medicine, which may or may not involve imaging procedures, is to deliver a radioactive dose to a specific region within a patient. In this instance it is good practice to determine activity distributions following administration to confirm that the desired dose is being delivered to the target. Ideally this is performed using an imaging technique. With some long-established procedures, such as radioactive iodine therapy, radioactivity counting equipment is sometimes used to confirm administration and for measuring external dose-rates prior to patient discharge.

The chain of traceability for commonly used radionuclides, such as ^{131}I, is well defined up to the point of patient administration. As with diagnostic imaging, the traceability chain beyond this point is poorly defined, with a variety of methods employed to determine activity distributions and radiation dose delivered.

A key component of traceability is uncertainty, and methods for determining uncertainty budgets are described in the Guide to Uncertainty in Measurement (GUM) (BIPM et al., 2008). Uncertainty propagation in nuclear medicine is one of the main limitations to performing traceable imaging measurements. Uncertainty is clearly propagated through the chain until the point of patient administration. However, once imaging equipment is introduced to the chain it becomes difficult to construct meaningful uncertainty budgets due to the black-box nature of vendor-specific software in use. In addition, imaging systems are very complex, and the determination of an accurate uncertainty budget becomes impractical for individual clinical sites.

All new radiopharmaceuticals must undergo pre-clinical trials prior to release in human studies. The purpose of the trials is to determine safety and efficacy of the product. Since information from the pre-clinical studies is used in human studies, it is important that traceability is considered throughout the process.

1.4 Clinical trials and radiopharmaceutical development

Traceability is required as part of the development of any radiopharmaceutical to allow progression from basic research to clinical implementation. In order to bring a new drug of any type into regular use, organisations such as the Food and Drug Administration (FDA) and European Medicines Agency (EMA) require a system of trial phases to be followed in order to monitor safety and efficacy (USDoH, 2014). The typical process for development of a new radiopharmaceutical is shown in Figure 1-2.

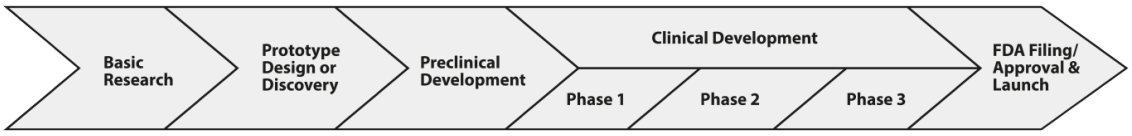

Figure 1-2: New radiopharmaceutical development process

During basic research, prototyping and development, it is common for manufacturers to use non-traceable activity measurements, such as those obtained through gamma spectrometry or estimated radionuclide calibrator dial settings, to speed development. This would seem to be a false economy, since eventually they will almost certainly be required to revisit this work to establish traceability. These early stages often rely on comparative measurements rather than absolute determinations of activity distributions. Thus traceability at this stage is less likely to affect the overall outcomes of the testing, but uncertainty should still be assessed. Upon entering pre-clinical or clinical studies, it becomes more important to ensure that the measurement equipment is traceable to allow multi-device or multi-centre trails. Without traceability or comparability, the results from such trials can be difficult to interpret and ultimately could lead to a new product being withdrawn. Finally the EMA, FDA and other authorising bodies such as the Medicines and Healthcare products Regulatory Agency (MHRA), will require drug development companies, and clinical sites that use the product, to demonstrate traceability of the product being administered, and will look to see that good practice is used throughout the development and measurement chain.

Due to recent interest and a lack of existing standards, the positron-emitting radionuclide ^{89}Zr was chosen as a focus for this investigation. There has been widespread interest in ^{89}Zr as a labelling agent for radiopharmaceuticals used in clinical trials, as PET imaging is a useful tool for quantitative and qualitative assessment (Börjesson et al., 2006; Dejesus and Nickles, 1990; Kaalep et al., 2018a; McKnight and Viola-Villegas, 2018; Meijs et al., 1994). Applications involving ^{89}Zr labelled monoclonal antibodies (mAbs) show particular promise, mainly due to the fact that the relatively long physical half-life of ^{89}Zr (78.4h) accommodates mAbs uptake time of 2-8 days (Deri et al., 2013;

Svensson, 2008). Allowing radiolabelled mAbs to be tracked throughout the subject over several days can be invaluable in demonstrating the efficacy of mAbs and for monitoring long-term stability of the product in vitro. In addition, bio-kinetic uptake and retention rates can be established to determine effective doses better. The main phases of a clinical trial are discussed below, along with a comment on how traceability fits in at each stage.

1.4.1 Early phase trials

Phase 0 and 1 trials investigate the safety of a product (not the therapeutic or diagnostic effect) and establish if it is performing as designed (i.e. travelling to anatomical sites of interest) before larger randomised groups are exposed to the drug. Often phase 0 trails are incorporated into the early stages of a phase 1 trial for practical reasons. The first human trials using ^{89}Zr were undertaken between 2003 and 2005 (Börjesson et al., 2006) and investigated the diagnostic usefulness of imaging patients with head and neck carcinomas (HNSCC) using the chimeric mAb U36. The results of these studies showed that PET imaging using this technique had marginally better diagnostic accuracy than CT/MRI for this condition, and that no excessive radiation doses were received by the patients undergoing imaging. Since this initial trial, several further studies have begun across Europe investigating the potential of ^{89}Zr labelled mAbs. At the time of these trials, no activity standard for ^{89}Zr was available and, therefore, they relied on activity measurements using estimated calibration factors and nuclear data. This introduces an unknown element to the established safety margins and may lead to either under or over administration of activity to animals and patients in future studies, which may affect the efficacy of the product.

1.4.2 Phase 2 trials

Following a successful phase 1 trial, the drug may proceed to phase 2 to establish therapeutic effectiveness or diagnostic efficacy, and determine radiation dose values. These trials involve a larger number of patients who are specifically selected, generally

because they have the disease under investigation. The trials often involve the use of placebo drugs in some of the patients to create a control group, and are critical in establishing a reference dataset for the drug. There are ongoing phase 2 trials involving ^{89}Zr labelled antibodies for the treatment of prostate cancer and esophagogastric cancer, in which the treatment potential of the antibody therapy is under investigation alongside the imaging benefits of ^{89}Zr (Adams et al., 2019; Allred et al., 2021; McKnight and Viola-Villegas, 2018). The lack of standardisation and traceability in activity administration and imaging during this phase can lead to incorrect conclusions being drawn from the results. Without accurate knowledge of administered activity, the outcomes cannot be attributed to a specific administered activity, which may hamper the continuing development of a drug. Inaccurate knowledge of activity distributions may also lead to incorrect conclusions being drawn regarding efficacy.

1.4.3 Phase 3 trails and release

Phase 3 trials involve upscaling administration of the drug to thousands of patients from multiple sites and countries in order to fully establish the benefits of the new drug. The drug will be trialled alongside existing treatments (or placebos) in order to establish any benefits or limitations, and to better understand the administration requirements, effectiveness and side effects. If the outcomes from phase 3 are favourable, the drug will be filed for release with the relevant agencies and will become commercially available for general use by physicians. Phase 3 represents a large increase in use of the drug and, therefore, establishing traceability chains becomes more difficult, time consuming and complex. There are a few phase 3 clinical trials involving ^{89}Zr labelled antibodies, targeted at kidney disease and lung disease, but outcomes are yet to be published (TELIX, 2021). At this stage, the lack of standardisation and comparability is critical as it becomes increasingly difficult to draw meaningful conclusions from multiple sites which may have entirely different methods for measuring activity and performing imaging. It is not uncommon in trials to have different results between sites and countries due to

cultural or lifestyle differences as highlighted by the FDA and EMA in 2019 (Schwarz and Decristoforo, 2019). However, if there is no common basis for the measurements being performed, interpreting these differences can be difficult and harmonisation is required. Differences in the available equipment and local practices between sites also play a role in the outcomes, and this is where the uncertainties on each measurement need to be assessed to allow meaningful comparison of results.

1.5 Overview of aim and objectives

The primary aim of this thesis is to link measurements of activity distributions within patients being treated in a clinical environment with the absolute realisation of the becquerel. This is approached by starting at the top of the chain of traceability (the realisation of the becquerel) and considering each transfer measurement between this first stage and the final imaging of patients using PET. Specific objectives are summarised below:

- Primary activity standardisation of ^{89}Zr.
- Measurement and evaluation of half-life and γ-emission probabilities.
- Determination of transfer standards (secondary standards) for clinical use.
- Verification of a pre-clinical imaging system for quantification of ^{89}Zr.
- Verification of a clinical imaging system for quantification of ^{89}Zr.
- Outlining methodologies for establishing realistic uncertainty budgets for imaging systems.
- Assessment of uncertainty propagation throughout measurement chain.

This work is focussed on ^{89}Zr as an example, but much of the methodology can be transferred to other radionuclides of interest.

1.6 Contents

This thesis introduces some underlying concepts before progressing to address each step in the measurement chain, beginning with the primary standardisation. The primary

standardisation was performed using several methods to provide additional confidence in the results, and lead to the development of secondary standard calibration factors for NPL equipment as well as commercially available radionuclide calibrators and those used at the PETIC facility. Nuclear data are addressed at this point and new measurements of the ^{89}Zr half-life and gamma emission intensities presented; these are used extensively in Monte Carlo simulation and activity determination using spectroscopic techniques are presented. The nuclear data were evaluated alongside existing measurements and new recommended values presented along with revised uncertainties.

Imaging is discussed in the next section of the thesis, beginning with pre-clinical applications. Using the primary and secondary standards developed earlier, measurements of phantoms were performed on a pre-clinical scanner at the PETIC facility to assess the precision and accuracy of the manufacturer's reconstruction and calibration processes. This included methods for accurate and precise filling of phantoms used in the experiments. The imaging work is continued onto two clinical imaging systems, one based at PETIC and the other at NPL.

Uncertainties are a critical part of traceability and these are addressed alongside all of the results in a general discussion section. Recommendations for future work are also presented.

Chapter 2: Underlying concepts

2.1 Introduction

The underlying physical concepts supporting the work in this thesis are presented in this chapter. This is by no means an exhaustive explanation of each concept but is meant as

an introduction to important processes to which reference will be made in later chapters of this work. For further information, excellent books are available such as those by Knoll (2010) and Tsoulfanidis and Landsberger (2015).

2.2 Properties of radioactivity

Radioactive decay is a naturally occurring random process discovered by Henri Becquerel in 1896 whilst investigating the recently discovered 'x-rays' produced and detected by Wilhelm Röntgen the previous year. Marie Curie and her husband Pierre performed much of the initial investigative work on the properties of radiations emanating from ore material, eventually separating polonium and radium as identifiable elements in the following years. Ernest Rutherford is credited with truly identifying the main types of radioactive emission – alpha, beta and gamma particles, and determining this classification system based primarily on the interaction of these emissions with matter.

The interaction properties are ultimately what makes radioactivity a useful tool in the field of nuclear medicine, allowing diagnosis, treatment and staging of disease through functional imaging techniques or non-imaging particle and photon counting measurements. In therapeutic applications, radiation with a high linear energy transfer (such as alpha and beta) is desirable to cause maximum damage to a targeted area of the body whilst minimising damage to surrounding tissue. Gamma and x-ray emissions are used extensively for the diagnosis or staging of diseases ranging from cancerous tumours to kidney failure. Regardless of the application, it is important to monitor and control the radiation dose to patients, staff and members of the public, not only to deliver successful treatment or diagnosis, but also to maintain safety and adherence to legislation.

2.2.1 Radioactive decay

At the individual atomic level, radioactive decay is a random process and it is impossible to determine when a specific atom will decay. The decay constant (which is unique to

each radionuclide) is the a probability per unit time that an atom will decay and is assigned the symbol λ. The decay constant applies to all atoms of a species of radionuclide and is not affected by the number of atoms present or the age of the atoms. The number of atoms of an element (N) is given by Avagadros number (N_A) multiplied by the ratio of the mass (M) and the atomic weight (A_r) as shown in Equation 2-1.

$$N = N_A \frac{M}{A_r}$$

Equation 2-1

During decay, the number of atoms of a particular radioactive element decreases as a function of time, which is governed by the decay constant. Therefore, we can express N at a given time t as a differential in Equation 2-2.

$$-\frac{dN_t}{dt} = \lambda N_t$$

Equation 2-2

This can be solved to give Equation 2-3, in which N_t is the number of atoms at the reference time t, and N_0 is the number of atoms at time zero.

$$N_t = N_0 e^{-\lambda t}$$

Equation 2-3

This equation is used extensively in all aspects of radionuclide applications in order to relate measurements performed at different times. A common concept in radiation measurement is the half-life ($T_{1/2}$), which is the time taken for half of the atoms of a particular radionuclide to decay. Using Equation 2-3, the relationship between $T_{1/2}$ and λ can be demonstrated and is shown in Equation 2-4 and Equation 2-5.

$$\frac{N_t}{N_0} = \frac{1}{2} = e^{-\lambda T_{1/2}}$$

Equation 2-4

$$\lambda = \frac{\ln 2}{T_{1/2}}$$

Equation 2-5

The rate of decay referred in Equation 2-2 is known as the radioactivity (often shortened to activity) of a sample and has the units of the becquerel (Bq), which is described later in section 2.5. The activity (A) at a given time is therefore related to the number of atoms at the same time by the decay constant as shown in Equation 2-6.

$$A_t = \lambda N_t$$

Equation 2-6

In some instances, the daughter of a parent radionuclide is also radioactive. The work undertaken by Bateman (1910) describes the differential equations required to calculate N (or A) for each radionuclide in the decay chain.

2.2.2 Modes of decay

The main modes of decay relevant to this thesis are discussed briefly below. Further information can be found from many sources, but a good concise description of all of these processes is given by Knoll (Knoll, 2010).

2.2.2.1 Alpha

$$^{A}_{Z}X \rightarrow ^{A-4}_{Z-2}Y + ^{4}_{2}He^{2+}$$

Equation 2-7: Alpha decay

Alpha decay can be described as the emission of a helium nucleus (two protons and two neutrons) from the parent nucleus through electromagnetic (Coulomb) repulsion by means of quantum tunnelling (Equation 2-7 and Figure 2-1). Typically, the emitted alpha particle has very high energy (several MeV) and travels at approximately 5 % the speed of light. The alpha particle quickly slows in matter, depositing energy as it travels, and so this type of emission is favourable for therapeutic applications. The short range also leads to limited dose to surrounding tissue provided the labelling agent used has a high specificity for the target. The only alpha emitting radionuclide currently used routinely in nuclear medicine, ^{223}Ra, has a long chain of alpha, beta and gamma emitting progeny

before reaching a stable nucleus. This has the potential benefit of providing an increased dose rate, but can lead to labelling problems due the different chemistries of the progeny. Uptake in healthy tissue will lead to significant damage due to the high linear energy transfer. Typically, alpha decay is accompanied by x-ray and gamma emissions due to isomeric transitions in the daughter atom. The gamma emissions can potentially be advantageous for imaging or measurement purposes. Current clinical therapeutic administrations use relatively low activity (few MBq), which can lead to poor counting statistics using conventional detection and imaging equipment.

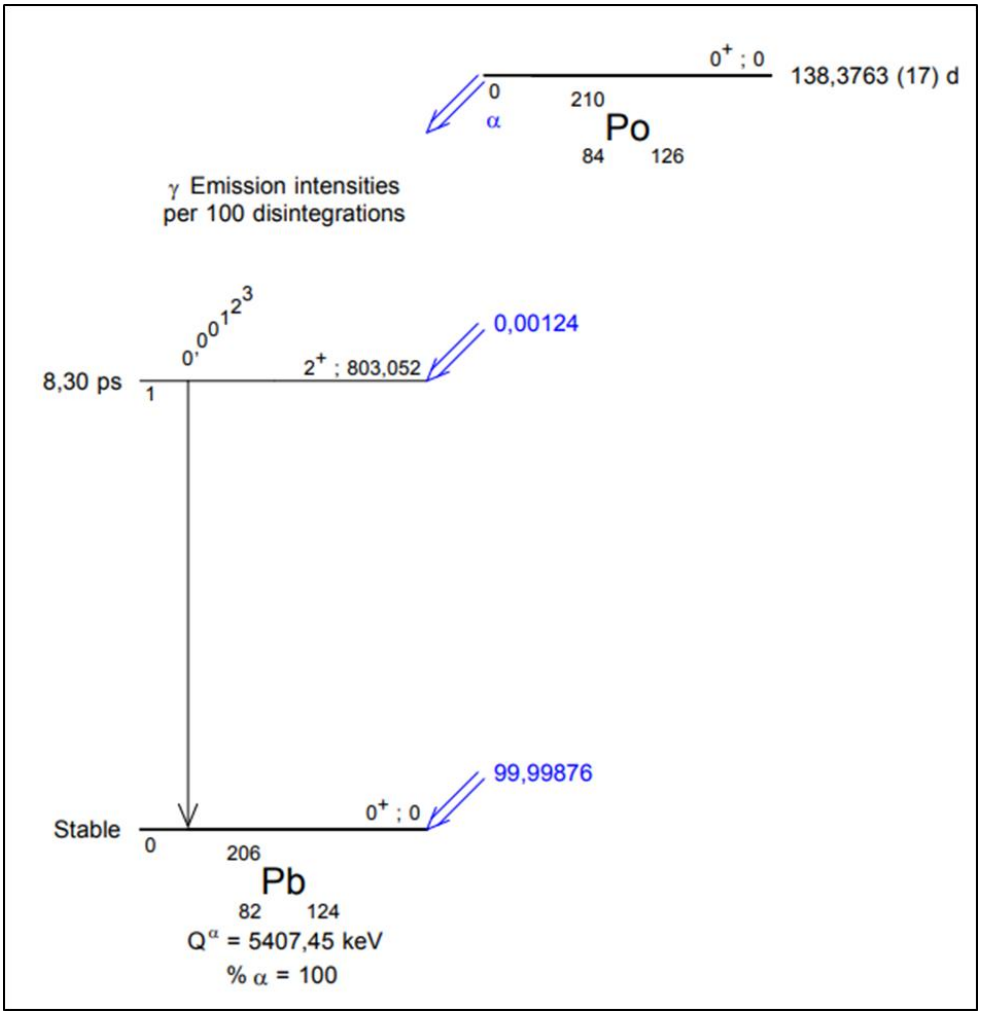

Figure 2-1: Alpha decay scheme of ^{210}Po (Bé et al., 2008).

2.2.2.2 Beta-minus (β^-)

$$ {}^{A}_{Z}X \rightarrow {}^{A}_{Z+1}Y + e^- + \overline{\nu_e} $$

Equation 2-8: Beta-minus decay

Beta-minus decay (generally referred to as beta decay) is characterised by the emission of an electron (beta-minus particle) and an antineutrino from the parent nucleus (Equation 2-8 and Figure 2-2). This process occurs due to a neutron ‘decaying’ to a proton by the creation of an electron in order to change the ratio of protons to neutrons in the nucleus. It is important to note that the electron is always created in the nucleus during beta decay and is not taken from the surrounding electron cloud. During the decay process, an antineutrino is created to balance the lepton number of the resulting proton. The total energy of the decay is shared between the created particles and the atomic recoil, which leads to the characteristic continuous beta spectrum that is observed in this type of decay (Figure 2-3). In nuclear medicine, high energy beta emitters (approximately 100 keV – 3 MeV) are used routinely for the treatment of cancers and other ailments. The relatively short range (typically of a few mm, which is energy dependent) allows for high radiation doses to be targeted in small areas, thus limiting dose to surrounding healthy tissue. Therapeutic radionuclides used in nuclear medicine often do not have significant gamma emissions; therefore, imaging activity distribution following administration can be challenging.

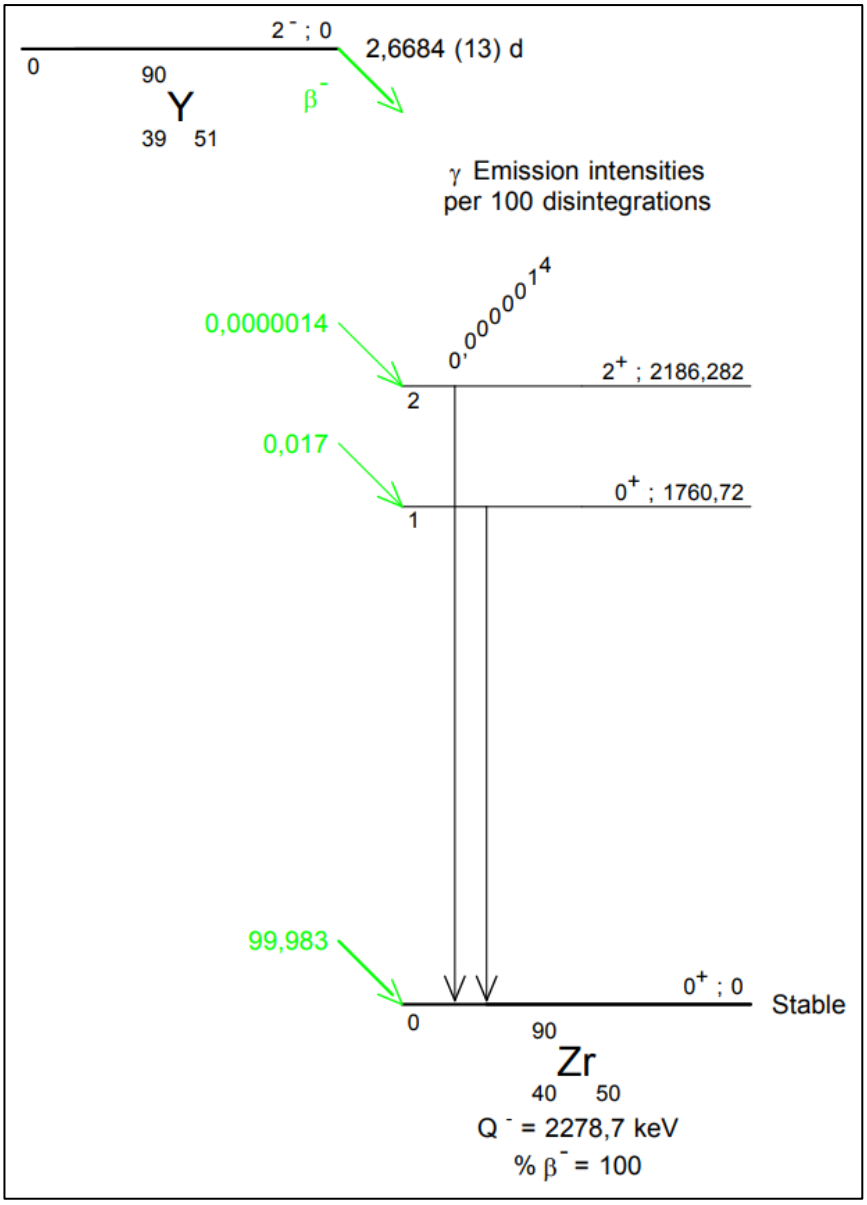

Figure 2-2: Decay scheme of 90Y (Bé et al., 2006)

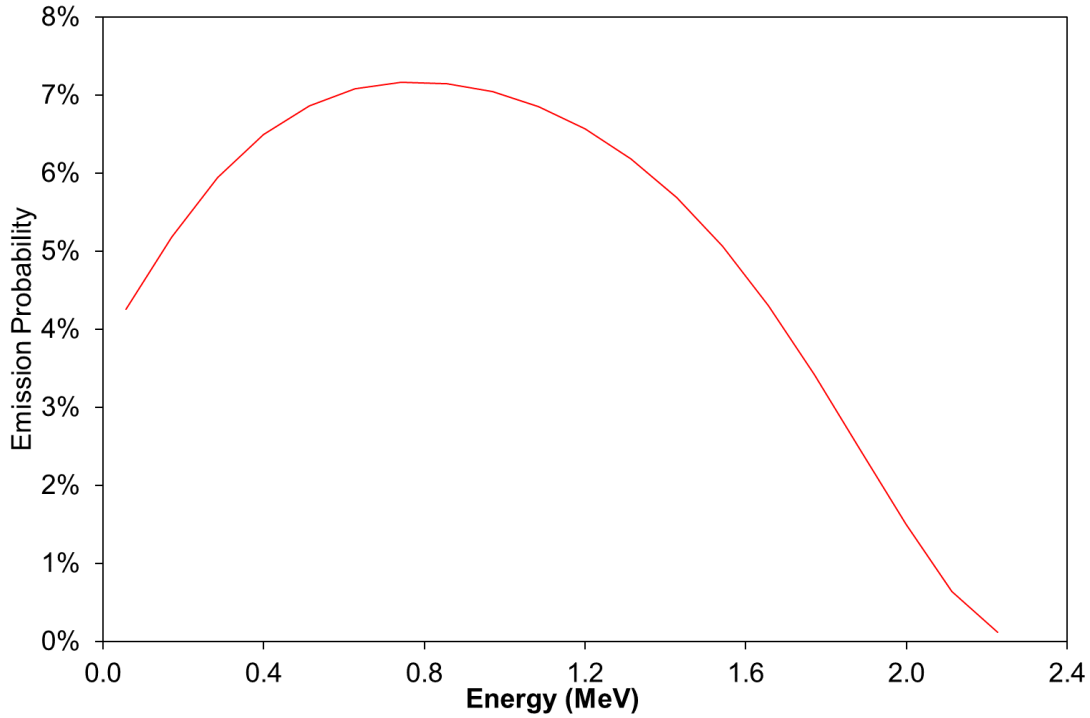

Figure 2-3: Example of beta energy spectrum for ^{90}Y (Eckerman et al., 1994)

2.2.2.3 Positron (β^+)

$$ {}^{A}_{Z}X \rightarrow {}_{Z-1}{}^{A}Y + e^{+} + v_e $$

Equation 2-9: Positron decay

Positron decay occurs when a proton decays to a neutron by the creation and emission of a positive electron (a positron or beta-plus particle) along with an accompanying neutrino to balance the lepton numbers of the neutron (Equation 2-9 and Figure 2-4). A positron is the anti-particle of an electron (in the same way an anti-neutrino is the anti-particle of a neutrino) and, therefore, when a positron comes into contact with an electron, annihilation occurs. The combined mass of the particles is converted to energy, E, in accordance with Einstein's Law. In this case, $E = 2m_0c^2$ due to both particles having the same rest mass m_0, equivalent to 511 keV. This energy is typically released in the form of two gamma rays, each of energy 511 keV, emitted at 180° (in opposite directions) to conserve momentum. If either particle has significant kinetic energy upon annihilation, this energy is added to the total emitted photon energy and can lead to

emission angles other than 180°. Since β^- and β^+ decay occur in a similar fashion, the positrons also exhibit a similar characteristic beta spectrum (Figure 2-5).

Positrons may also be created through internal pair production, in which an electron and positron are created rather than the emission of a photon (the transition energy must be greater than 1.022 MeV). An example of this type of positron production occurs in the decay of ^{90}Y, which has a low intensity (0.017 %) beta decay to an excited level in ^{90}Zr. This level has a spin value of 0+, which matches the ground state of ^{90}Zr and, therefore, single photon emission is forbidden. In order to transition to the ground state, it is necessary to either undergo internal pair production, internal conversion of an orbital electron or, in some very rare cases, the emission of a double photon. For ^{90}Y, there have been many studies showing the observation of a small but measurable 511 keV positron signal (D'Arienzo, 2013; Selwyn et al., 2007).

Positrons travel through matter in a similar fashion to electrons and, therefore, annihilation and the subsequent gamma emissions are not localised close to the decaying atom. Positron emission computed tomography is one of the leading diagnostic tools and is discussed further in section 2.7.

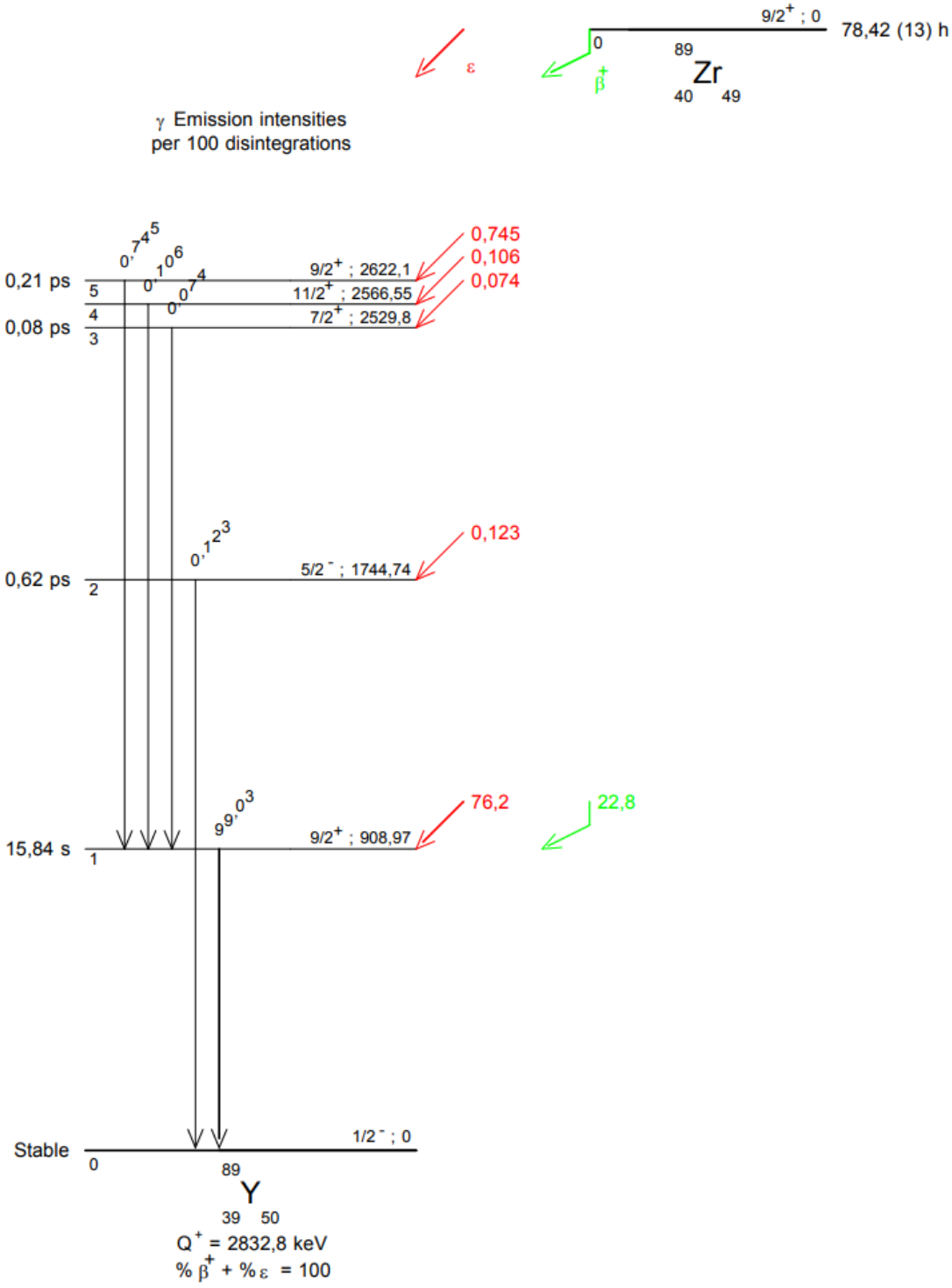

Figure 2-4: Decay scheme of ^{89}Zr (Bé et al., 2016)

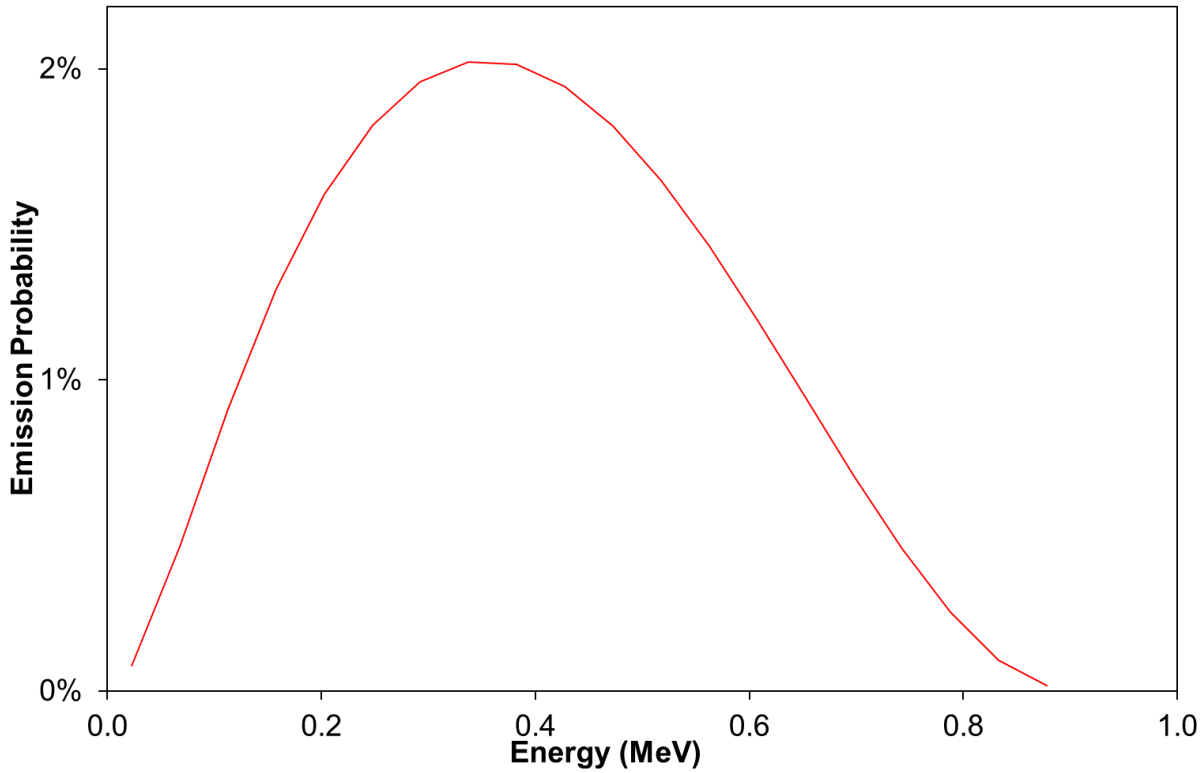

Figure 2-5: Example of beta spectrum for ^{89}Zr (Eckerman et al., 1994)

2.2.2.4 Electron capture

$$ {}^{A}_{Z}X + e^{-} \rightarrow {}^{A}_{Z-1}Y + v_e $$

Equation 2-10: Electron Capture decay

Electron capture occurs when the parent atom has an abundance of protons in the nucleus and utilises one of its own orbital electrons, typically from the K- or L- orbitals, in order to convert a proton to a neutron whilst generating a neutrino in order to balance the lepton number (Equation 2-10 and Figure 2-4). Electron capture operates in competition with positron decay, with both processes commonly found in the same nuclear decay scheme. The subsequent electron shell rearrangement and isomeric transitions of the daughter atom lead to x-rays or gamma rays being emitted, and in some cases the emission of an Auger or conversion electrons (as with other modes of decay). Whilst electron capture in itself does not yield any therapeutically beneficial emissions, secondary emissions such as Auger or conversion electrons may cause damage to

surrounding tissue. The gamma emissions from the isomeric transitions that often follow electron capture decay can also be used for imaging purposes.

2.2.2.5 Isomeric transition

Following radioactive decay, the daughter nucleus may be left in an excited state and must undergo some form of isometric transition to reach the ground state. There are two main types of isomeric transition; gamma emission and internal conversion.

Gamma emission is the creation of a photon from the abundant energy in an excited state of the daughter nucleus. Gamma emissions have specific energy, which is governed by the energy levels within the nucleus from which it was created. The gamma transition may or may not return the atom to the ground state, and in many cases there will be several sequential gamma decay paths that may be considered. Photons are highly penetrating and, therefore, are of limited use as a therapeutic agent. However, their large range allows detection outside the body, which makes them valuable as an imaging agent. Typically, low energy gamma emitters are used in nuclear medicine applications (10's or 100's of keV) as this minimises absorbed dose to patients whilst giving good sensitivity on imaging equipment.

Internal conversion is a process in which, rather than emitting a photon, the atom emits an orbital electron (known as a conversion electron) with an energy determined by the transition energy minus the binding energy of the electron. This process obviously effects the emission probability of the gamma photons and can interfere with counting experiments. Where present, conversion electrons are also visible on the beta-spectra, and should be considered in absorbed dose calculations.

Other modes of isomeric transition are rare, but include internal pair production and double gamma emission which are mentioned in 2.2.2.3.

2.3 Radiation interactions

Radiation interacts with matter in different ways depending on the type of emission, the energy of the emitted particle and the properties of the material with which it is interacting. These interactions are critical to the detection of radiation, and to the use of radionuclides as therapeutic agents. Typically, heavy charged particles such as fission fragments or alpha particles will travel a short distance and deposit a large amount of energy, whereas uncharged particles, such as gamma rays, will deposit their energy over a larger distance and travel further through materials.

2.3.1 Photon Interactions

There are four main types of photon interaction with matter: Rayleigh scattering, Compton scattering, the photoelectric effect and pair production.

Rayleigh (also referred to as Thompson, coherent, or classical) scattering is an elastic scattering process that typically involves a particle much smaller than the wavelength of the incident photon. This process is dominant in gasses, but can also be observed in liquids and solids.

Compton scattering occurs when an incident photon collides with an electron and is deflected from its incident path, losing energy during the process. A photon may undergo several Compton scattering events before losing all of its energy or interacting in another way.

The photoelectric effect is probably the most well-known photon interaction. As the name suggests, the process involves an incident photon being ‘converted’ into an electron by giving all its energy to an electron from the atomic orbitals. If this electron is given enough energy to overcome the binding energy, it is emitted from the atom and an electron in a higher orbital will fill the vacancy, emitting secondary photons in the process. This interaction is most likely to occur at relatively low incident energies and only occurs if the frequency of the incident photon is greater than the threshold frequency for the material.

Pair production can only occur if the incident photon has an energy of more than twice the rest mass of an electron (1.022 MeV). In pair production, the photon interacts with the atomic nucleus and converts all its energy into an electron and a positron. This is a similar process to internal pair production as discussed in 2.2.2.3; however, the energy is provided by an external photon rather than internal excitation.

2.3.2 Electron interactions

Charged particles such as electrons generally interact with matter through Coulomb interaction, the emission of bremsstrahlung (braking) radiation or the emission of Cerenkov radiation.

Coulomb interaction is the interaction of a charged particle with either the atomic nucleus or the surrounding electron cloud. Due to the size of the nucleus relative to the size of the orbital electron cloud, it is far more likely that the interaction is between the incoming particle and the electron cloud. In this case, as the fast-moving electron approaches close to the orbiting electron, it is repelled due to the negative charge. During this process, energy is transferred to the orbital electron. This transfer of energy not only slows the incoming particle but can cause excitation, in which the orbital electron moves to a vacant quantum state in a higher orbit, or ionisation, in which the orbital electron gains sufficient energy to completely escape the host atom and become a free particle. During excitation, the orbital electron will quickly return to a lower energy level (assuming one is available) and emit surplus energy in the form of an x-ray. An ionised atom will remain ionised until it can collect a free electron from its surroundings and return to neutrality. Since the energy transfer in the case of excitation is relatively small, many interactions can take place before the incoming electron is stopped.

As a high-energy electron is slowed in a material, it may emit bremsstrahlung radiation, which consists of a spectrum of photons. The amount of bremsstrahlung produced is

dependent on the density of a material and Coulomb force between the material and incoming particle.

The Cherenkov phenomenon is credited to Pavel Cherenkov, who gained the Nobel Prize in Physics in 1958 for its discovery. However, it was observed (if not explained) by Marie Curie as far back as 1910. If an electron is travelling faster than the speed of light in the medium through which it is passing, Cherenkov light may be produced. This is characterised by a directional continuous spectral shock-wave focussed in the ultra-violet region. Whilst the amount of kinetic energy lost through this process is small, it can be useful in radiation counting experiments and is often visible to the human eye in high particle flux environments such as nuclear reactors.

2.3.3 Positron interactions

Energetic positrons interact with matter in much the same way as electrons (described in 2.3.2) and their track through matter is essentially the same. The principal difference occurs when the positron encounters an electron after it has lost most of its kinetic energy. This leads to annihilation and the emission of photons whose total energy is equivalent to the mass of the positron and the electron. Typically, two 511 keV photons are emitted at approximately 180º, which forms the basis for PET imaging. It is important to note that this interaction occurs some distance from the atom from which the positron originated, and the energy of the emitted positron along with the material composition dictates the distance from the starting atom. This ‘spreading’ effect has implications for image quality in PET and must be considered when calibrating counting equipment which relies on known geometries.

2.4 Radiation dose

Radiation dose is a relatively simple concept which defines the amount of energy deposited into a medium during the interactions mentioned in 2.3. In practice, radiation dose is a complex field due to the relationship between energy deposited and biological

impact. There are three main definitions of radiation dose which are: absorbed dose, equivalent dose and effective dose. Absorbed dose is defined as the amount of energy, in Joules, deposited per unit mass of an object. This can be used in vitro and in vivo as there is no relation to biological outcome considered. Absorbed dose is the measurable quantity of radiation dose and is used to determine equivalent or effective doses. Equivalent dose is the absorbed dose to a specific organ, multiplied by a scaling factor to account for the biological effect. The scaling factor relates to the biological damage likely to be caused by the specific type of incident radiation on a specific organ. Effective dose is the sum of equivalent doses throughout an individual (whole body dose).

2.5 Units

The units for radioactivity and radiation absorbed dose are distinct and are not directly interchangeable. In common colloquial use, a term such as ‘dose’ may be used to refer to a pharmaceutical dose and, in the clinical setting, this has become a common expression when prescribing an activity to be administered to a patient (in becquerels). This unfortunate practice has become so engrained in the culture of nuclear medicine that it is common to refer to the instruments used to measure activity as ‘dose calibrators’ when, in fact, all the devices can measure is the activity. To avoid ambiguity these devices should be referred to as a Radionuclide Calibrator (RC) or activity meter. It is important that the correct units are observed for the sake of clarity. Further information regarding SI units can be found by consulting the SI brochure published by BIPM (BIPM, 2006).

2.5.1 Becquerel

The becquerel (Bq) is the SI unit of measurement for radioactivity. It is defined as the inverse of the second and denotes the number of disintegrations per unit time (Equation 2-11). This unit, when expressed in SI base units (s^{-1}), could be confused with the unit for frequency (Hz). However, hertz is used only for periodic phenomena whereas the becquerel is reserved for the stochastic process observed in radioactive decay. In

nuclear medicine, patients are generally administered with activities in the order of 10^6 or 10^9 Bq (MBq or GBq respectively).

$$Bq = \frac{Nuclear\ Disintegrations}{s} = \frac{1}{s} = s^{-1}$$

Equation 2-11: Definition of the Becquerel

2.5.2 Gray and sievert

Absorbed dose and equivalent dose are both expressed in units of energy deposited per unit mass called the gray (Gy) and sievert (Sv) respectively (Equation 2-12). The important difference that the sievert is scaled using a multiplicative factor that depends relative biological effectiveness of the radiation to the tissue into which the energy is deposited (Equation 2-13). The gray and sievert, when considered in terms of dose to tissue, are large units and studies have shown that the median lethal instantaneous dose to a whole body exposure is 3 Gy (Levin et al., 1992).

$$Gy = \frac{J}{Kg}$$

Equation 2-12: Definition of the gray (absorbed dose)

$$Dose\ Equivalent\ (Sv) = Q \cdot Absorbed\ dose\ (Gy)$$

Equation 2-13: Definition of the sievert where Q is a dimensionless scaling factor

2.6 Measurement of radioactivity

Radioactivity can be observed using a variety of methods, which are dependent on the emission type. A brief description of the detectors of interest in this thesis are presented as an overview. For a more thorough description of each of these detector types, books by Knoll (2010) and Tsoulfanidis and Landsberger (2015) are recommended.

2.6.1 Gas detectors

Gas detectors were among the earliest radiation detectors, mostly due to the simplicity of their construction and operation. All gas detectors operate on the basis of the measurement of electron-ion pairs created through ionisation of a counting gas. Once these particles reach the anode or cathode, they can be measured as a current to indicate a time-averaged count rate or converted into electrical pulses to count individual particles. Gas detectors have a distinctive relationship between voltage applied between the electrodes and the number of ion pairs collected for a given activity, as shown in Figure 2-6. This characteristic is important as it allows gas detectors to be operated in 5 different regions simply by changing the voltage. As the voltage is increased across the gas, the electrons and ions are subject to greater acceleration towards the anode and cathode respectively, and they may recombine, continue unaffected or to cause secondary ionisations. The three curves on the figure denote different incident particle energies and demonstrate the proportional nature of some of the regions of the gas counting system.

Regions 1-3 marked in Figure 2-6 all share the characteristic that the output signal is directly proportional to the energy deposited in the gas and may be used to provide an energy spectrum or identify particle types. Region 4 (the Geiger-Müller region) simply outputs a signal provided sufficient energy was deposited to cause a single ionisation and will only indicate particle flux. Region 5 indicates a state of continuous discharge following a single ionisation and the system therefore ceases to be a detector. Region 1 is known as the recombination region due to the slow-moving ionised particles having time to interact and recombine before being counted. This region is not generally used for radiation detectors as the output signal is very small and small variations in bias voltage will lead to significant changes in output. Region 2 is known as the ionisation region, in which the output of the detector remains constant despite small changes in the voltage. Within this region there is no recombination or secondary ionisation and the

output is directly proportional to the energy deposited. Depending on the design of the detector, when operated in this region it is possible to distinguish between particles by the size of the output signal. The output in this region is relatively small (typically ~10^{-9} A) and, therefore, amplification is generally required to resolve the signal. Region 3 is known as the proportional region due to the fact that proportional counters are operated within it. In this region secondary ionisations are beginning to occur which cause a phenomenon known as gas multiplication (effectively amplifying the signal). It is also possible to determine the type of particle (and the energy of the particle) that deposits energy in this region. In practice, no single gas detector is used across the entire voltage range. Instead, detectors are specifically designed for use in one of the regions and tailored accordingly depending on performance requirements.

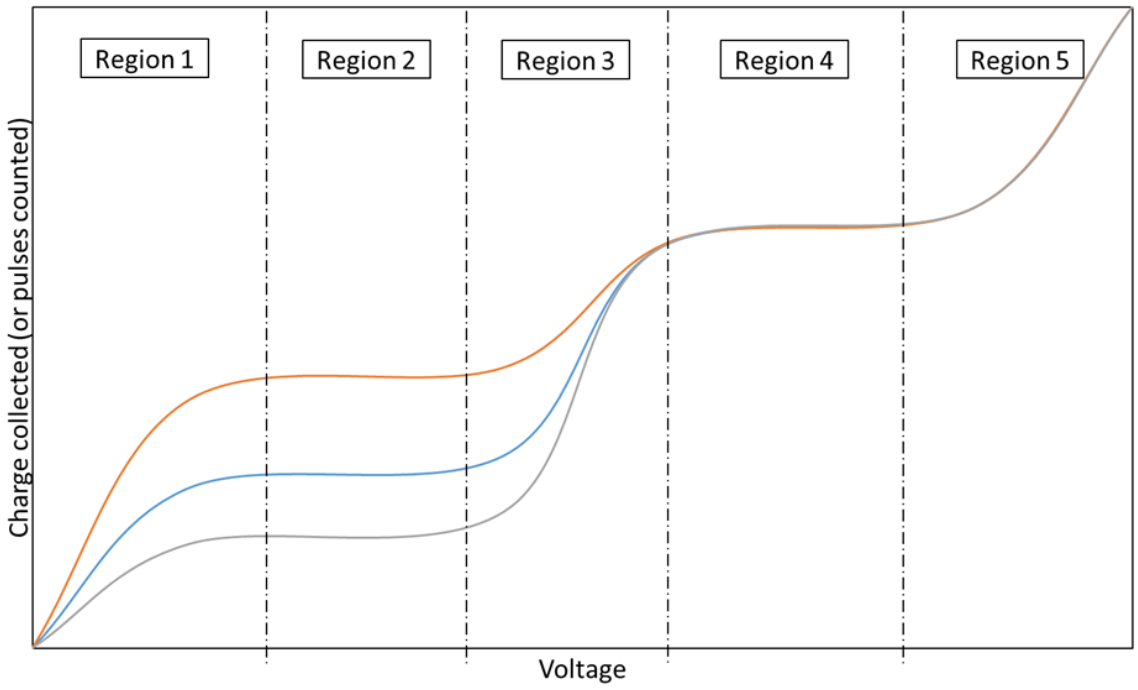

Figure 2-6: Response function of a gas-filled detector with respect to voltage. The three curves represent different energies of the incoming particles, with the orange line representing a higher energy and the grey a lower energy.

2.6.1.1 Ionisation chambers

Ionisation chambers are gas-filled detectors typically consisting of an anode and a cathode held at a high-voltage potential and separated by a pressurised counting gas (typically argon or nitrogen). As the radioactive emissions (typically gamma rays) travel through the gas, they ionise its atoms and create electron-ion pairs. These ionised particles are accelerated towards the anode or cathode as appropriate to their charge and a current may be observed. The current is proportional to the energy deposited per unit time and is related to the energy of the individual particles and the particle flux. Through the use of conversion factors, it is possible to determine the amount of radioactivity or the absorbed dose deposited in the chamber.

Ionisation chambers are one of the most commonly used detector types due to their simplicity, ease of construction and stability. Most relevant to nuclear medicine applications are ionisation chambers that have been designed as Radionuclide Calibrators (RCs). These incorporate a simple-to-use electrometer and readout system and are used to measure radiopharmaceutical activity prior to injection. Typically, these devices are the only means available to a hospital for the accurate measurement of radioactivity. Provided a good Quality Assurance (QA) schedule is employed, they can provide activity estimates with uncertainties of < 5 % for most gamma emitting radionuclides.

In general, radionuclide calibrators have a re-entrant type ionisation chamber (Figure 2-7), which allows the placing of a variety of container geometries into the central part of the chamber, thus increasing the detection efficiency. Since the counting gas is pressurised, it is impractical to place the source directly into the chamber itself as the walls of the container and chamber would interfere with the emitted particles before they interact with the gas. Chambers are typically constructed with aluminium or steel walls of the order of several mm thickness, and commercial devices also have special plastic holders for positioning the source. The vast majority of the energy deposited in the gas

is generated by photons, as all alpha particles are entirely attenuated, and the majority of beta particles are also stopped before reaching the gas. For this reason, radionuclide calibrators are sensitive to changes in geometry and it is important to know the effects of geometry when making measurements and considering uncertainty budgets.

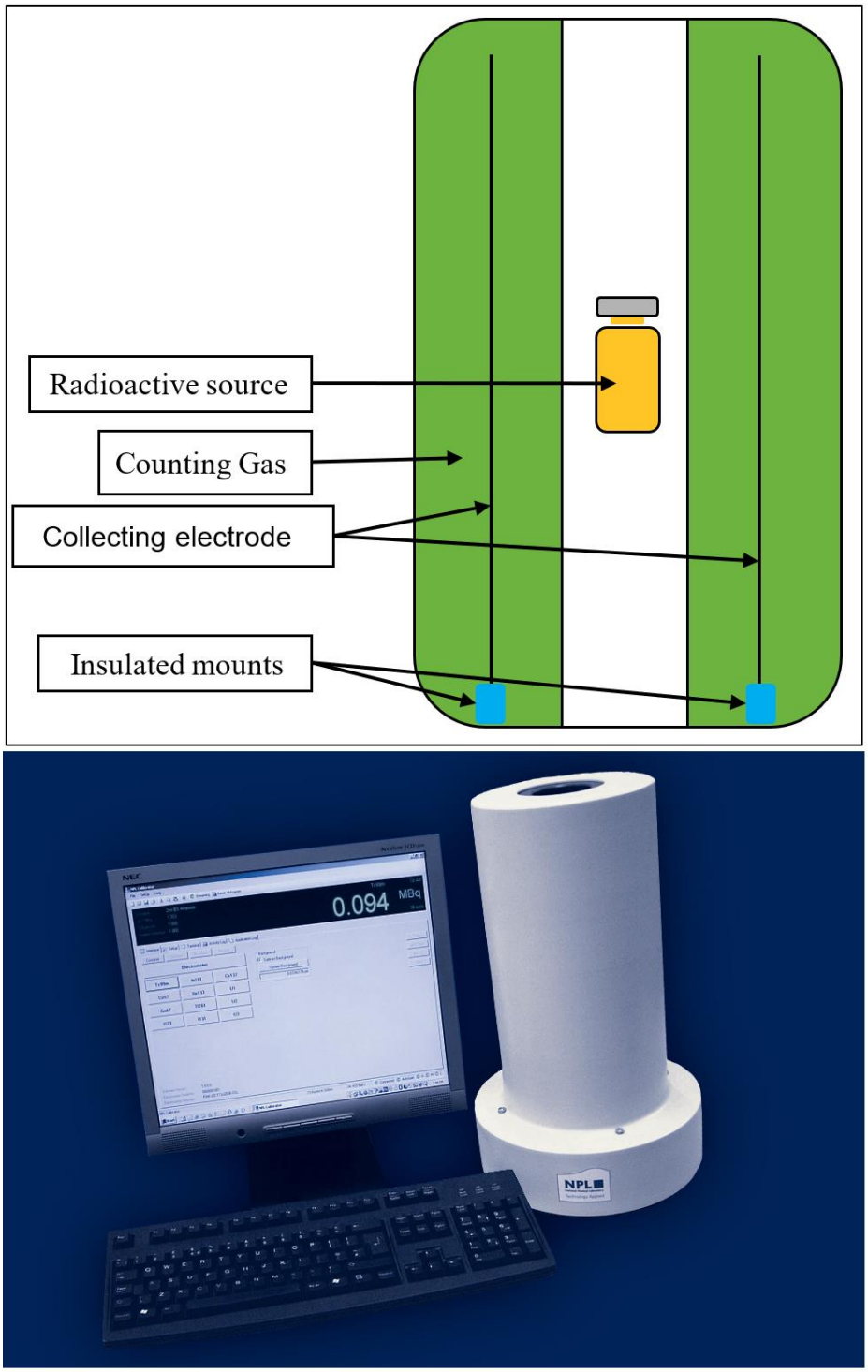

Figure 2-7: Typical schematic of a re-entrant type ionisation chamber (top) and a photograph of a radionuclide calibrator incorporating an ionisation chamber as the detector (bottom).

In radiation dose measurements, ionisation chambers are widely used, particularly in external beam radiotherapy applications. These ionisation chambers are typically very small and require large amounts of incident energy to provide an accurate response. Their design and the associated readout equipment limits their usefulness in patient studies, but they are widely used as reference calibration devices and in phantom studies to check the accuracy of treatment plans and delivered doses. Other larger ionisation chambers are also used to monitor ambient background dose rate in particle accelerator or nuclear reactor sites, and some have been developed as hand-held devices for a range of specialist applications.

2.6.1.2 Proportional counters

The proportional counter is closely related to the ionisation chamber, but operates in pulse mode. Therefore, it is better suited to detect specific emission types or to give spectral information. To work in this manner, it is preferable to have the source of radioactivity in close contact with the counting gas and, therefore, these detectors often either encapsulate the source, or have a thin window that allows most radiations to pass through without substantial loss (Figure 2-8).

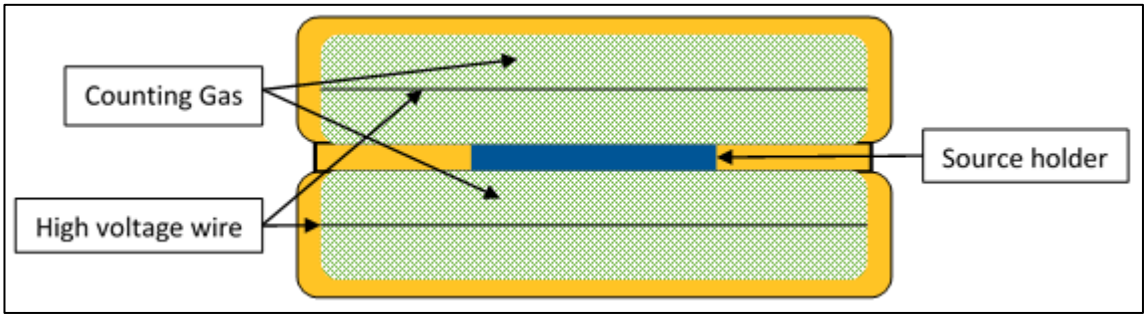

Figure 2-8: Typical design of a pill-box proportional counter.

2.6.1.3 Geiger-Müller (GM) tubes

GM tubes are used extensively in radiation protection as a simple means of detecting radioactive contamination or performing dose rate measurements, and are included here for completeness. The GM tube operates in the Geiger-Müller region of the curve shown in Figure 2-6 and does not output a response proportional to the incident energy. GM

tubes are sealed detectors with a thin window (typically made of mylar or similar material) to allow the radiation to pass through into the detection region. The type of windows used along with the type of gas, gas pressure and applied high voltage determine the sensitivity and types of radiation that can be detected. Since they are very versatile and come in a range of designs for specific purposes GM tubes are often found in laboratories for hand-held or fixed contamination monitoring or radiation dose measurement.

2.6.2 Semiconductor (solid-state) detectors

Semiconductor detectors operate in a similar fashion to ionisation chambers in that pairs of electrons and 'holes' (a positive vacancy left by the electron) are created when photons deposit energy in the material (Figure 2-9). The electrons in this case are excited from the valence band into the conduction band, leaving behind a 'hole' which behaves very much like a positive ion when an electric field is applied. These holes and electrons can be collected and measured as pulses from the detector by the application of a high voltage. Since the electron-hole pairs are created by transferring the energy deposited by the particle, it is possible to gain spectral information from the pulse height of the output signal, allowing the detector to be used to analyse samples in far greater detail than is possible with an ionisation chamber. High Purity Germanium (HPGe) is a commonly used semiconductor detector material. Due to its very small energy band gap, it must be cooled during operation, typically with liquid nitrogen. These detectors are usually housed in a graded lead shield to provide good background radiation reduction. Metals such as tin, cadmium and copper are used to reduce the characteristic x-rays from lead and other metals within the shield itself. The calibration of these detectors can become somewhat complex depending on the methodology, employed but typical energy and efficiency calibration can be readily achieved with a mixed gamma reference source of known activity placed in a reproducible geometry in front of the detector. A detector with a relative efficiency of 20 % can be expected to give an energy resolution of < 0.9 keV (at 122 keV) allowing easy identification of a sample through its emission

profile. Once a calibration is established, the system can be used to analyse and identify a range of gamma emitting radionuclides spanning the energies for which it has been calibrated.

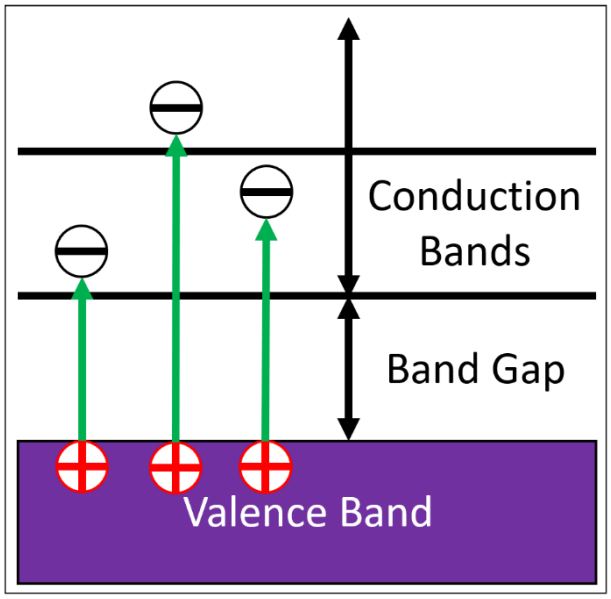

Figure 2-9: Mechanism of detection within semiconductor detectors

2.6.3 Scintillation detectors

Famously, scintillation detectors were one of the first devices used to measure radioactivity, by the physical counting of light flashes on a screen. A scintillator works in a similar manner to a semiconductor detector, with the incident radiation being absorbed and electron-hole pairs created in the conduction and valence bands respectively. Rather than directly counting charge pairs, their recombination leads to the emission of photons, which can be counted after amplification and conversion to electrical signals using photomultiplier tubes (PMTs) that are optically coupled to the material. Inorganic scintillators, such as thallium-doped sodium iodide (NaI(Tl)), rely on impurities known as activators to shorten the band-gap between the valence and conduction bands and increase the amount of scintillation light produced by improving the recombination efficiency (Figure 2-10). Once an electron-hole pair is created, the hole will immediately seek out an activator site and ionise it, creating a new hole for the electrons in the conduction band to populate.

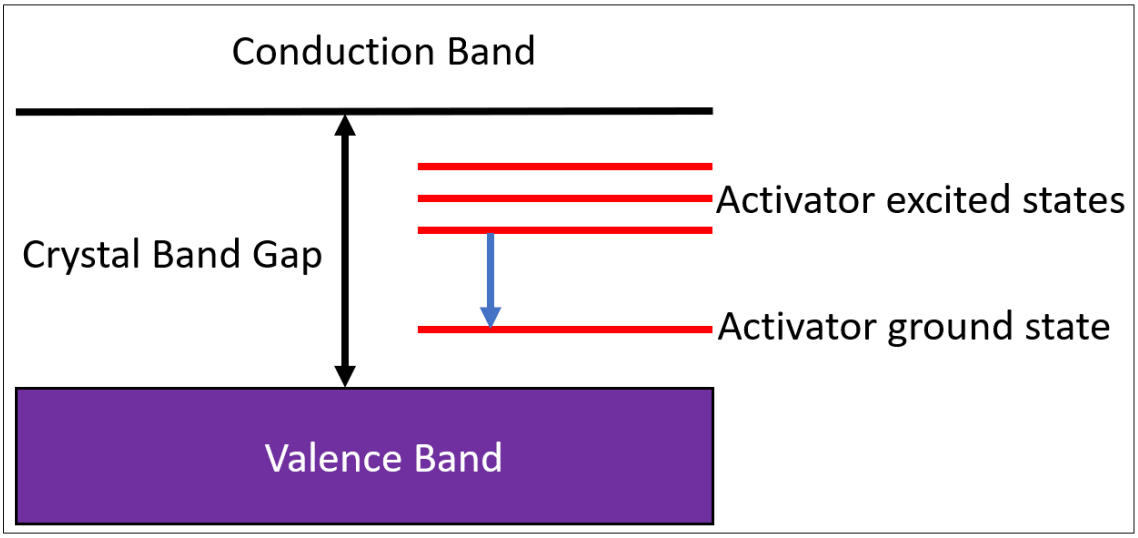

Figure 2-10: Activator energy levels in the band gap of an inorganic scintillator. The downward arrow denotes a photon emission following de-excitation of an electron within the activator atom.

Organic scintillators do not rely on actuators but are compounds of benzenoid rings and create light through molecular excitation rather than electron-hole pair formation. When ionising radiation passes through the scintillation compound the molecules are given energy and therefore excited into a higher energy band. In order to return to the ground state, the molecule will use vibration to lower its energy to the bottom of the next available excited level and then transition to the ground state during which a photon is emitted. These photons are then converted to an electrical pulse using PMTs as described previously. Organic scintillators have much faster decay time than inorganic scintillators and are therefore well suited to fast timing applications in nuclear physics experiments where nano-second timing resolution is required.

2.6.3.1 Liquid scintillation counting

Liquid scintillators are organic scintillation compounds (commonly referred to as cocktails) in liquid form and therefore have the advantage of being able to be mixed with a radioactive solution or artefact in order to improve scintillation efficiency. The PMTs in this instance are not usually optically bound to the scintillator as this would be impractical, but instead the scintillator is contained in a transparent sample holder (usually a glass or

plastic vial) and placed in an optical chamber with one or more PMT tubes in close proximity. The optical chamber reflects light to improve the efficiency of light collection by the PMT. This method is used extensively in the analysis of environmental samples due to its high efficiency and is particularly well suited to the measurement of high energy beta and alpha emitting radionuclides as the efficiencies are close to 100%.

An important consideration in liquid scintillation counting (LSC) is the 'quench' parameter which can be considered as a measure of counting efficiency. Quench is a measure of the light output relative to incident energy with a higher quench relating to a lower light output, leading to a lower counting efficiency. Samples can be intentionally quenched using chemicals or coloured dyes. Chemical quenching is the most commonly used method and works by interfering with the interaction between the emitted particles and the scintillator. Colour quenching absorbs the emitted light from he scintillator before it can interact with the photocathode of the PMT.

2.7 Methods for primary standardisation of radioactivity

Primary standards in radioactivity are realised through a variety of techniques, which must be tailored to each radionuclide based on its decay characteristics. In many instances it is possible and beneficial to use multiple techniques in order to provide increased confidence in the determined activity.

2.7.1 CIEMAT/NIST Efficiency Tracing

The use of commercial liquid scintillation counting systems to perform primary standardisations was conceived in the early 1980's as a joint venture between two institutions: the Centro de Investigaciones Energéticas, Medioambientales y Tecnológicas (CIEMAT) in Spain, and the National Institute of Standards and Technology (NIST) in the USA (Malonda and Garcia-Toraño, 1982). The method relies on both experimental determination of counter efficiency at given quench values using a standardised source (typically ^{3}H), and the theoretical calculation of the 'free parameter'

for the counter. This information may then be used to determine the relative efficiency of the system for an unknown radionuclide at a given quench parameter using available nuclear data (Figure 2-11).

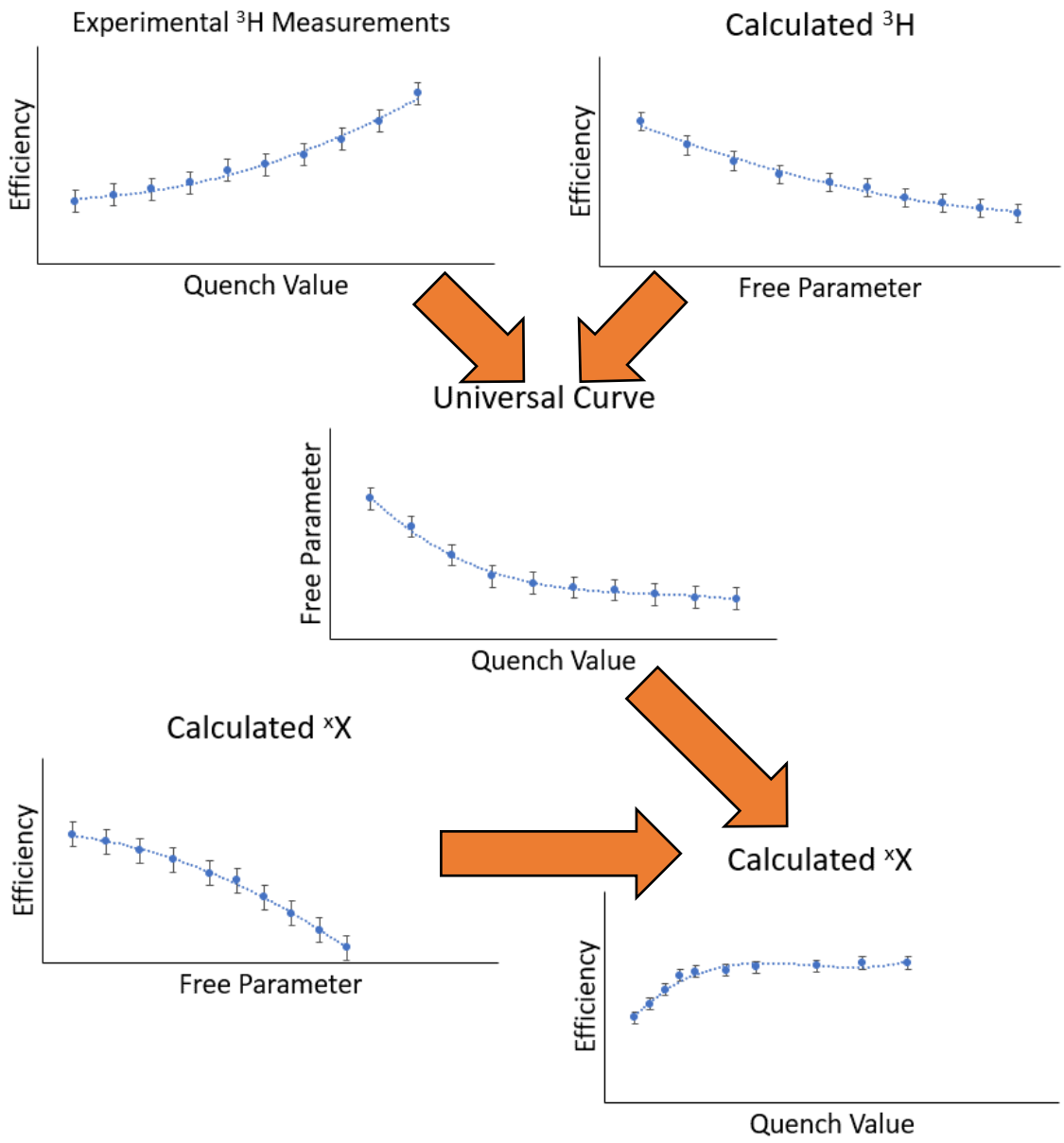

Figure 2-11: Depiction of experimental and theoretical calculation steps involved when using the CIEMAT/NIST technique. Adapted from (Malonda, 2001).

The free parameter is determined by Poisson modelling of the light production process within the scintillation counting system. It is therefore reliant on the composition of the sources used in the measurement of the standard being identical to those of the unknown radionuclide. Several computer modelling and simulation codes exist to perform the free

parameter and efficiency modelling with varying degrees of complexity, and a good summary of the methodology can be found in the work of Gunther (2002) and Pochwalski et al. (1988) among others. The CIEMAT/NIST (CN) technique has been successfully applied to a multitude of radionuclides with various decay schemes, and is well understood by the metrology community.

2.7.2 Triple to double coincidence ratio

The Triple to Double Coincidence Ratio (TDCR) method in another liquid scintillation counting technique. However, in this instance, it does not rely on efficiency tracing using another radionuclide. It was conceived in the early 1960's by a German group (Hoegl and Schwerdtel, 1963) in response to the difficulties of using existing liquid scintillation counters in primary standardisation work. Originally, the method relied on determining relative efficiencies using standards of radioactivity and employing a 3-PMT liquid scintillation counter to monitor the number of coincidences observed from a source. This was developed in the 1970's (Pochwalski and Radoszewski, 1979) with the addition of a model of the detection efficiency in order to remove the requirement to use a tracer radionuclide and has been constantly improved since (Broda, 2003).

2.7.3 4π β-γ Coincidence counting with efficiency extrapolation.

Coincidence counting relies on observing the coincidence emission of particles between disintegration modes, and using these to determine a counting efficiency for the detector system. With a simple decay scheme (Figure 2-12) the coincidences between betas and prompt gammas in the same decay are observed and are used to determine the efficiencies of each detector.

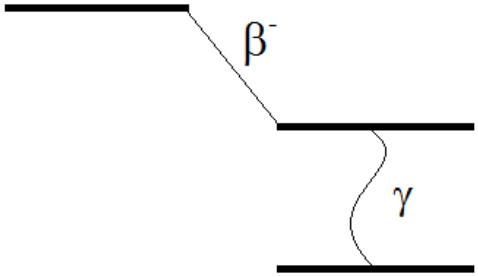

Figure 2-12: A simple non radionuclide specific β-γ decay scheme. This is done with a standard set of equations (Equation 2-14 - Equation 2-16) (Baerg, 1973a)

$$N_\beta = N_0 \varepsilon_\beta$$

Equation 2-14 (Baerg, 1973a)

$$N_\gamma = N_0 \varepsilon_\gamma$$

Equation 2-15 (Baerg, 1973a)

$$N_c = N_0 \varepsilon_\beta \varepsilon_\gamma$$

Equation 2-16 (Baerg, 1973a)

where:

N_0 is the disintegration rate

$N_{\beta,\gamma,c}$ is the observed β,γ and coincident rates respectively

$\varepsilon_{\beta,\gamma}$ is the efficiency of the beta/gamma detector respectively

These methods are described in detail in many publications (Baerg, 1973b; Baerg et al., 1966; Barnothy and Forro, 1951; Dunworth, 1940; Keightley and Park, 2007; Keightley and Watt, 2002; Putman and Siegbahn, 1955; Smith and Chen, 1985).

If the radionuclide decays by multiple modes or by multiple branches as shown in Figure 2-13, equations 2-14 to 2-16 no longer hold true, and corrections must be made as shown in equations 2-17 to 2-19 (Baerg, 1973a).

$$N_\beta = N_0 \sum a_r \left[\varepsilon_{\beta r} + \left(1 - \varepsilon_{\beta r}\right) \left(\frac{\alpha \varepsilon_{ce} + \varepsilon_{\beta\gamma}}{1 + \alpha} \right)_r \right]$$

Equation 2-17

$$N_\gamma = N_0 \sum a_r \frac{\varepsilon_{\gamma r}}{1 + \alpha_r}$$

Equation 2-18

$$N_c = N_0 \sum a_r \left[\frac{\varepsilon_{\beta r} \varepsilon_{\gamma r}}{1 + \alpha_r} + (1 - \varepsilon_{\beta r}) \varepsilon_{cr} \right]$$

Equation 2-19

where:

α_r is the internal conversion coefficient for the β- branch

ε_{ce} is the efficiency of the β-detector for the conversion electrons

$\varepsilon_{\beta r}$ is the efficiency of the β-detector

$(\varepsilon_{\beta\gamma})_r$ is the efficiency of the β-detector to γ-rays from the rth branch

$\varepsilon_{\gamma r}$ is the efficiency of the γ-detector to the γ-rays from the rth branch

ε_{cr} is the probability of recording a coincidence if the associated β-particle is not detected

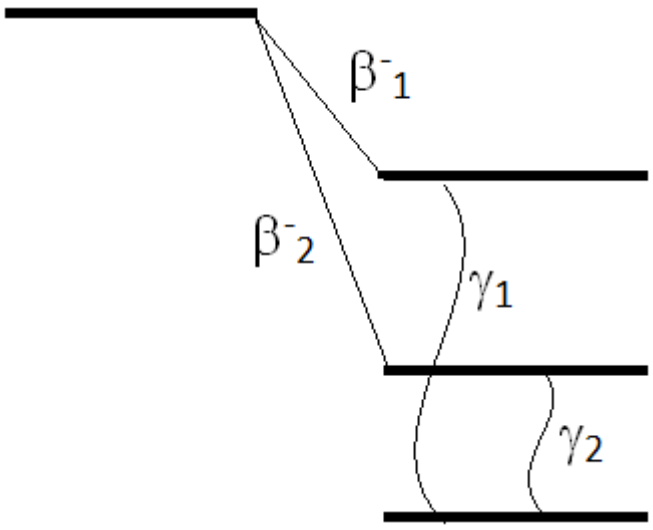

Figure 2-13: A non-radionuclide specific β-γ decay scheme showing multiple beta decay branches. Equations taken from (Baerg, 1973a):

In order to minimise the corrections required, a method of varying the efficiency of one of the detectors may be employed in order to extrapolate back to unit efficiency (Baerg, 1973a). When using an Atmospheric Pressure gas Proportional Counting system (APPC), the beta efficiency is often varied by manipulation of the source (such as

covering it with an attenuating material) or by varying the beta detection threshold. The higher the polynomial order of the fit, the more difficult it is to produce accurate extrapolations and, therefore, the extrapolation should be as linear as possible. In addition, to further reduce uncertainty, the efficiency of the beta detector should initially be as high as possible so that the extrapolation is not over a large range. From the above, it can be seen that more complex decay schemes will require more complex corrections making the method more difficult to implement.

At NPL, the APPC, High Pressure Proportional Counting (HPPC) and Liquid Scintillation Digital Coincidence Counting (LS-DCC, Figure 2-14) systems are used, depending on the needs of the radionuclide being standardised. Typically, most measurements are performed using the LS-DCC due to the simplicity of operation and versatility when measuring a range of radionuclides. An example of this method being used is given in 2.9.1 and described in more detail in Michotte et al. (2016)

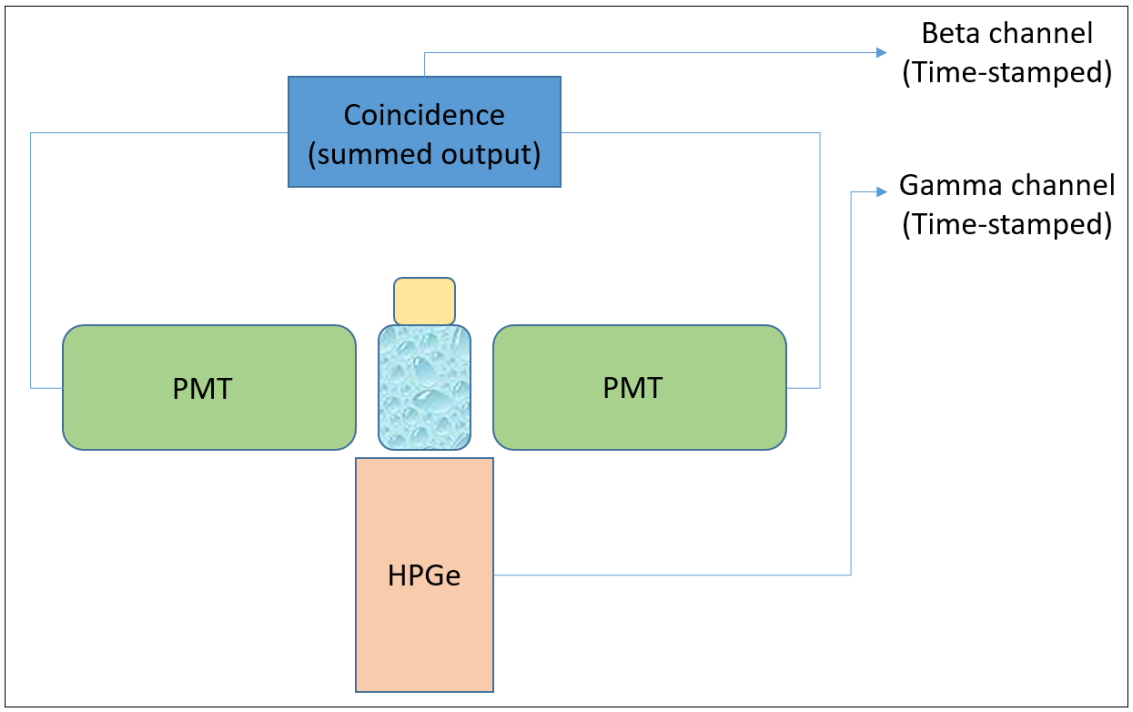

Figure 2-14: Layout of the LS-DCC counting system. The PMT's are connected to a coincidence circuit to reduce dark noise. Both channels are collected in 'live time' whereby each pulse is assigned a unique time-stamp.

2.8 Positron emission computed tomography

PET imaging uses the emissions of a radionuclide decaying by positron emission to image a bodily function using a detector array. The underlying principle is to observe coincident 511 keV gamma events at 180° arising from the annihilation of positrons to build up a series of response lines which, once overlaid, will indicate the most probable sites of annihilation. The technique was first tested as far back as the 1950s, but it was not until the 1970s when ^{18}F labelled 2-fluorodeoxy-D-glucose (now commonly known as FDG) was trialled in patients, that it began to be seen as a useful routine medical tool.

The layout of a typical modern PET camera can be seen in Figure 2-15. It consists of several rings of detector modules surrounding a moving patient bed. Typically, each detector module will typically consist of a pixelated scintillation crystal optically bonded to an array of photomultiplier tubes to give positional information across the crystal. It is preferable to use scintillators with fast timing characteristics to improve the resolving time of the coincident photons, and crystal types such as cerium-doped lutetium yttrium orthosilicate (LYSO) are commonly used.

More recently, there has been the introduction of so-called ‘digital PET’, in which silicon photomultipliers are employed. These enable faster timing and greater sensitivity to be achieved, along with the ability to combine additional modalities such as Magnetic Resonance Imaging (MRI). Except for the detector and photomultiplier, these systems operate in the same manner as the traditional systems.

Following detection of the incident photons, the position of the interaction is recorded, and the pulses are saved in ‘list-mode’, in which each event is binned by time and energy to be handled off-line. To allow accurate recording of energies and positions, a series of corrections are required to ensure energy, uniformity and alignment are all comparable. The corrected pulses are then used to reconstruct a three-dimensional pixel (voxel)

image using one of a variety of reconstruction methods, typically based on Ordered Subset Expectation Maximisaton (OSEM) techniques.

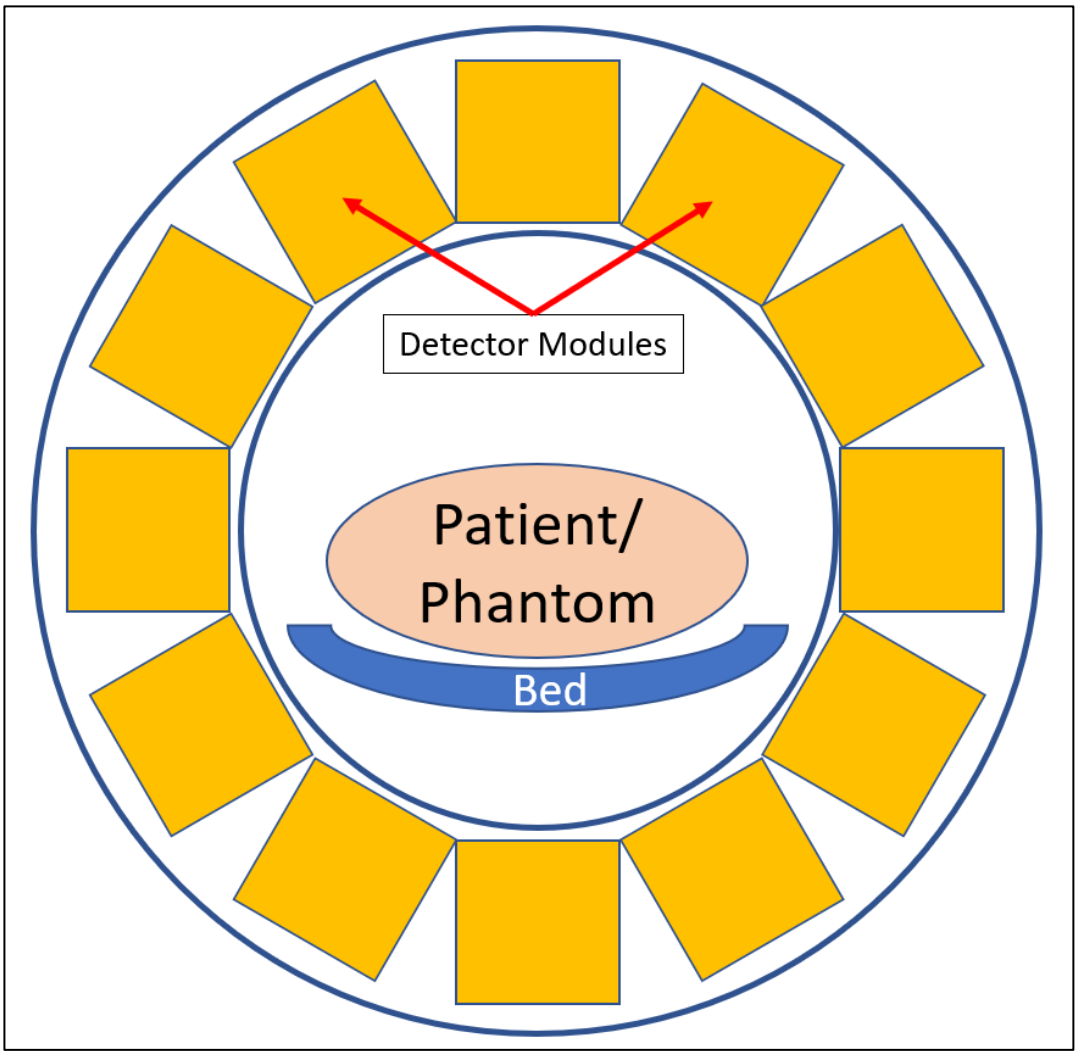

Figure 2-15: Layout of a typical modern PET camera

PET systems are typically coupled to CT systems to provide geometrical information. This can be used to apply scatter and attenuation correction to the acquired data as well as giving anatomical information. PET systems can be used for in both pre-clinical and clinical applications with the primary difference in hardware being the size and effective number of detectors. Due to the smaller geometry in pre-clinical studies it is possible to obtain sub-millimetre resolution and therefore testing of novel radiometals such as ^{89}Zr is possible in a pre-clinical environment before moving to human studies.

2.9 Underlying standards of radioactivity

In order to calibrate and monitor the performance of radioactivity measurement systems, it is necessary to use multiple standardised radionuclide solutions and artefacts. In the case of high purity germanium detectors (and other spectral measurement systems), it is necessary to use different radionuclides covering the energy range of interest for energy and efficiency calibration of the system (perhaps higher depending on the emissions of the radionuclides under study). In the case of ionisation chambers, even though each radionuclide calibration factor is derived from a primary standard directly, it is necessary to have a range of factors for radionuclides of interest in order to correct for impurities and to determine model response curves. In PET imaging systems it is common practice to use a single radionuclide (often ^{18}F) for energy and sensitivity calibration as this is more practical in a clinical environment. At NPL there is easy access to primary standards of a host of radionuclides and therefore the NPL equipment used in this project has all been calibrated in a traceable manner where appropriate. The imaging equipment at both NPL and Cardiff has been calibrated using ^{18}F which is traceable to NPL via transfer instruments. Fluorine-18 was standardised as part of a separate project (Michotte et al., 2016) but the method and results are presented briefly in section 2.9.1 as an example.

2.9.1 Standardisation of ^{18}F

Flourine-18 is an important radionuclide in PET imaging and is used extensively across the world. It is favoured primarily due to its ability to be conjugated as a glucose analogue and its short half-life of 1.82890 (23) hours. This short half-life makes it difficult for international organisations to compare measurements of the same solution, and the BIPM SIR system which is traditionally used to establish equivalence becomes limited to NMIs which are geographically close to Paris due to the limitations on transport. To address this issue the BIPM introduce a new travelling instrument known as the SIRTI (SIR Travelling Instrument) based on a sodium iodide well-type crystal and in order to

determine its efficacy this instrument was compared against equipment at sites that had previously submitted samples to the SIR. NPL took part in a multi-lateral study to both validate the accuracy of the SIRTI system and also to update the NPL equivalence value. This work is briefly described here due to the use of ^{18}F as a calibration radionuclide in this study, a more complete report has been published by Michotte et al. (2016).

2.9.1.1 Method

A solution of ^{18}F as fluorodeoxyglucose (FDG) was dispensed in 0.1 g aliquots to a set of 6 liquid scintillation vials containing 10 ml of Ultima Gold LLT (Perkin Elmer, USA) scintillant and 1 ml of deionised water. The same solution was dispensed to 2 ml and 5 ml BS ampoules for measurement by ionisation chamber, a 2 ml ISO ampoule for measurement by gamma spectrometry and 3.6 g to an NBS ampoule for measurement in the SIRTI instrument for validation testing. Following successful results of the validation, the source preparation was repeated using a fresh solution of ^{18}FDG in order to determine the NPL equivalence value.

2.9.1.2 Measurements: Primary standardisation

The liquid scintillation vials from both experiments were measured using the NPL digital 4πβ-γ coincidence counting system described in 2.7.3. and shown in Figure 2-14. The HPGe detector was replaced with a sodium iodide detector in order to increase gamma detection efficiency. Each source was measured for between 400 s and 600 s leading to >100,000 counts in the 511 keV photon peak. The lower level discriminator (LLD) on the beta channel was set to exclude contributions from Auger and x-ray emissions from the electron capture branch of the ^{18}F decay. A gamma gate was applied to the 511 keV peak and the beta channel efficiency was varied using the computer discrimination method presented by Smith (1975) and Smith (1987). Efficiencies were varied between 0.98 and 0.90 and a linear extrapolation was made to determine unit efficiency. Since the electron capture branch of decay has been excluded, it is necessary to perform a

correction to the final result using the positron branching ratio for ^{18}F, which was taken as 0.9686 (19) (Bé et al., 2004).

2.9.1.3 Measurements: Secondary standards and SIRTI

The ionisation chamber ampoules were measured using dedicated holders on the NPL Vinten 671 (Vinten Instruments, UK) and 'PA782' (Atomic Energy Research Establishment, UK) secondary standard ionisation chambers which had previously been calibrated for ^{18}F in the geometries specified. A mean of the ampoule measurements was taken for comparison with the primary result and the SIRTI measurements. An ampoule was also measured using a calibrated high-purity germanium detector to determine the presence of impurities but none were detected. The SIRTI ampoule was measured 10 times over 4 half-lives at count rates lower than 20,000 s^{-1}. To minimise the uncertainty contribution due to decay during measurement, each measurement was made for a maximum of 400 s. When all measurements were decayed to a common reference time, a reduced chi-squared value for the count rate results from the SIRTI was determined to be 0.88 for the equivalence measurements.

2.9.1.4 Results and discussion

The primary standard results are presented alongside those from the other laboratories participating in the SIRTI trial in Table 2-1 and as part of the updated Key Comparison Database (KCDB) in Figure 2-16. The results in the KCDB include subsequent submissions to the SIR using the travelling instrument from NMISA (National Metrolgoy Institute of South Africa) and NIST which are detailed in Michotte et al. (2017c) and Michotte et al. (2017b) respectively. The results show all five laboratories participating in the SIRTI trial are in statistical agreement with other NMIs who have submitted samples directly to the SIR (shown as red triangles). The three laboratories shown in blue triangles have determined equivalence using an ionisation chamber response comparison, and hence uncertainties are far greater than that achieved using the SIRTI instrument. The measurements undertaken by ionisation chamber confirmed that the

calibration factors in use on the secondary standard ionisation chamber system give an activity within 0.1 % of the primary result. However, the standard uncertainty on the calibration factor value is 1 % using the previous standardisation. Therefore, it was decided that new calibration factors should be determined using the lower uncertainty achieved during this comparison.

NMI, date	Measurement method	Activity conc. (kBq g^{-1})	Standard uncert. (kBq g^{-1})	Reference date (YYYY-MM-DD)	A_E (kBq)	$u(A_E)$ (kBq)	Linked A_e (kBq)	$u(A_e)$ (kBq)	D_i (MBq)	U_i (MBq)
VNIIM, June 2014	4πβ (NaI) counting	44.73	0.27	2014-06-26 8:00 UTC	10.164	0.063	15 197	97	−0.08	0.20
NPL, Sept. 2014	4π(LS)β$^+$-γ(NaI) coincidence counting	26.02	0.06	2014-09-25 12:00 UTC	10.241	0.032	15 311	52	0.04	0.11
	4π(LS)β$^+$-γ(NaI) coincidence counting	2.679	0.013							
ENEA-INMRI, Oct. 2014	4πγ counting	2.678	0.014	2014-10-27 13:00 UTC	10.279[a]	0.031	15 368	49	0.09	0.11
	TDCR	2.679	0.013							

[a]Result based on the arithmetic mean (2.6790(78) MBq g^{-1}) of the results using the three measurements methods, estimated by the ENEA-INMRI taking into account correlations.

Table 2-1: Results of the SIRTI comparison exercise from participating laboratories (taken from ((Michotte et al., 2016))).

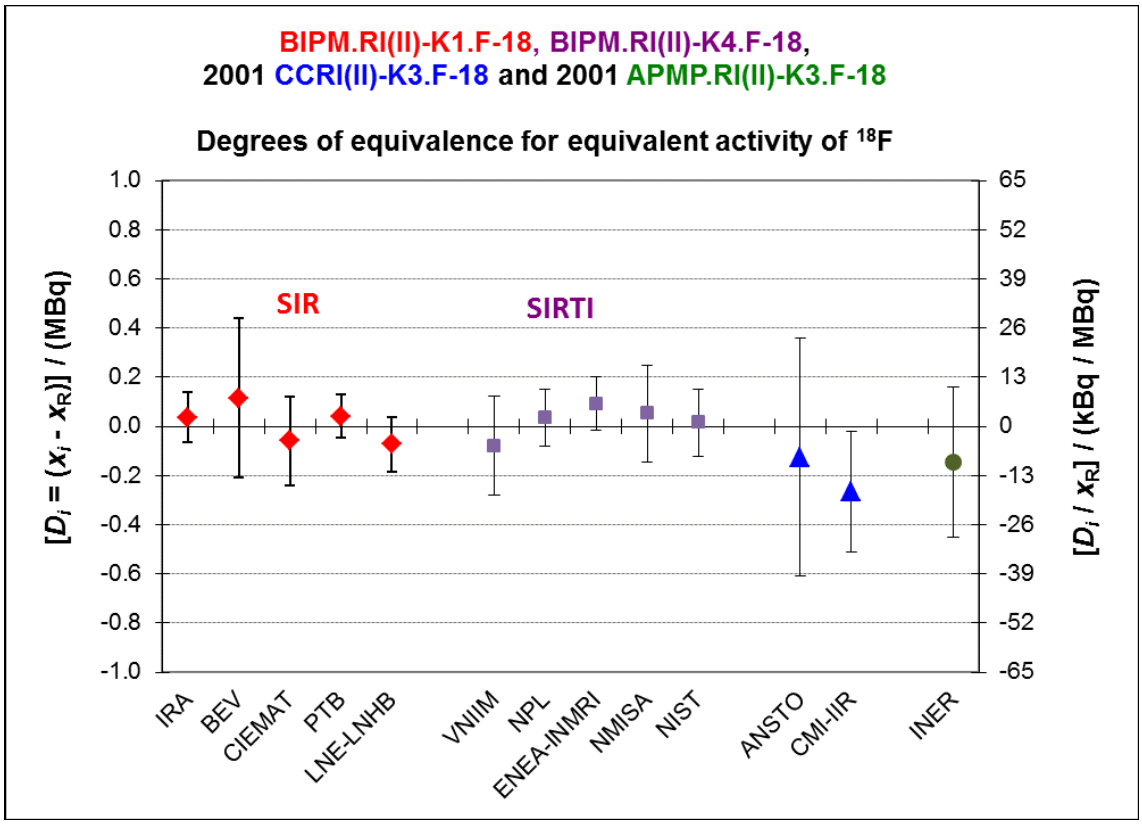

Figure 2-16: Updated Degrees of equivalence for ^{18}F as published in the KCDB ((Michotte et al., 2017a)).

2.9.1.5 Conclusion

The results from the SIRTI comparison demonstrate NPL's equivalence for ^{18}F and confirm the traceability of existing calibration factors in use on the NPL secondary standard systems. The SIRTI has been demonstrated to be an important tool when comparing laboratories which are distant from BIPM and global equivalence for this important radionuclide can now be achieved.

2.10 Chapter summary

This chapter introduced underlying physical concepts that will be referred to in later chapters of this thesis. Beginning with the basic properties of radioactivity the chapter progresses through interactions, units and measurement techniques relevant to this work. The primary activity standardisation of ^{18}F was summarised to demonstrate traceability for this radionuclide which is used in the calibration of PET cameras.

Chapter 3: Absolute Standardisation and Nuclear Data Measurements of ^{89}Zr

3.1 Introduction

This chapter addresses the measurement of nuclear data and primary activity standardisation of ^{89}Zr which underpins all activity measurements of ^{89}Zr within this thesis. The specific objectives are as follows:

- New primary activity standardisation of ^{89}Zr and calibration of secondary standard systems.
- New determination of the half-life of ^{89}Zr.
- New measurement of normalised (relative) and absolute gamma emission intensities.
- New evaluation of nuclear data to include those determined in this work.

Primary activity standardisation represents the first link in the chain of traceability (Figure 1-1) and links measurements performed in clinical departments with those undertaken at a national and international level. Improvement in the published nuclear data through measurement and re-evaluation will lower uncertainty introduced during decay correction and improve measurement of activity by techniques such as gamma spectrometry. The measurement of the positron branching ratio will be completed in later works, outside the scope of this thesis. All uncertainties in this and subsequent chapters are stated as combined standard uncertainties unless stated otherwise.

3.2 Overview of existing data

3.2.1 Decay properties

Zirconium-89 decays by electron capture (77%) and positron emission (23%) to excited states of ^{89}Y with subsequent gamma transitions to the ground state (Figure 2-4). Most decays pass directly through the 908.97 (3) keV metastable state of ^{89}Y, which has a

half-life of 15.84s. Several lower probability (<1%) electron capture branches populate higher excited states and de-populate to the same 909 keV level, except for a single branch populating the 1744.72 (18) keV level and decaying directly to the ground state of ^{89}Y. The decay data of ^{89}Zr have been determined by several independent studies during the last century. These data are well summarised in evaluations performed by the Decay Data Evaluation Project (DDEP) (Bé et al., 2016) and the International Network of Nuclear Structure and Decay Data Evaluators (NSDD) (Singh, 2013), wherein derived gamma emission probabilities, electron capture/positron branching ratios, and half-life values are determined from previously published data using statistical methods. A recent paper by Garcia-Torano et al. (2018) describes work on a half-life measurement, primary standardisation and associated radionuclide calibrator dial settings but does not provide any additional gamma emission intensity data. Although the values are in good agreement, the relative uncertainties ascribed to the gamma emission intensities are significant; in particular the standard uncertainty on the positron branching ratio as used in medical imaging applications is 1.3%. All previous measurements have been defined by relative measurements (using the 908.97 keV transition as a reference point) and there has been no direct measurement of the photon emission intensities using a solution of ^{89}Zr traceable to a primary standard.

3.2.1.1 Electron and positron emissions

As previously mentioned, ^{89}Zr decays by both positron and electron capture processes to excited levels of ^{89}Y. Evaluators have taken the gamma ray emission data and used these to determine a balanced decay scheme in terms of energies and emission probabilities, and this is reported by both DDEP (Bé et al., 2016) and NSDD (Singh, 2013). There are five electron capture branches with a combined emission probability of 77.248(30) % and energies of 211(3), 266(3), 303(3), 1088(3) and 1924(3) keV. There is a single positron branch with an emission probability of 22.8(3) %, a positron maximum energy of 902(3) keV and an average positron energy of 395.7(14) keV. Theoretical

calculations of Auger emission data using the EMISSION computer model (Schönfeld and Janßen, 2000) are reported by DDEP (Bé et al., 2016), and these identify emissions from 12-17 keV in the K-shell and 1.27-1.89 keV in the L-shell.

3.2.1.2 Gamma and X-ray emissions

X-ray emissions during the shell re-arrangements are primarily in the 14 keV to 17 keV energy range. The primary gamma emission is from the 909 keV transition within ^{89}Y. All other emissions account for less than 1 % of the decay (other than annihilation photons associated with the positron branch) and have energies ranging from 1620 keV to 1745 keV. The X-ray and gamma emissions are listed in Table 3-1.

Energy (keV)	DDEP Emission Intensity (%)
1.686 – 2.347	2.36(5)
14.8829	14.08(13)
14.9585	27.01(20)
16.7259 16.7381 16.88	6.78(8)
17.0156 17.0362	0.94(4)
511	45.6(6)
908.97(3)	99.03(2)
1620.83(20)	0.074(5)
1657.58(15)	0.106(5)
1713.1(3)	0.745(10)
1744.74(18)	0.1231(40)

Table 3-1: x- and gamma-ray emission intensities in the decay of ^{89}Zr as published by DDEP (Bé et al., 2016)

3.2.1.3 Half-life

The half-life value is reported in the current DDEP publication (Bé et al., 2016) as 78.42(13) h and as 78.41(12) h in the ENSDF database (Singh, 2013). Figure 3-1 shows the spread of half-life values found in the literature. Due to large discrepancies or a lack of uncertainties, several points have been excluded from both evaluations (Sagane et

al., 1938), (Sagane et al., 1940), (Hyde and O'Kelley, 1951), (Shure and Deutsch, 1951), (Katz et al., 1953), (Howe et al., 1962). The data measured prior to 1962 show large deviations, but the values obtained in later years show more consistency. It is likely that this is due to the instability of equipment and difficulty in detecting impurities. Both evaluations were performed prior to the publication of the value obtained by Garcia-Torano et al. (2018) and are, therefore, heavily weighted toward the value of Van Patter and Shafroth (1964) due to its relatively small uncertainty. The value of 78.333 (38) h obtained by Garcia-Torano et al (2018) is determined as a weighted mean of four measurements on a high purity germanium detector and two measurements on a high-pressure re-entrant type ionisation chamber. The paper has a robust description of the method used for measurement and calculation and contains a detailed uncertainty budget, unlike many of the previous publications.

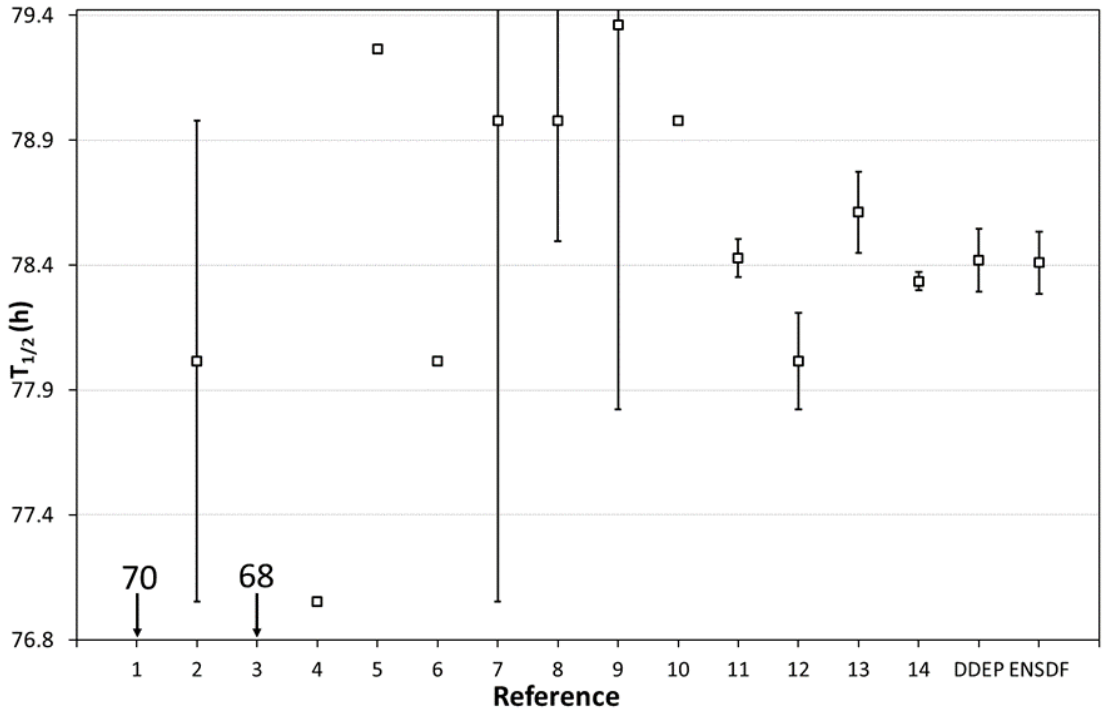

Figure 3-1: Values considered in the DDEP and ENSDF evaluations of the ^{89}Zr half-life. For clarity the y-axis has been adjusted to exclude two data points ((Sagane et al., 1938), (Sagane et al., 1940) as identified by the arrows. The references are listed in Figure 3-12

3.2.2 Main production modes

3.2.2.1 Proton irradiation of ^{89}Y

By far the most common and well researched method for the production of ^{89}Zr for medical applications is the ^{89}Y (p,n) ^{89}Zr reaction proposed by (Link et al., 1986). Provided proton energies are maintained below 14 MeV, the production of unwanted impurities, such as ^{88}Zr and ^{88}Y, is negligible. Therefore, by tuning the beam energy to around 13 MeV on a target of high purity ^{89}Y, it is possible to obtain high yields (>80 %) of ^{89}Zr with minimal impurities (Meijs et al., 1994). Many studies have investigated the most efficient modes for producing ^{89}Zr using this method, in particular, the favourability of using filters and varying target thickness to optimise yields and purity on hospital cyclotrons with limited energy ranges. A host of studies have also investigated the various purification techniques required post-production to remove impurities (^{48}V and ^{56}Co) resulting from the target foil. Typically, a method involving double solvent extraction followed by an anion exchange resin can be utilised to produce a product with purity of 99.99 %.

3.2.2.2 Deuteron irradiation of ^{89}Y

The ^{89}Y(d,2n)^{89}Zr reaction utilising deuterons at energies above 5.6 MeV has been investigated in several works, and can be used to produce ^{89}Zr with a comparable purity to that obtained by proton irradiation (Lebeda et al., 2015). Purification is generally achieved using an anion exchange resin rinsed with varying concentrations of hydrochloric acid. Arguably, this leads to a simpler purification method, but problems have been noted when using this technique and it would benefit from further study (Hohn et al., 2008). The limited availability of cyclotrons providing deuteron beams means that this method is not widely used outside of academia, and is unlikely to be adopted in the clinical environment at present.

3.2.2.3 Alpha particle induced reaction on ^{nat}Sr

Few articles can be found in the literature regarding direct production through the $^{nat}Sr(\alpha,[x]n)^{89}Zr$ reaction. However, several authors have investigated the excitation functions, separation and extraction techniques as a by-product of other investigations (Deri et al., 2013). The collected works identify that high purity material can be produced using the $^{88}Sr(\alpha,3n)^{89}Zr$ reaction. However, due to the other naturally occurring isotopes present in ^{nat}Sr (^{86}Sr, ^{87}Sr), the production of unwanted impurities limits the upper beam energy, resulting in lower yield (Ivanov et al., 2014). Yields may be improved by using enriched ^{88}Sr, but this is generally considered to be prohibitively expensive for routine applications.

3.2.3 Primary and secondary standards

At the beginning of this project, there had been no previously published primary standardisation and very little other metrological work in relation to ^{89}Zr. In 2018, a team from CIEMAT undertook a standardisation using the TDCR, 4πγ and 4πβ-γ coincidence counting methods (Garcia-Torano et al., 2018). The paper indicates that using the TDCR and 4πγ counting methods, it is possible to obtain final activity uncertainties of less than 1 %. However, the 4πβ-γ coincidence method relies on using the positron branch only and, therefore, since a correction for the positron branching ratio must be applied, an additional uncertainty is introduced taking the final uncertainty up to 1.8 %. In 2019 a paper published by a team from the Horia Hulubei National Institute of Research and Development in Physics and Nuclear Engineering (IFIN-HH) in Romania describing the use of the 4πβ-γ method on the positron branch and the resultant 2% uncertainty on the final result is in agreement with the CIEMAT findings (Sahagia et al., 2019). Unfortunately, neither of these institutes submitted a sample to the BIPM SIR system, nor did they publish calibration factors for a comparable device (such has the Vinten 671 ionisation chamber) or nuclear data that could be compared to check if they were in agreement with each other.

Previous work to provide dial settings for ^{89}Zr on commercially used radionuclide calibrators cover a 10 % range and, therefore, it is difficult to be certain about which settings should be used in practice (Avila-Rodriguez et al., 2007; Beattie et al., 2014; Capintec, 2009; Verel et al., 2003; Wooten et al., 2016). In 2019, the group from CIEMAT provided a follow-up publication to the work performed in 2018, detailing traceable dial settings for a range of commercial radionuclide calibrators in a variety of geometries (Garcia-Torano et al., 2019). However, this publication was unavailable at the time of the standardisation work undertaken in this thesis and published in 2020 (Fenwick et al., 2020). It also neglected to include nuclear data studies or 'Vinten' calibration factors for easy comparison.

3.3 Methodology: primary standardisation

The primary standardisation was performed using the CIEMAT/NIST method described in section 2.7.1. This method was chosen following investigations into the potential of standardising the solution using 4π-βγ coincidence counting and TDCR counting, for which the measurements are also summarised below.

3.3.1 CIEMAT/NIST efficiency tracing

3.3.1.1 Source preparation

Two sets of vials were prepared with a common chemical composition to provide the tritium and ^{89}Zr sources for the CIEMAT/NIST standardisation. The base composition of both sets of LSC sources was 10 ml Ultima Gold AB (UGAB) (Perkin Elmer, USA) scintillant, 0.2 g of 2 mol dm^{-3} hydrochloric acid (containing 10 µg g^{-1} inactive zirconium) and 0.1 g deionised water. The tritium vials contained 0.1 g of tritiated water replacing the deionised water, and the zirconium vials contained 0.1 g of active zirconium in 2 mol dm^{-3} hydrochloric acid in place of 0.1 g of the inactive zirconium carrier. Sources were prepared by gravimetrically dispensing and weighing aliquots of the respective solutions using a pycnometer. A dilution was performed prior to the dispensing of the

active zirconium from the solution that was measured on the ionisation chamber and gamma spectrometry systems. The gravimetrically calculated dilution factor was confirmed by gamma spectrometry measurement.

3.3.1.2 Measurements

The tritium and zirconium vials were measured 4 times over 3 days using a model 2910TR liquid scintillation counter (Canberra-Packard, USA). The counter was operated in coincidence mode with an 18 ns coincidence time and a 'delay before burst' (DBB) setting of 800 ns. Following the first three measurements, which were performed to establish stability of the samples, the vials were quenched using a solution containing 10 % nitromethane to give tritium efficiencies in the range of 35-50 %. Results were recorded as counts per minute for each vial and corrected for radioactive decay.

3.3.1.3 Modelling of efficiencies

The MICELLE2 Monte Carlo simulation code (Kossert and Carles, 2010) was used to model the efficiencies of the liquid scintillation counter for ^{89}Zr relative to ^{3}H. Input files (Appendix 1: MICELLE2 input files) were prepared using existing nuclear data taken from DDEP (Bé et al., 2016), and an efficiency curve was generated. A quadratic curve was fitted to the efficiency values and the fitting parameters were then used to determine the zirconium efficiency relative to the tritium efficiency, normalised to the quench parameters measured during the source sampling. In order to determine a variance due to potential differences in sample composition, geometry and nuclear data, a sensitivity analysis was performed. The parameters were varied and quadratic curves fitted (Figure 3-2). In addition to this, the modelling was also repeated using the CN2005 Monte Carlo simulation software, to verify the MICELLE2 results. The results indicated an average 0.3% bias in the CN2005 values (on tritium efficiencies between 35 and 50 %) compared to those from MICELLE2, when using the same input parameters. This is within the uncertainty of the fit, and the slightly higher results are likely due to differences in the underlying model (MICELLE2 considers more interactions than CN2005).

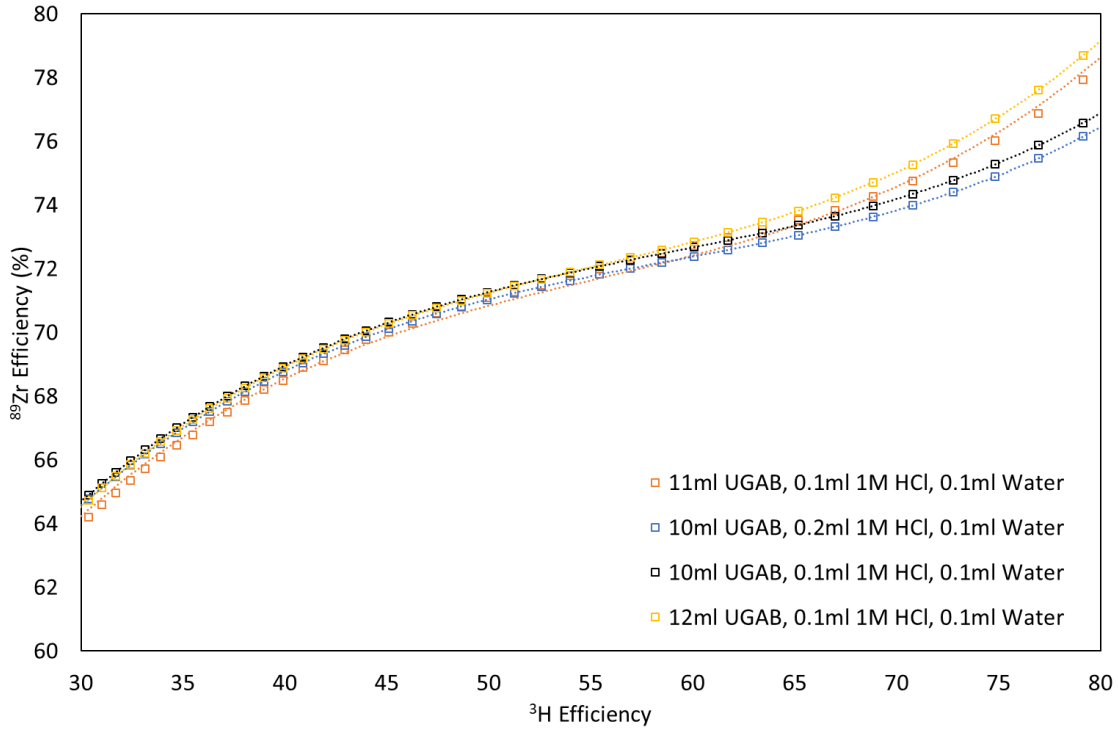

Figure 3-2: Modelled efficiency curves from MICELLE2 for different volumes of scintillant and carrier. The black dataset (10ml UGAB, 0.1ml HCl, 0.1ml water) represents the chemistry used in the source preparation and was used for the calculatons. Error bars have been omitted for clarity.

3.3.1.4 Sample stability

The first three measurements were used to determine the stability of the liquid scintillation samples prior to quenching. Average count rates (after correction for decay and mass) were calculated for each set of vials and compared (Figure 3-3).

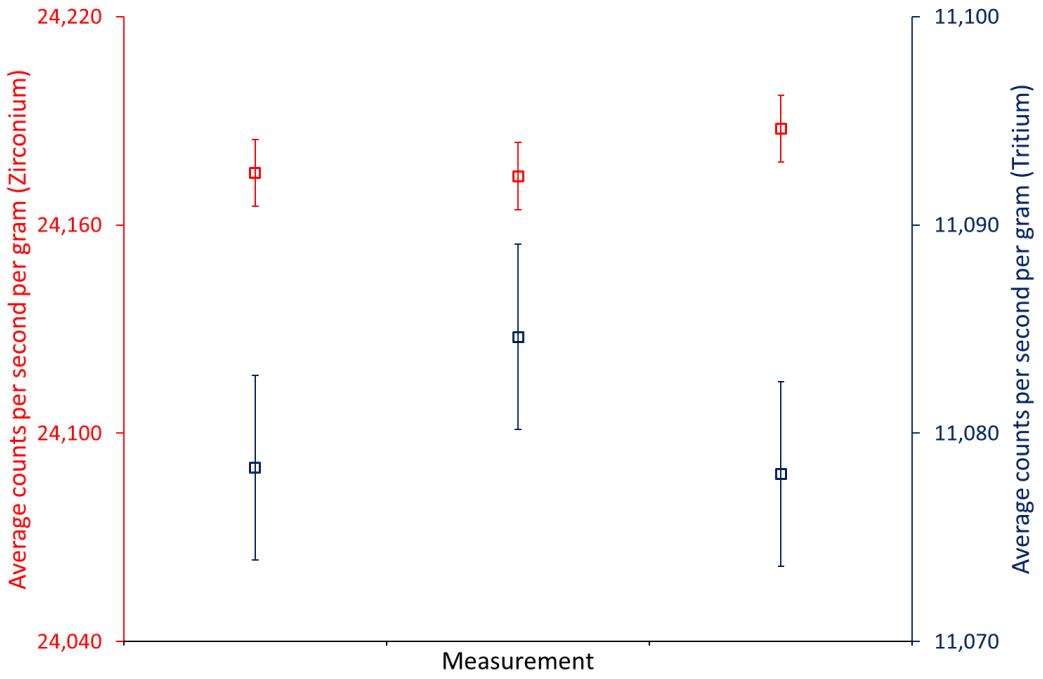

Figure 3-3: Plot of sample stability for liquid scintillation vials prior to quenching. Red points represent zirconium samples and follow the left axis, blue points represents the tritium vials and follow the right axis.

3.3.2 Beta-gamma coincidence counting

Aliquots of ^{89}Zr in 2M hydrochloric acid ranging from 1-2 drops (~0.03 g) up to 0.1 g were dispensed to liquid scintillation vials containing 10 ml of UGAB scintillation cocktail. The equipment consisted of a light-tight chamber housing two closely matched photomultiplier tubes connected in a coincidence circuit to eliminate dark current, situated atop a high-purity germanium detector, with a thin aluminium window between the light-tight chamber and the detector face (Figure 2-14). The PMT voltage was initially set at 1700 v but subsequently increased to 2300 v in order to better resolve the Auger and low energy x-ray emissions. Data was collected as a series of time-stamped pulses in both the beta and gamma channels, with coincidence gates, resolving time and dead time correction being applied during the processing steps. These measurements were repeated using different scintillants (Optiphase Hi-safe3 and Ultima Gold LLT) but little difference in relative counting rates was observed.

3.4 Methodology: secondary standards

Secondary standards are essential in disseminating primary measurements to the user community. This is generally achieved using ionisation chambers which are both sold as 'radionuclide calibrators' for use in clinical departments and as stand-alone chambers for use in industrial applications. Both systems rely on a response function (known as a calibration factor or dial setting) to convert energy deposited within the sensitive region of the chamber into an activity. Many factors affect the response of ICs and, therefore, extensive measurements must be performed in order to determine the overall uncertainty on any derived response function.

3.4.1 Vinten 671 measurements

To determine calibration factors for the Vinten 671 secondary standard ionisation chamber, a series of ampoules and vials (Table 3-2) were filled gravimetrically from a standardised stock solution of ^{89}Zr with an activity of 5.116 MBq g^{-1}. The ampoules and vials were measured on the Vinten 671 system using dedicated ampoule holders (Figure 3-4) and a dedicated current measurement system (described in section 3.5.2). The activity was chosen such that approximately 50 pA g^{-1} was observed in the chamber and, therefore, uncertainties due to current measurement would be minimised.

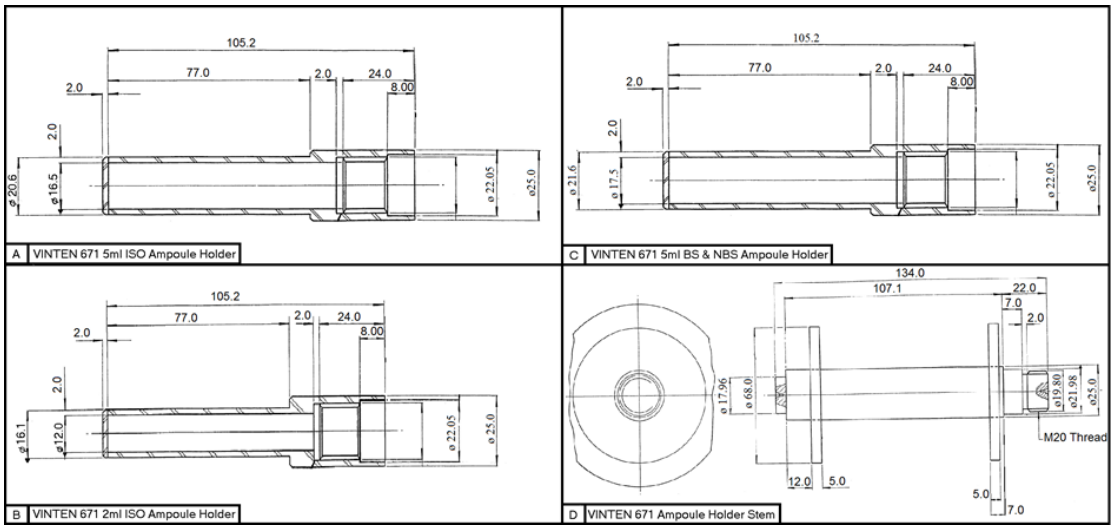

Figure 3-4: Ampoule holders used for ampoule and vial measurments on the Vinten 671 system. Holder C was not used in this study but is shown here to demonstrate the subtle differences in holder design.

Container ID	Container Type	Nominal fill volume	Mass
A180608	2ml ISO Ampoule	1 ml	1.09037 (21)
A180609	2ml ISO Ampoule	1 ml	1.00961 (18)
A180610	2ml ISO Ampoule	1 ml	1.04645 (15)
A180611	2ml ISO Ampoule	1 ml	0.99832 (16)
A180614	5ml ISO Ampoule	3 ml	3.02455 (35)
A180615	5ml ISO Ampoule	3 ml	3.01650 (31)
A180616	5ml ISO Ampoule	3 ml	3.00877 (32)
A180617	5ml ISO Ampoule	3 ml	3.13067 (28)
B180699	10ml Schott Vial	4 ml	4.06948 (26)
B180700	10ml Schott Vial	4 ml	4.02412 (33)
B180701	10ml Schott Vial	4 ml	4.03678 (37)
B180702	10ml Schott Vial	4 ml	4.02221 (34)

Table 3-2: Details of ampoules and vials used to determine calibrations factors on the Vinten 671 system.

3.4.2 Radionuclide calibrator measurements

Measurement of the four 10 ml Schott vials were made at NPL on a Capintec CRC-25R, Capintec CRC-12, (Capintec, USA) and Atomlab 500 (Biodex, USA) radionuclide calibrators using the manufacturer recommended dial setting for ^{18}F. So that the dial settings could be adjusted once the primary standardisation was completed and true activity known, a long-lived check source was placed into the chamber and the dial setting was adjusted through its range. This must be done with Capintec devices due to the non-linear relationship between the dial setting and activity reading. By comparing the activity reading with the true activity, the dial settings can then be modified to give the correct reading.

The Capintec CRC-25 PET, located in the pre-clinical scanner room, was calibrated by comparison with the UHW Fidelis using 4 ml of ^{89}Zr oxalate solution in a 10 ml Schott

vial. The same vial was also sent to NPL to confirm that the calibration factor on the UHW Fidelis is comparable to the Vinten 671 dial setting. The devices at the PETIC site are regularly calibrated for ^{18}F by comparison with NPL during annual accuracy checks.

3.4.3 SIRIC predicted calibration factors

Ionisation chambers in use at NPL have been calibrated for a variety of radionuclides over the past 50 years. Using mathematical and Monte Carlo based models, it is possible to predict the response function for a radionuclide in an existing geometry using available nuclear data. The 'SIRIC' programme was developed by NPL and the BIPM for the purposes of predicting calibration factors for the systems used at the BIPM for international comparison exercises. Using SIRIC and the nuclear data evaluated by DDEP, a calibration factor of 11.265 (38) pA/MBq was derived for 3ml of solution in a 5ml glass flame-sealed ampoule in the NPL secondary standard ionisation chamber. This value can act as a guide when determining new calibration factors from primary measurements, but cannot be considered as traceable and must be validated by independent measurements.

3.5 Methodology: half-life determination

A new half-life was determined using two techniques: high resolution gamma spectrometry with a high purity germanium detector and measurement of the decaying current observed in an ionisation chamber.

3.5.1 Experimental arrangement

3.5.1.1 Source preparation

A high purity sample of ^{89}Zr oxalate was received from Perkin Elmer and diluted using 10 ml of 1 mol dm^{-3} hydrochloric acid. Due to the small volume of oxalate solution (<0.1 ml) it was not deemed necessary to perform a chemical conversion of the oxalate solution prior to dilution. Nominal activities of 1 MBq contained in 1 ml aliquots were dispensed to 2 ml ISO ampoules (ISO, 2010) for measurement by HPGe detectors.

Approximately 70 MBq contained in 5 ml of solution was dispensed to a 5 ml ISO ampoule (ISO, 2010) for measurement on a re-entrant type ionisation chamber.

3.5.2 Half-life measurement by ionisation chamber

The 5 ml ISO ampoule was measured on the NPL 'PA782' secondary standard ionisation chamber (Collins et al., 2015) for 448 sets of 10 cycles, on 115 occasions in which the ampoule was removed and replaced in the ionisation chamber. The measurements were taken over 7.26 half-lives (23.7 days). The back-to-back arrangement of this ionisation chamber allows for lower backgrounds and improved stability during the measurements compared with a standalone chamber. Quality assurance, consisting of background and ^{226}Ra measurements, were performed throughout the campaign to determine stability of the system, and a plot of the residuals of the radium measurements is shown in Figure 3-5. The ionisation chamber was connected to a current measurement system, which employs a calibrated DATRON 1061 digital voltmeter (DVM) to determine the voltage across a calibrated capacitor at defined time points. These measurements are then used to calculate an observed rate of change of voltage (V s^{-1}) for each measurement cycle and the observed current is calculated using the simplified Equation 3-1, where I is the ionisation chamber current (typically measured in pA) and C is capacitance (in pF).

$$I = C\frac{\mathrm{dv}}{\mathrm{dt}}$$

Equation 3-1: Calculation of observed current

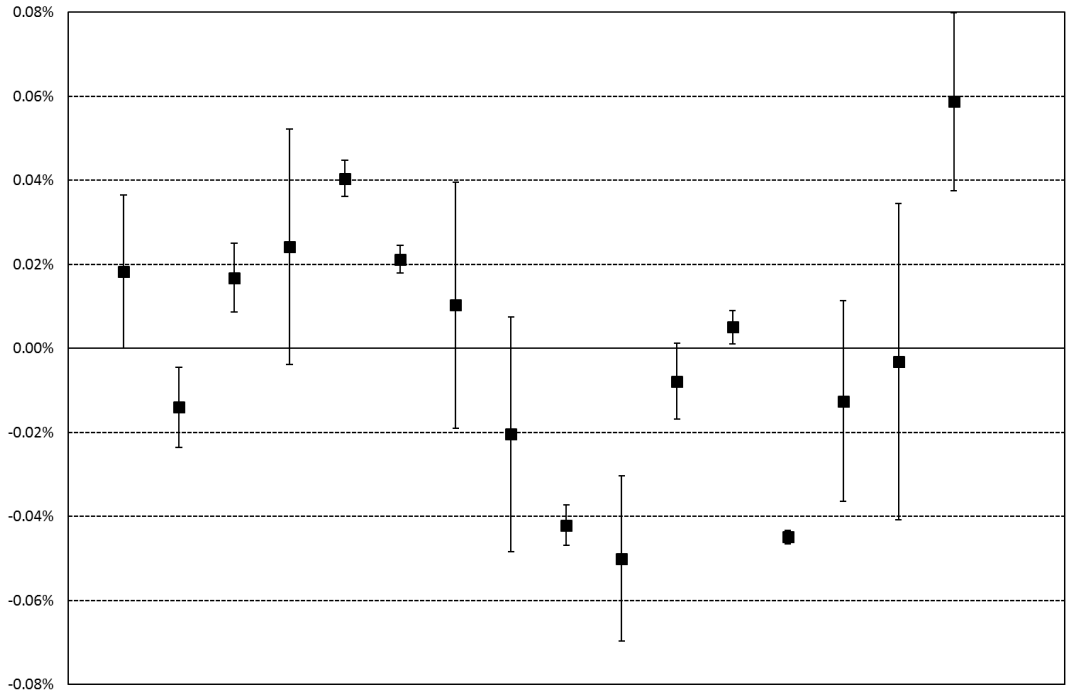

Figure 3-5: Plot of residuals of radium QA measurements

Individual cycle measurements varying between 64 s and 500 s were taken over the course of the campaign. The measured currents were background corrected and a least squares exponential fit was made to the data.

3.5.3 Half-life measurement by gamma spectrometry

The 2 ml ISO ampoule was measured 177 times on a calibrated HPGe detector for a total of 7.72 half-lives (25.2 days). Measurement times varied between 40 minutes and 5.5 hours to maximise the number of counts in the 909 keV photopeak. An ^{241}Am source (main gamma emission at 60 keV) was placed behind the ^{89}Zr ampoule to act as a QA point for all of the measurements; it was also used to verify that the dead time correction was being applied correctly. The existing nuclear data evaluated by DDEP (Bé et al., 2016) were used to determine the presence of any impurities and to give an indication of the activity. Minimum detectable activity (MDA) values of 216 Bq and 16 Bq were determined for ^{88}Zr and ^{88}Y respectively using the Currie method (Currie, 1968). The MDA values represent a potential impurity lower than 0.01% for ^{88}Zr and 0.001% for ^{88}Y at the end of the measurement campaign. The collected spectra were analysed using

the Genie2000 (Mirion, USA) peak fitting software. The interactive peak fitting tool was used to manually fit the 909 keV gamma emission, and the background corrected area under each peak was used to determine a total number of counts.

3.6 Methodology: determination of relative gamma emission probabilities

3.6.1 Measurements

Three separate sources were prepared and measured between 2017 and 2019. All sources were made from stock solutions of ^{89}Zr prepared in 2ml ISO ampoules. Details of the activities, measurement times and total collected counts in the main fitted photopeak are given in Table 3-3. The ampoule measured in 2018 was prepared from the same stock solution that was standardised by the CIEMAT/NIST efficiency tracing method. All measurements were performed on an n-type semi-planar HPGe with a relative efficiency of 22 % as described by Collins et al. (2019b) which also describes the calibration methodology and electronics. A plot of the efficiency calibration and residuals is taken from this publication and shown in Figure 3-6 for reference.

Source ID (year)	Measurement time (s)	Nominal Activity (kBq)	Measurement number	Total corrected counts in fitted 909 keV peak
A170110 (2017)	83395	61	1	1541665
A180612 (2018)	77230	416	1	9679177
A180612 (2018)	97000	336	2	9819939
A190148 (2019)	7200	879	1	1905502
A190148 (2019)	43200	222	2	2887500
A190148 (2019)	43200	199	3	2585155
A190148 (2019)	43200	178	4	2317319
A190148 (2019)	43200	159	5	2073868
A190148 (2019)	43200	143	6	1860677
A190148 (2019)	43200	128	7	1667629

Table 3-3: Details of sources used for the determination of gamma emission intensities

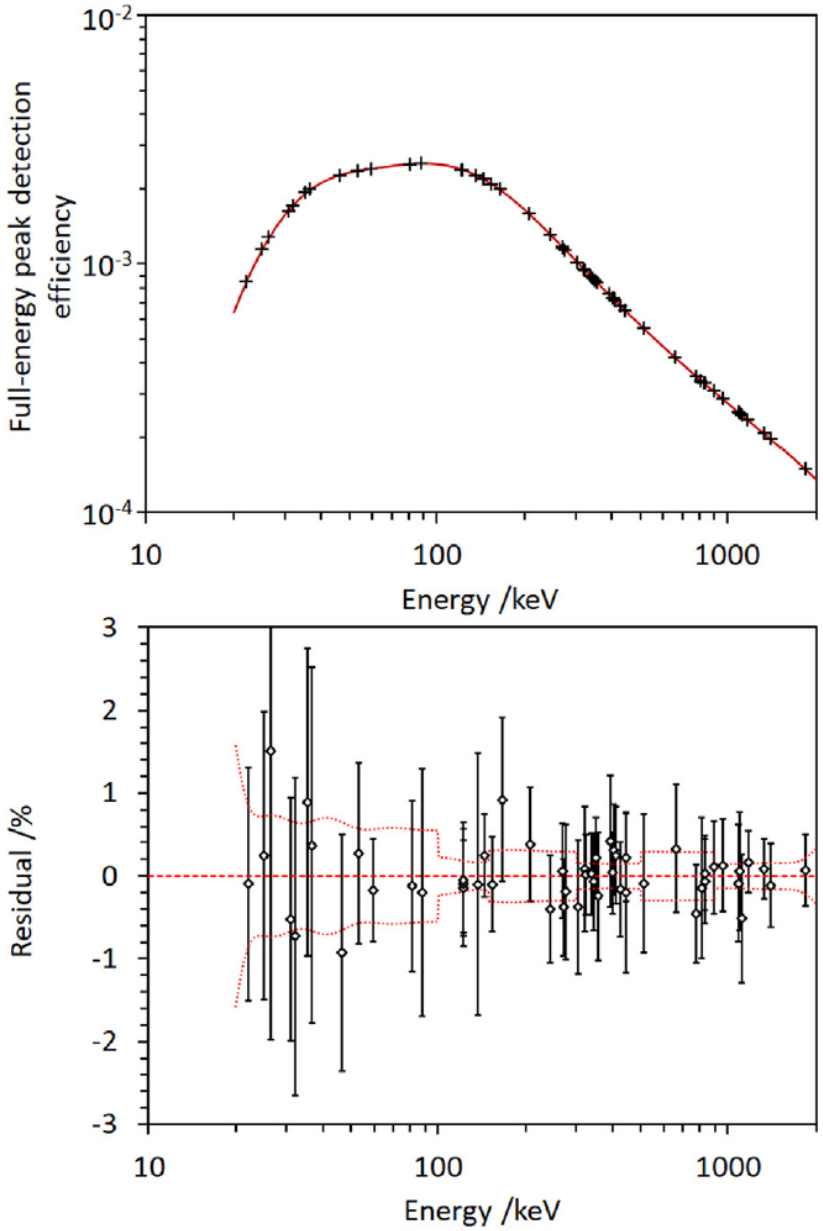

Figure 3-6: Full energy peak detection efficiency and plot of residuals (Collins et al., 2019a)

3.7 Results

3.7.1 Primary standardisation

3.7.1.1 CIEMAT/NIST efficiency tracing

Tritium efficiencies between 35 % and 48 % yielded sample efficiencies between 66 % and 71 % respectively. An activity per unit mass of 5.116 (37) MBq g^{-1} at a reference time of 2018-09-25 12:00 UTC was determined using the MICELLE2 model, and a value of 5.131 (50) MBq g^{-1} at the same reference time was determined using the CN2005 model, after applying a dilution factor of 4.990 (20). Comparison with the activity of 5.128 (64) MBq g^{-1} determined by gamma spectrometry and the ionisation chamber value of 5.123 (64) MBq g^{-1} determined using the modelled SIRIC calibration factor curve, demonstrates statistical agreement between these results (Figure 3-7). The uncertainty components for the CIEMAT/NIST standardisation are shown and described in Table 3-4.

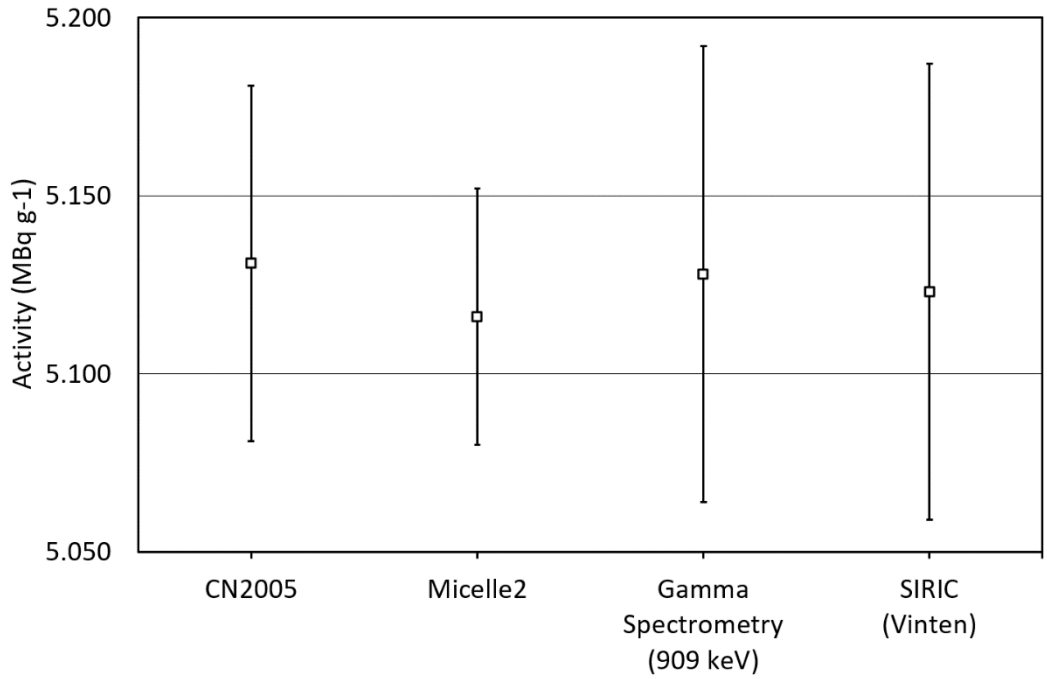

Figure 3-7: Comparison of activity values determined by different techniques

Component	Description	Standard Uncertainty (%)
Counting Statistics	Standard uncertainty due to repeatability and reproducibility of source measurements on LS counter. Calculated by taking standard deviation of activity concentrations	0.24
Background	Standard uncertainty due to background variability. Typical standard deviation of background measurements was 5 %.	0.11
Tracer Activity	Standard uncertainty due to ^{3}H tracer activity concentration uncertainty of 2.5 %	0.42
Decay Correction	Standard uncertainty due to decay correction of ^{3}H and ^{89}Zr to common reference time. Half-life uncertainties of 0.2 % and 0.17 % were used respectively.	0.24
Weighing	Standard uncertainty on masses of active solution dispensed.	0.05
Dead-time	Estimated uncertainty due to dead-time correction performed by LS counter.	0.09
CIEMAT/NIST modelled efficiency calculation	Standard uncertainty on the modelled efficiency curve generated by Micelle. Determined by variation of input factors such as chemistry, volume, kB value and beta shape function. Largest observed difference was 0.72 % and half of this value has been taken.	0.36
Dilution	Standard uncertainty on the dilution factor used between levels. Taken as half of the difference between gravimetric and radiometric dilutions.	0.21
Solution Stability	Standard uncertainty due to the effect of sample stability in both ^{3}H and ^{89}Zr vials.	0.09
Impurity	Standard uncertainty for the effect of impurities estimated using MDA values for ^{88}Y and ^{88}Zr.	0.001
Photon backscatter	Standard uncertainty due to photon backscattering within the LS counter. Value estimated by calculating potential 7 % increase in the efficiency of the 909 keV branch based on the work of (Cassette et al., 2006).	0.18
	Combined standard uncertainty	**0.73 %**

Table 3-4: Uncertainty budget for CIEMAT/NIST standardisation with description of component parts.

3.7.1.2 Beta-gamma coincidence counting

To determine an absolute measurement of activity using this method, it is first necessary to determine the number of β- events, γ events and any coincident β-γ events within a specified time interval. In a perfect system, this would be enough to determine the overall efficiency and, therefore, the activity of any source measured. In practice, consideration must be given to many variables such as the efficiency of the beta counter to gamma events, multiple branches of decay and other emissions such as Auger electrons and x-rays. To correct for this, it is common to use a method of efficiency extrapolation, whereby the efficiency of one channel (typically the beta channel) is varied and the data are fitted and extrapolated to unit efficiency to determine the total activity of the source under study.

Initially a coincidence gamma gate was set on the 511 keV annihilation peak in order to obtain an estimate of the activity. This required raising the lower threshold to exclude the Auger and x-ray part of the spectrum and count the positrons. However, due to the interference from the Auger electrons and x-rays, a non-linear trend was identified in the dataset.

Further attempts were made to fit the data using a variety of coincident gamma gates set on the other major photon energies. However, the very low energy (1.27 – 1.89 keV) auger electrons may not have been counted due to the setting of the beta threshold and sensitivity of the PMTs, which would cause divergence of the fit from a linear model. The data recorded did not enable the determination of an absolute activity value at this time, but has highlighted the difficulties in using this method for the standardisation.

3.7.2 Secondary standards

From the CIEMAT/NIST measurements and using the MICELLE2 model, an activity of 5.116(36) MBq g^{-1} was calculated for the stock solution at a reference time of 2018-09-25 12:00 UTC after the application of the dilution factor. The standardised

solution was used to determine calibration factors for the NPL secondary standard ionisation chamber. Other sources prepared between 2015 and 2019 were used to determine dial settings for the commercially available radionuclide calibrators and these are shown in Table 3-5.

Chamber	Geometry	Volume (ml)	Calibration Factor (pA/MBq)	Dial Setting	Standard Uncertainty (%)
Vinten 671	2ml ISO Ampoule	1	11.281	-	0.74
Vinten 671	5ml ISO Ampoule	3	11.220	-	0.74
Vinten 671	10ml Scott Vial	4	11.193	-	0.74
SIRIC (Vinten 671 Model)	2 ml BS Ampoule*	1	11.26	-	1.24
Capintec CRC-25R	10 ml Schott Vial	4	-	486	1.35
Capintec CRC-12	10ml Schott Vial	4	-	483	1.68
Atomlab 500	10ml Schott Vial	4	-	10.1	1.25

Table 3-5: Calibration factors and dial settings determined for a range of radionuclide calibrators.

Previous work found dial settings for the Capintec family of radionuclide calibrators to be 465, 510, 504 and 514 for geometries similar to that used in this study (Avila-Rodriguez et al., 2007; Beattie et al., 2014; Verel et al., 2003; Wooten et al., 2016). This work suggests that the Capintec recommended value of 465 is approximately 3% low. This could be attributed to historic inaccuracies of the Capintec positron emitter dial settings or the effects of geometry (3 ml ampoule compared to 10 ml vial). Other values reported for the Capintec calibrator show an opposite 3 % discrepancy, although the geometries used in these studies are significantly different to those used in this study. In contrast, the recommended Atomlab 500 dial setting is within 2% of the value determined in this work. The theoretical model of the response of the NPL Vinten 671 ionisation chamber (SIRIC) (Cox et al., 2007) was used to determine a calibration factor for a 2 ml BS

ampoule, which is a close approximation to the 2 ml ISO ampoule used in this study and the calibration factors determined are in statistical agreement.

3.7.3 Half-life determination

3.7.3.1 Ionisation chamber

Figure 3-8 shows a plot of the residuals for the exponential fit of the ionisation chamber data. The gaps in data collection indicate intervals where QA and background checks (or other necessary measurements) were undertaken. The least squares fit to the data yielded a half-life value of 78.366 (31) hours and this is reported in Table 3-6 alongside the uncertainty budget.

Uncertainty Component	σ_A/A (%)	n	Factor	$u(T_{1/2})/T_{1/2}$ (%)
High Frequency				
Standard Deviation of Residuals	0.081	115	0.1425	0.0116
Medium Frequency				
Ionisation chamber stability	0.031	1	1.0854	0.034
Geometric Repeatability	0.070	115	0.1425	0.010
Low Frequency				
Background	0.00024	1	1.0854	0.00027
Impurities	0.010	1	1.0854	0.011
Linearity	0.010	1	1.0854	0.0109
$T_{1/2}$ (hours)	**78.366 (31)**	**Combined % uncertainty**		**± 0.040 %**

Table 3-6: Half-life and uncertainty budget for ionisation chamber measurements

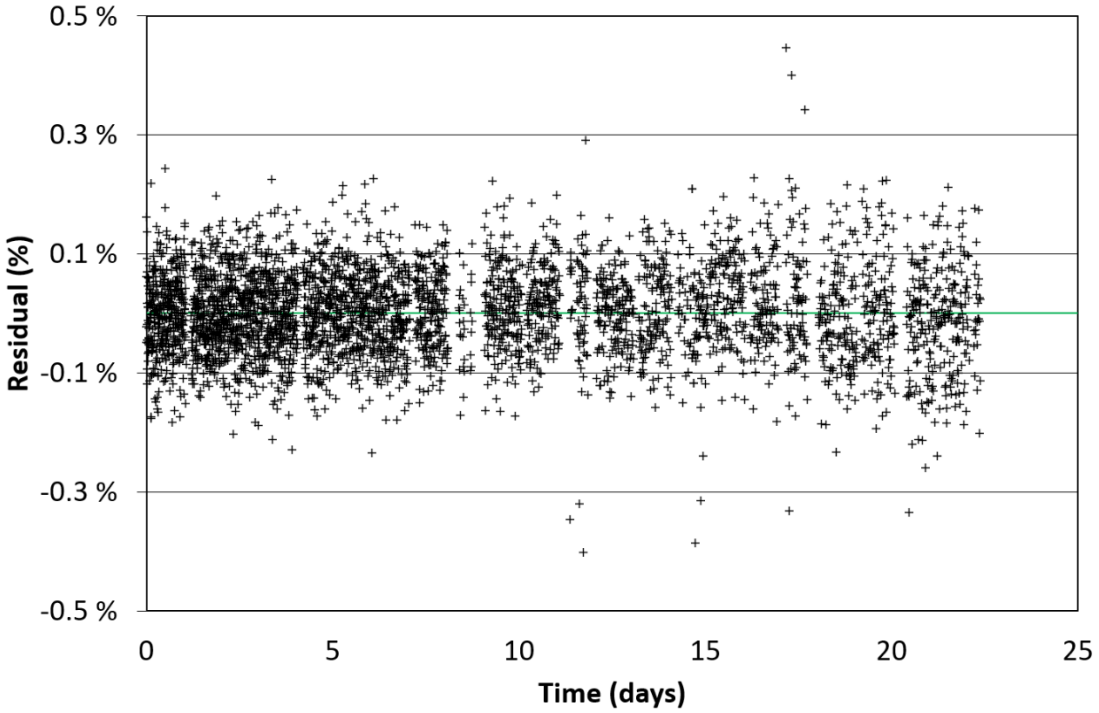

Figure 3-8: Plot of the residuals of all data points from the ionisation chamber half-life dataset

The uncertainty was determined using the method described by Pommé et al. (2008) whereby high, medium and low frequency components are propagated using Equation 3-2. In this equation T represents the duration of the measurement programme, λ represents the decay constant, n is the number of times each uncertainty component is observed and $\frac{\sigma_A}{A}$ represents the value of the uncertainty component.

$$\frac{\sigma_{T_{1/2}}}{T_{1/2}} \approx \frac{2}{\lambda T}\sqrt{\frac{2}{n+1}}\frac{\sigma_A}{A}$$

Equation 3-2: Uncertainty propagation formula presented by Pommé (2008)

The components of the uncertainty budget were classified as follows:

High Frequency components relate to the statistical nature of the measurements and are calculated by determining the standard deviation of the residuals. In this measurement, the high frequency components have a small contribution to the overall uncertainty due to the large number of measurements taken.

Medium frequency components are considered by looking at trends in the residuals and the geometric repeatability of the ionisation chamber. Small trends were identified in the residuals of the radium QA measurements and a standard deviation of the residuals was included to form the detector stability component. The geometric reproducibility was difficult to identify in this work, due to the relatively small number of repeated measurements undertaken over a short time period. Therefore, a value of 0.07 % was assigned to this component by using historic QA data of the ionisation chamber itself.

Low frequency components are considered as the long-term stability of the ionisation chamber, and are identified as the linearity of the chamber and DVM, the effect of background correction and the maximum error that could have been noted from the presence of undetected impurities. The linearity of the DVM was taken from calibration certificates which indicated a linearity of better than 0.01 % during measurement. The background component was calculated by taking an estimated 5 % bias and propagating this through to the maximum error that would be observed in the calculated half-life during the course of the measurement. The effect of impurity was determined by using the calculated MDA values (see section 3.5.1) from gamma spectrometry measurements, which gave 0.01 % for ^{88}Zr and 0.001 % for ^{88}Y at the end of the measurement campaign. These were normalised to account for chamber response relative to ^{89}Zr by the use of predicted response factors based on available nuclear data.

3.7.3.2 Gamma spectrometry

A non-linear least squares exponential fit was made to the number of counts determined in the 909 keV peak from each measurement, and this gave a half-life of 78.375 (78) h. Figure 3-9 shows a plot of the residuals of the fitted dataset and Figure 3-10 shows a plot of the residuals of the ^{241}Am QA measurements undertaken at the same time. The relatively small uncertainties are attributed to the higher efficiency of the detector at lower gamma energies.

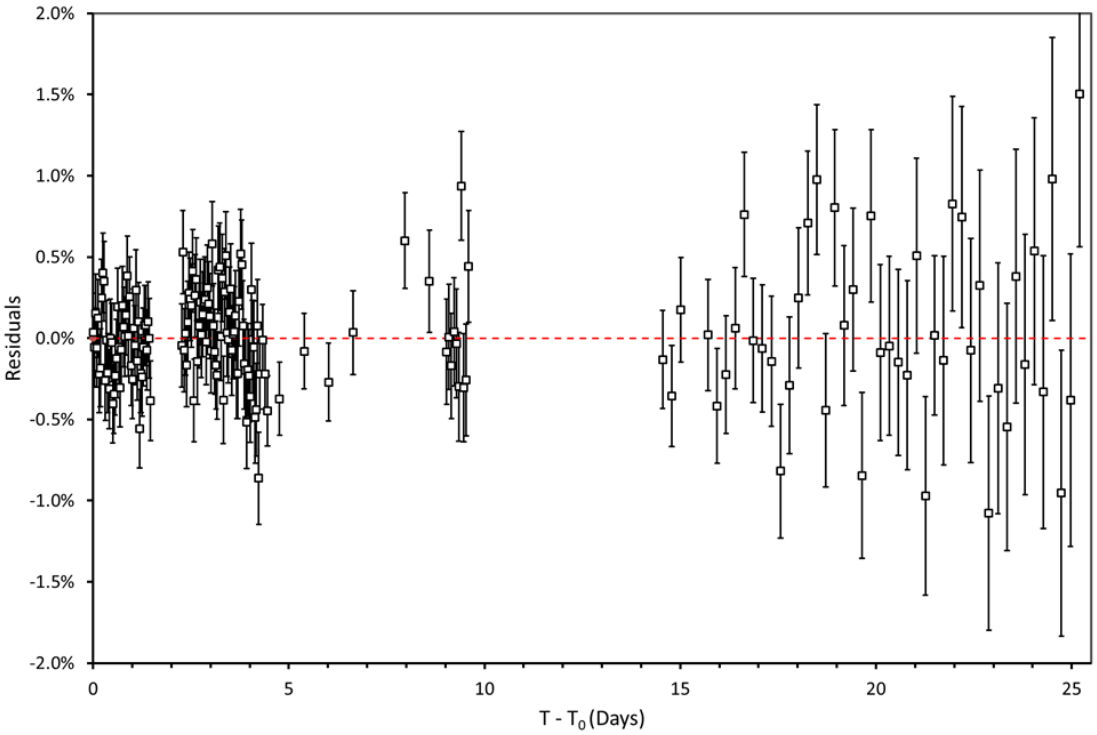

Figure 3-9: Plot of the residuals of the gamma spectrometry measurements considered in the half-life determination

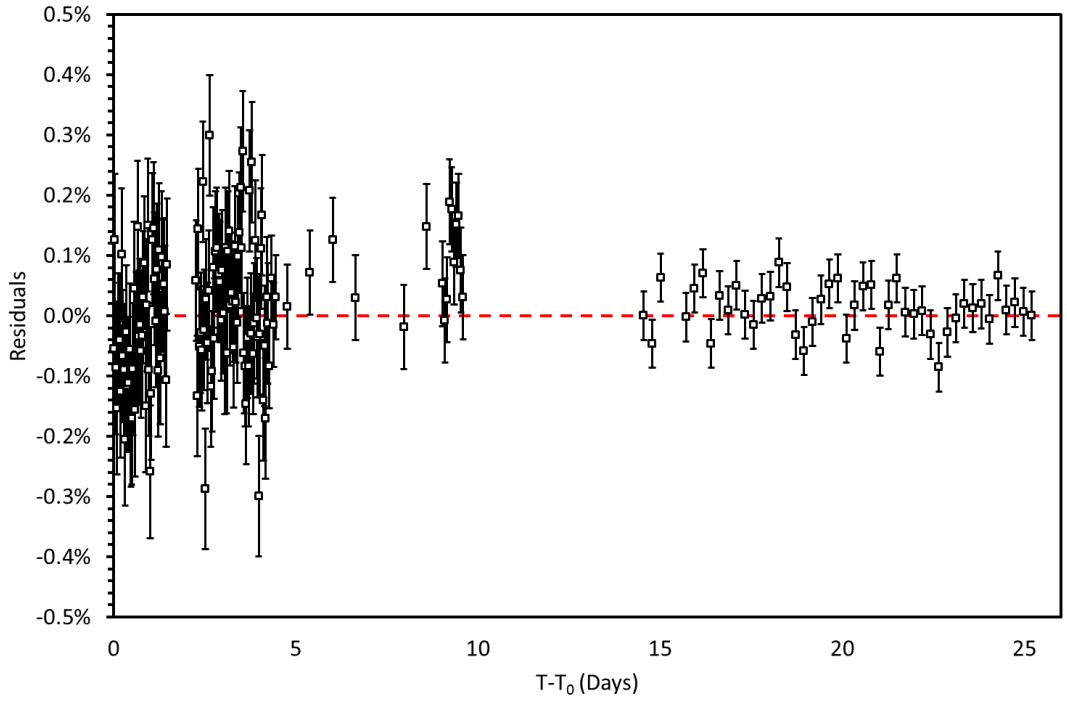

Figure 3-10: Plot of the residuals from the ^{241}Am QA measurement

Uncertainties were calculated in the same manner as described in section 3.7.3.1 and using high, medium and low frequency values propagated using Equation 3-2. In this

instance, the high, medium and low frequency components were determined as shown below and are reported in Table 3-7.

The high frequency component was determined to be the standard deviation of the residuals of the fitted 909 keV peaks.

The medium frequency components consisted of an estimated value of 0.1% for geometric reproducibility, and a measurement stability value determined from the standard deviation of the residuals of the fitted ^{241}Am 60 keV peak data.

In general, low frequency uncertainties cannot be obtained from the measured dataset and, therefore, several assumptions have been made based on historic information regarding the detector. The long-term efficiency stability of the detector was calculated by using daily QA measurements and by determining a standard deviation of the residuals of the six months of data surrounding the measurement campaign. An uncertainty due to the peak fitting process was estimated to be 0.15 %, based on a worst-case scenario of the fitting of the smallest peak used in the dataset. To determine the dead-time and pulse pile up correction component, a 5 % uncertainty was applied to the correction factor and propagated using the median recorded dead time value.

Uncertainty Component	σ_A/A (%)	n	Factor	$U(T_{1/2})/T_{1/2}$ (%)
High Frequency				
Standard Deviation of Residuals	0.275	177	0.040	0.011
Medium Frequency				
Detector stability	0.099	1	0.374	0.037
Geometric reproducibility	0.10	1	0.374	0.037
Low Frequency				
Background	0.090	1	0.374	0.034
Peak Fitting	0.15	1	0.374	0.056
Dead time / pulse pile-up	0.095	1	0.374	0.036
Efficiency stability	0.099	1	0.374	0.037
$T_{1/2}$ (hours)	**78.375 (78)**	**Combined % uncertainty**		**± 0.099%**

Table 3-7: Uncertainty components and result of the gamma spectrometry half-life measurement.

3.7.4 Determination of relative gamma emission probabilities

Peaks were manually fitted to each measurement and the area under the peak calculated and corrected for density and efficiency. Gamma emission probabilities were then determined relative to the corresponding 909 keV gamma peak in each spectrum and an average of the 7 measurements was calculated. Initially, the limitation of relative statistical weight method (LWM) was used to determine a mean of the dataset. However, inconsistencies became apparent in the data due to the small uncertainties of two values and it was decided to use a power moderated (weighted) mean (PMM) as described by Pommé and Keightley (2015). The mean results are shown in Table 3-8 and the individual results used in the calculation are shown in Figure 3-11, alongside the PMM value. As the 2018 measurements were performed using the solution standardised in section 3.3.1, an absolute gamma emission probability for the 909 transition was determined to be 0.9914(78).

The main uncertainty components in the emission intensity data are peak fitting and low counting statistics for the less intense gamma emissions. The PMM determines an overall uncertainty for the dataset including contributions from each of the 10 measurements alongside any additional uncertainty as given in Table 3-8.

Energy (keV)	I_γ	$u(I_\gamma)$	α	χ^2	U (additional) (%)	n
1620.81	0.06756	0.00080	1.7	1.196498	0.0129	10
1657.56	0.0980	0.0014	1.7	1.665824	0.034	10
1713.1	0.7393	0.0021	1.7	0.85	-	10
1744.72	0.1225	0.0015	1.7	1.62	0.035947937	10

Table 3-8: Mean gamma emission intensities of ^{89}Zr relative to the 909 keV gamma emission with associated uncertainty, fitting parameters, reduced chi-squared value and number of measurements.

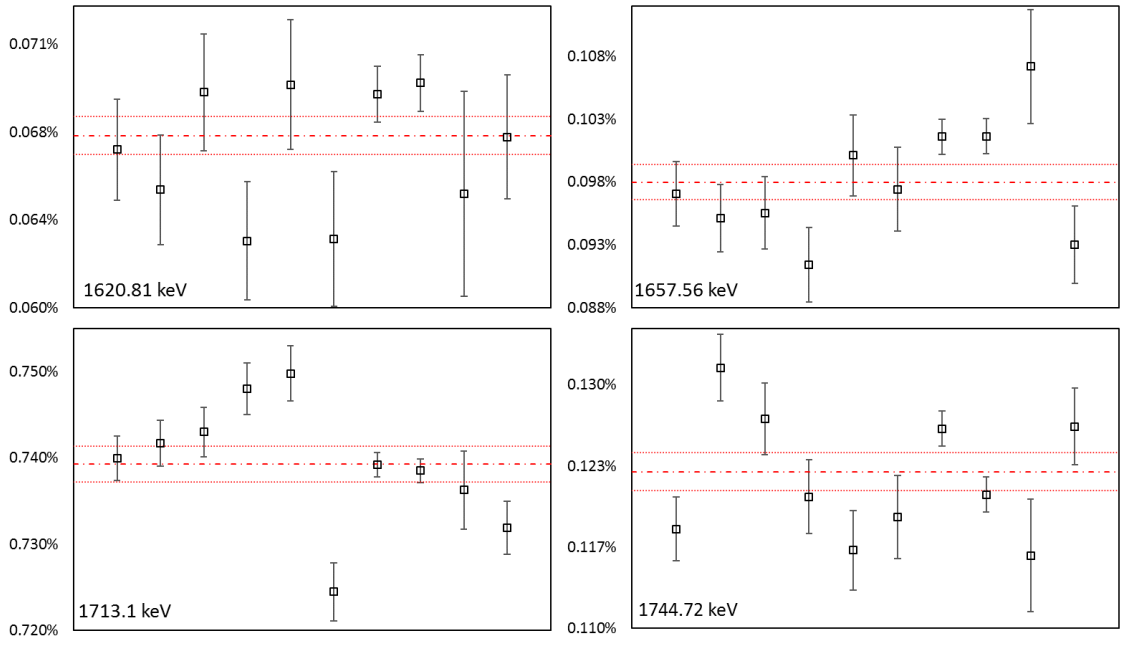

Figure 3-11: Plot showing data used to determine PMM emission probabilities relative to the 909 keV emission. The x-axis is the measurement number corresponding to the 10 measurements used to determine the PMM and has been omitted for clarity.

3.8 Evaluation of nuclear data

There are many techniques available to evaluate nuclear data, but the most widely accepted method in this field is to use the LWM, allowing for rejection based on lack of uncertainty or the identification of an outlier using Chavuenet's criterion (Chavuenet, 1871). The half-life evaluation was performed using the LWEIGHT programme and resulted in 6 results being rejected from the dataset, mostly due to a lack of published uncertainties (Table 3-9). The final value was determined to be 78.362 (23) hours with a χ^2 value of 1.15 and critical value of 2.51, which indicates a consistent dataset. Figure 3-12 shows the non-rejected results plotted alongside the evaluated value.

The gamma emission intensity data were evaluated using the same techniques and new relative gamma emission intensities are shown in Table 3-10, with Figure 3-13 showing the data used in each. For the 1620 keV and 1658 keV transitions, there is a large change in value, and in all datasets, the overall reported uncertainty has been significantly reduced. Collected works (Arlt et al., 1971; Baillie et al., 1979; Draper and McCray, 1968; Gunnink et al., 1969; Heath, 1974; Hinrichsen, 1968; Monaro et al., 1961; Robinson et al., 1969; Van Patter and Shafroth, 1964) were used in this evaluation, with some values excluded due to a lack of uncertainties or using Chavuenet's criterion.

Reference	Reported Half-life (hours)	Uncertainty (hours)	Relative weight (%)	Accept/Rejected
(Sagane et al., 1938)	70			Reject (uncertainty)
(DuBridge and Marshall, 1940)	78	1	0.00053	Accepted
(Sagane et al., 1940)	68	2		Reject (outlier)
(Hyde and O'Kelley, 1951)	77			Reject (uncertainty)
(Shure and Deutsch, 1951)	79.3			Reject (uncertainty)
(Katz et al., 1953)	78			Reject (uncertainty)
(Shore et al., 1953)	79	2	0.00013	Accepted
(Hamilton et al., 1960)	79	0.5	0.0021	Accepted
(Rayburn, 1961)	79.4	1.6	0.00021	Accepted
(Howe et al., 1962)	79			Reject (uncertainty)
(Van Patter and Shafroth, 1964)	78.43	0.08	0.083	Accepted
(Robinson et al., 1969)	78	0.2	0.013	Accepted
(Skelton and Kavanagh, 1984)	78.62	0.17	0.018	Accepted
(Garcia-Torano et al., 2018)	78.333	0.038	0.37	Accepted
This Work	78.367	0.029	0.53	Accepted
Evaluated $T_{1/2}$ (hours)				**78.362 (23)**

Table 3-9: Half-life data considered in the evaluation

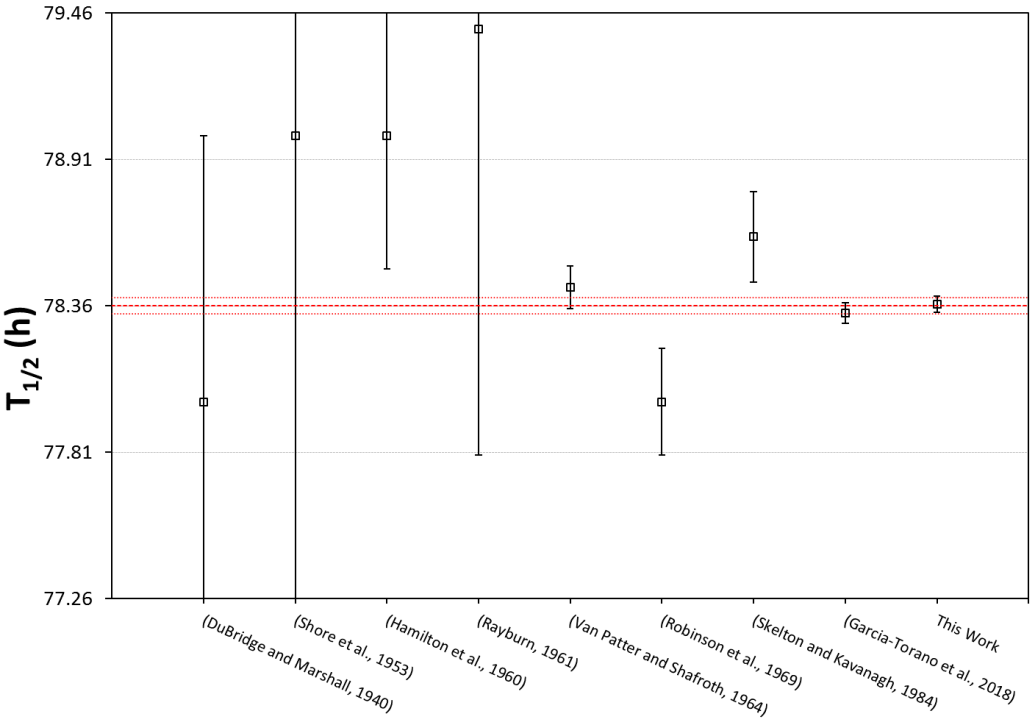

Figure 3-12: Plot of values used in the evaluation. The red line indicates the evaluated value and its associated uncertainty.

Energy	This Work	DDEP	Δ (%)	ENSDF	Δ (%)
1620.81	0.068 (1)	0.075 (5)	10.3	0.074 (5)	8.8
1657.56	0.100 (2)	0.107 (5)	7.0	0.107 (5)	7.0
1713.1	0.741 (3)	0.752 (10)	1.5	0.752 (13)	1.5
1744.72	0.124 (2)	0.124 (4)	0.0	0.124 (4)	0.0

Table 3-10: New evaluated relative gamma emission values compared against existing published data

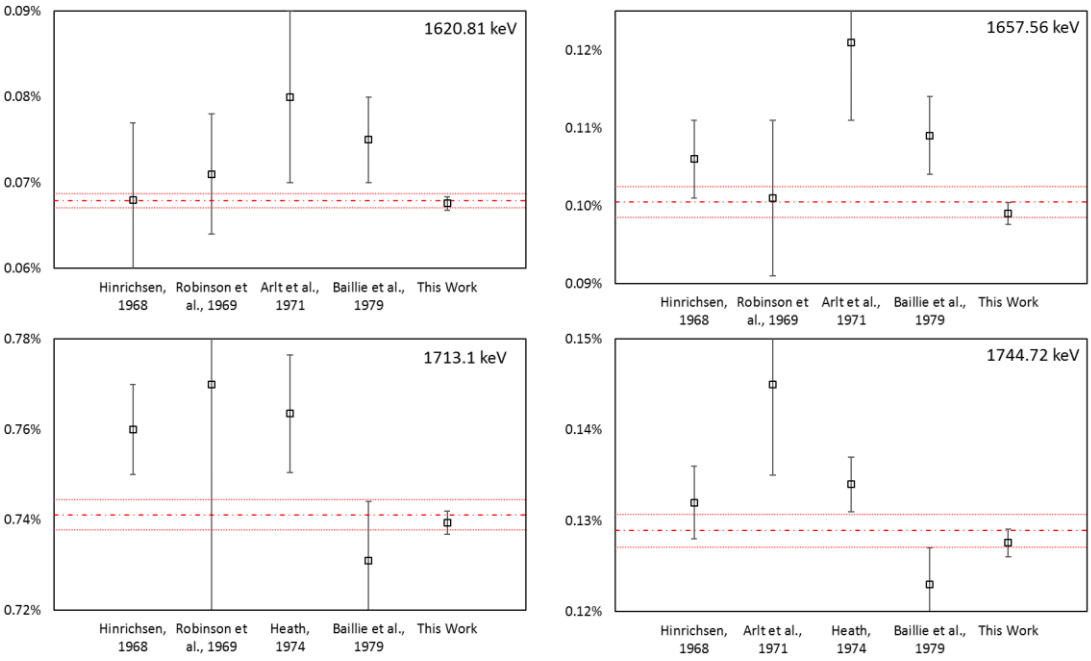

Figure 3-13: Gamma emission intensities plotted alongside this work and the newly evaluated value.

3.9 Chapter summary

This chapter has presented the following results:

- Overview of existing nuclear data for ^{89}Zr.
- Determination of new half-life by two methods and evaluation of this result alongside existing data.
- Primary activity standardisation of ^{89}Zr.
- Presentation of calibration factors and dial settings for secondary standard ionisation chamber systems at NPL and dial settings for commercially available systems used in the clinical setting.

A new value of the half-life has been determined and evaluated alongside existing data and the new result is presented with a consistent dataset. New gamma emission intensities have been determined for 4 gamma transitions and an absolute intensity for the 909keV gamma transition is reported. The collected data have been evaluated alongside existing data, and significant differences of up to 10 % from the existing

evaluated data have been identified. Calibration factors and dial settings for commercially available radionuclide calibrators are presented and indicate a difference of approximately 3% from published values, although it should be noted that the latter were determined for a different geometry than that used in this study. This work has highlighted the need for more measurements of both the calibration factors and the nuclear data for ^{89}Zr. This work provides the basis on which to begin investigations into the accuracy of activity quantification in imaging systems.

Chapter 4:
Preclinical PET imaging of ^{89}Zr

4.1 Introduction

Pre-clinical studies are designed to determine the baseline toxicity, pharmacokinetics and efficacy of the drug or imaging agent in question. These studies are not only crucial to ensure that subjects in future trial phases are administered safe activities, but are also invaluable to estimate uptake and initial expected outcomes of the treatment. Sufficient evidence should be gathered to ensure that human subjects are not exposed to undue risk during future trial phases and therefore the use of mice and rats for testing is commonplace. Pre-clinical imaging of various ^{89}Zr labelled mAbs in animals has been particularly widespread in recent years (Deri et al., 2013). Many of the studies have highlighted the advantages of ^{89}Zr over shorter lived radiometals such as ^{68}Ga or ^{18}F (Baur et al., 2014). It allows the tracking of mAbs over extended periods of time, and thus the development of a better understanding of uptake and long-term residency times.

A series of measurements must be performed to enable imaging system calibration and to verify the accuracy of activity measurement. This chapter aims to address the following aspects of pre-clinical imaging

- Calibration phantoms/objects prepared with traceable activity distributions
- Calibration of the camera system (using manufacturer recommended procedures)
- Verification of the accuracy of the imaging system for ^{89}Zr for simple test objects.
- Assessment of volume-dependent activity recovery (partial volume effect) for ^{18}F and ^{89}Zr.
- Recommendations for measurements to identify key uncertainty components.

It is clear from the applications that any system used in clinical trials should be able to determine activities accurately in a variety of distributions and be repeatable over long periods of time to ensure consistency within and between studies.

It should be highlighted at this point that manufacturers often recommend calibration using a single radionuclide (^{18}F or ^{68}Ge typically) and, therefore, this chapter will cover calibration using the manufacturer recommended method and validation with the radionuclide of interest (^{89}Zr) in line with what is achievable in a clinical setting. This chapter will also review the work undertaken for the primary standardisation of ^{18}F and subsequent calibration of NPL equipment to demonstrate the traceability for this important radionuclide.

4.2 Overview of the Mediso nanoScan-PET/CT system

4.2.1 System specifications

The Mediso nanoScan PET/CT 122S scanner (Figure 4-1) installed at PETIC consists of a LYSO crystal PET module coupled with a high-resolution CT. The longitudinal axis of the scanner is 10 cm and the diameter of the bore is 12 cm which allows for the scanning of a whole mouse in a single field of view (FOV). Details of the system are presented in Table 4-1.

Figure 4-1: Mediso nanoScan PET/CT scanner.

PET maximum longitudinal field of view (Axial FOV)	100 mm
PET maximum Imaging bore diameter (trans-axial FOV)	120 mm
Individual Crystal size	1.12 x 1.12 x 13.0 mm
Number of Crystals	36,504
Spatial Resolution (3D OSEM)	0.7 mm
Spatial Resolution (FBP)	1.25 mm
Sensitivity	8 %
Timing resolution	1.3 ns (Ave.)
Energy Resolution (511 keV)	17.8 % (Ave.)
Reconstructed Voxel Size (minimum)	19.2 µm
CT tube power	80 W
CT tube voltages	35 kVp, 50 kVp, 70 kVp
CT tube current (maximum)	1mA
CT Slice Thickness	0.125
CT maximum image bore diameter (trans-axial FOV)	120 mm

Table 4-1: Details of the Mediso nanoScan PET/CT 122S installed at Cardiff University

4.2.2 Data acquisition

The conversion of detector events into an image involve a number of data processing steps, which are handled by a cluster of computers that accompany the scanner (Figure 4-2). Initial data acquisition and processing is performed by digitiser cards with each card collecting the signals of twelve detectors and performing an analogue to digital conversion. The digitiser cards also perform energy windowing (accepting a limited portion of the energy spectrum by selecting upper and lower energy limits) on the single detector events before sending the information to the other digitiser cards for the coincidence windowing process. This leads to the creation of data packets, which contain

'prompt gamma', 'random gamma' and deadtime information that is transferred to the Teratomo-real PC for further processing.

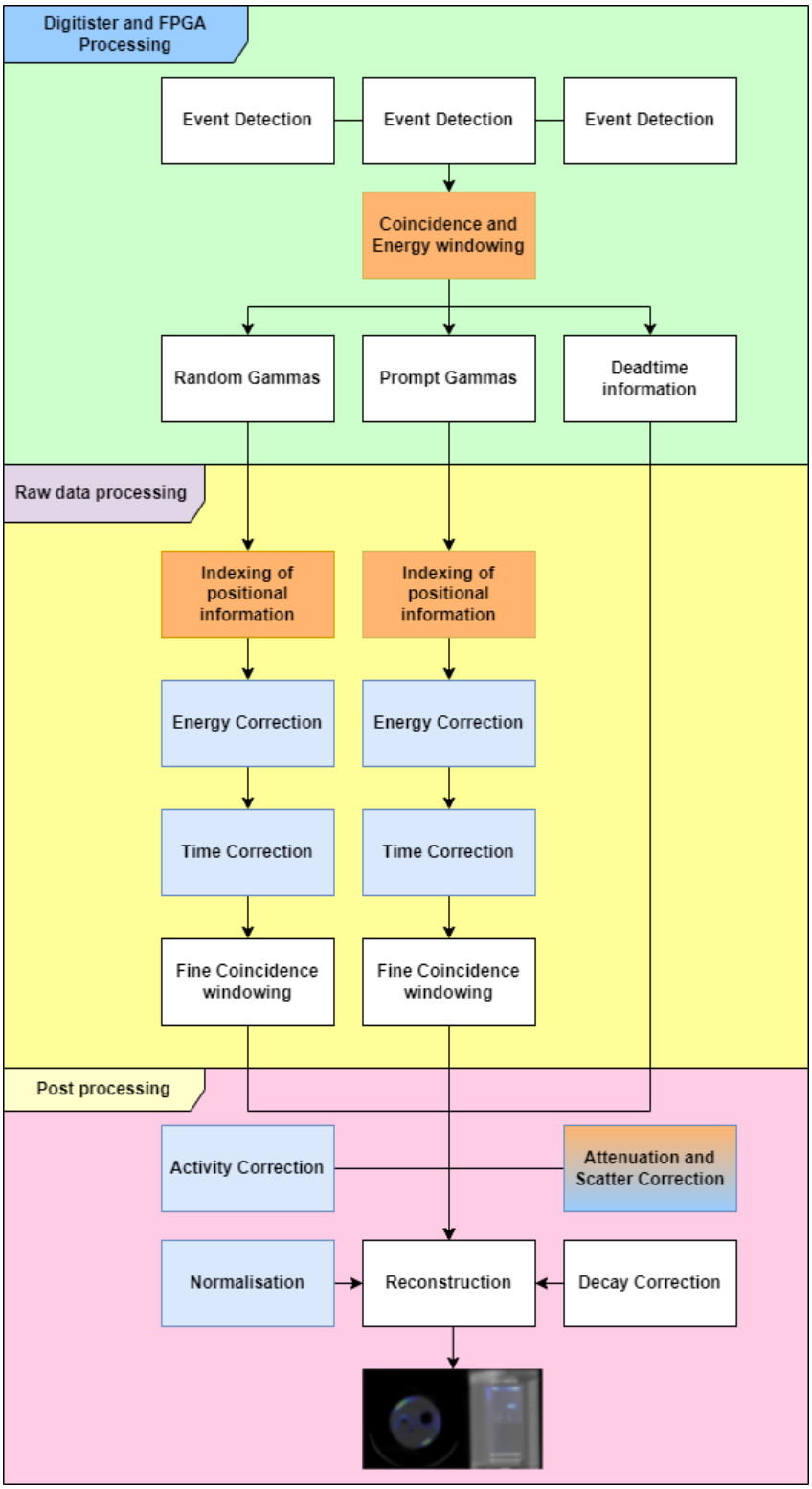

Figure 4-2: Data flow on the Mediso nanoScan PET/CT pre-clincial system. Blue shading indicates the application of a user calibration and orange indicates a manufacturer (factory) calibration. Attenuation and scatter corrections require input from both user and manufacturer.

The Teratomo-real PC (section 4.2.4) refines the data packets so that they are ready for reconstruction, by applying energy and timing corrections and a higher resolution coincidence filtering step. Finally, the data packets are sent to the Teratomo-post computer for reconstruction, whereby the remaining calibrations are applied (activity and normalisation) along with attenuation, scatter and decay corrections.

4.2.3 Digitiser card processing steps

The digitiser card (DCS) begins by classifying analogue event data according to pre-set trigger levels and pulse shapes. Provided a signal is above the lower level discriminator (LLD), the signal is classified as a real event and the pulse is integrated and is timestamped, after the pileup rejection. The DCS collects the single events into packets, which are sent to other digitizer cards, and performs a first level coincidence windowing step to create binary data packages containing event pairs. The Mediso system refers to these as raw data. The DCS also collects delayed random coincidences occurring in the detectors.

4.2.4 Raw data processing (Teratomo-real)

The raw data from the digitiser cards are sent to the Teratomo-real PC, which begins by converting the raw data into ‘list-mode’ data that can be used for reconstruction and further processing. After application of the positional, energy and timing corrections, the output data comprises the crystal index (spatial information) and energy of the event, segmented into coincidence and timing ‘bins’. This binned data is then sent to the reconstruction software which incorporates the remaining calibrations and corrections and form an image.

4.2.5 Manufacturer calibrations

Mediso recommends that service engineers perform an activity calibration and normalisation (with ^{18}F) every 6 months during routine operation. Mediso also provides an ‘activity test’ measurement protocol to determine the accuracy of the system. Should

this fail (whereby a measured activity differs by more than 10 % from the true value), users can instigate the same calibration. Mediso provides a calibration protocol and instructions on how to perform each measurement. It should be noted that calibrations are only performed using ^{18}F and no provision is made for testing or calibration using other radionuclides.

4.2.6 Activity calibration (^{18}F)

The activity calibration determines the factor required to convert count rate to units of activity (Bq), based on a standardised solution being measured in a large volume. This measurement must be performed with a solution of known activity, as any difference will directly affect the accuracy of the quantification. Mediso requires the use of a syringe uniformly filled with 3-5 ml of ^{18}F solution and placed in the centre of the FOV. The calibration allows users to select different reconstruction modes to generate correction factors for standard 2D OSEM and filtered back projection (FBP) techniques, as well as the Mediso 3D 'Teratomo' reconstruction that is the manufacturer preferred reconstruction method.

4.2.7 Normalisation calibration

The normalisation calibration is used to correct for differences in crystal sensitivity. This is performed using the same ^{18}F syringe as for the activity calibration placed at the centre of the FOV, and creating a table of correction factors that adjust the response from each crystal into a standardised output. This correction is applied during the reconstruction process.

4.3 Preparation of calibration phantoms and objects

To calibrate or verify the accuracy of activity measurement in a radionuclide imaging system, it is vital to be able to prepare a variety of radioactive sources with well-known activity concentrations and volumes. The determination of activity (and associated uncertainty) with hospital radionuclide calibrators is addressed in Chapter 3, and this

approach is used to develop a method of producing phantoms and test objects used for imaging system calibration. A flowchart for the preparation of a calibrated phantom is shown in Figure 4-3.

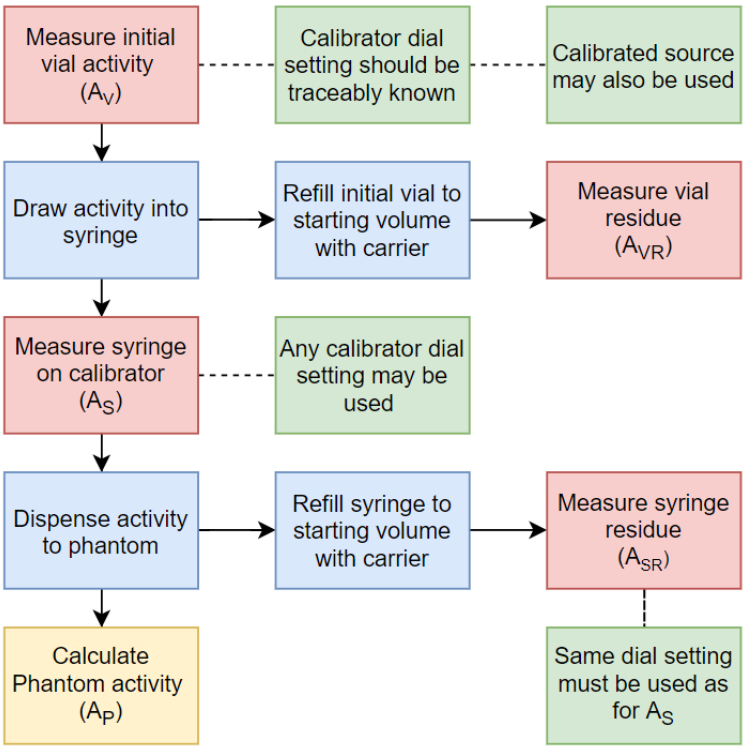

Figure 4-3: Flowchart showing steps involved in filling phantoms using a pre-calibrated source, or a traceably calibrated radionuclide calibrator.

Whether using a calibrated source or a calibrated dial setting, the flowchart uses corrections for losses during dispensing steps to maintain traceability. When applying these corrections, it is not necessary to use known (calibrated) dial settings for each geometry. A ratio can instead be used provided the conditions of measurement remain the same. In the case of the syringe in Figure 4-3, provided measurements are decay corrected to a common reference time, the same starting and residue volumes are used (through the refilling of the syringe with inactive carrier) and the syringe is measured in the same position in the calibrator, a correction can be applied as shown in Equation 4-1. This is discussed in more detail in the following sections.

4.3.1 Use of a radionuclide calibrator or calibrated source

The top of a hospital's internal traceability chain is often a calibrated radionuclide calibrator. This must be calibrated for each relevant radionuclide, and each measurement must be corrected for geometry effects as discussed in Chapter 3. Figure 4-3 shows an example of the methodology required adequately to trace the activity of a phantom throughout the filling process.

Assuming all measurements are decay corrected to a common reference time (t_{ref}) and a calibrated radionuclide calibrator is used with the appropriate geometry, the activity in the phantom (A_P) can be calculated by subtracting the vial residue activity (A_{VR}) from the starting vial activity (A_V) and then multiplying by the complement to the ratio of syringe residue activity (A_{SR}) to syringe starting activity (A_S) (Equation 4-1).

$$A_P = (A_V - A_{VR})\left(1 - \frac{A_{SR}}{A_S}\right)$$

Equation 4-1

4.3.2 Use of weighed aliquots of standardised material

By dispensing aliquots of radioactive material with activity standardised per unit mass, it is very simple to create phantoms with known activities and activity concentrations. This can be done provided that suitably accurate and calibrated balances are available for weighing. In this instance, it is preferable to use multiple balances and adopting the 'double weighing' method, in which the solution is weighed at both dispensing and receipt. This method allows comparison of two independent balance weights and can be used to reduce uncertainty in subsequent weighing stages.

4.3.3 Determination of stock solution activity

The activity and activity per unit mass of the starting solution can be determined by using either a pre-calibrated solution provided by a traceable laboratory, or by measuring an accurately weighed aliquot of the stock solution in a calibrated geometry on a

radionuclide calibrator (or other suitable radiation detector). The former should be accompanied by a calibration certificate listing activity, activity per unit mass, reference time and uncertainty. The stock solution activity should be determined as accurately as possible since, in most cases, it will be the primary reference point for further calculations.

4.3.4 Determination of activity distributions in test objects

Once the stock solution activity is determined, the ideal method is to use accurately weighed aliquots to define the activity and activity per unit mass of prepared test objects. This is not always practical in a clinical setting due to a lack of equipment. Therefore, the total activity can instead be tracked throughout the preparation process and the final activity concentration can be determined using knowledge of the test object volume as shown in Figure 4-3. The latter method is likely to provide an activity concentration with a higher uncertainty if the object volume is not well known. In pre-clinical studies, it is possible to measure directly the activity of some test objects using a radionuclide calibrator. Therefore, work can be done to calculate a dial setting that will allow rapid activity determination routinely.

4.4 Methodology

To determine if the Mediso pre-clinical system could accurately measure ^{89}Zr activity, it was first necessary to perform the manufacturer calibration in a traceable manner. Two experiments were done to perform these calibrations and are referred to herein as PC-C-1 and PC-C-2. Each experiment followed the Mediso recommended calibration protocols (Mediso, 2016), but included filling of the phantoms in a traceable manner as well as additional activity verification steps to ensure the calibration was successful. To determine measurement accuracy for ^{89}Zr and identify additional uncertainty components, a set of three syringes of known activity were measured on the pre-clinical scanner over a 6-week period. This was accompanied by the measurement of an image quality (IQ) phantom and long-lived QC check source containing ^{22}Na. A similar

measurement involving a single ^{18}F syringe was performed to give a comparison to the ^{89}Zr data.

4.4.1 Source Preparation

Both calibration experiments were based around the measurement of ^{18}F as FDG supplied by the PETIC cyclotron at Cardiff University. This cyclotron routinely produces GMP-grade ^{18}F-FDG and has rigorous QC procedures to ensure radionuclidic and chemical purity of the product. For each experiment, a 5 ml syringe was filled with a known activity of ^{18}FDG (Table 4-2) and sealed with a syringe cap to prevent leakage. In experiment PC-C-1, the activity was standardised with only the calibrated Captinec CRC-25/PET radionuclide calibrator, using a dial setting specifically determined for 5 ml of ^{18}F in a 5 ml syringe of the same type. In experiment PC-C-2, the activity concentration of the FDG solution was determined using weighed aliquots of a solution standardised using the UHW 'Fidelis' secondary standard radionuclide calibrator (which had previously been calibrated by NPL). The filled syringe was also measured directly on the Capintec CRC-25/PET calibrator, located in the preclinical scanner room, to confirm the activity and dial setting in use.

Experiment	Radionuclide	Activity (MBq)	Reference time
PC-C-1	^{18}F	12.28 (25)	2016-06-09 17:04:55
PC-C-2	^{18}F	4.943 (50)	2016-12-15 10:29:00

Table 4-2: Details of calibration syringes used for calibration of the Mediso nanoScan PET/CT system

For the verification measurements, a solution of ^{89}Zr as zirconium oxalate was provided by the PETIC cyclotron at Cardiff University. Aliquots of this solution were shipped to NPL to establish traceability for the radionuclide calibrators located at PETIC, as well as to determine impurity content. The syringes and QC source were filled by gravimetric means and the syringes were measured using the Capintec CRC-25/PET calibrator, which had been calibrated for ^{89}Zr against samples traceable to NPL. Aliquots were measured using the UHW Fidelis radionuclide calibrator to give additional confirmation

of the dial setting used for activity determination. The activities of each syringe and the QC source are listed in Table 4-3.

Object	Source Geometry	Activity (MBq)	Reference time
Syringe 1	5 ml active in 5 ml syringe	6.30 (13)	2019-02-27 14:54
Syringe 2	5 ml active in 5 ml syringe	1.030 (21)	2019-02-27 15:31
Syringe 3	5 ml active in 5 ml syringe	0.520 (10)	2019-02-27 15:27
QC Phantom	Image quality phantom	8.51 (17)	2019-02-27 16:07

Table 4-3: Activities of calibration objects

4.4.2 Equipment setup – calibration

The nanoScan PET/CT scanner was set up as described in the Mediso calibration protocol, with the filled syringe positioned centrally in the FOV. The syringe was mounted in a foam jig and secured with masking tape to ensure stability. X-ray scout images were taken vertically and laterally to ensure accurate positioning (Figure 4-4). The calibration protocol was loaded on the acquisition computer (Nucline) and relevant activities and reference times were inputted to the radionuclide information page. Measurements were not started until activities had decayed below 8 MBq in order to avoid adverse dead-time effects. The acquisition settings shown in Table 4-4 were used for the CT and PET calibration acquisitions with ^{18}F.

Modality	Parameter	Value
CT	Frames per rotation	480
	Number of rotations	2
	Slice Thickness	1 mm
	Reconstructed Pixel Size	0.250 x 0.250 mm
	Reconstructed Slice Thickness	0.250 mm
	Tube current	0.6 mA
	Tube Voltage	50 kVp
PET	Mode	Normal
	Slice thickness	0.4 mm
	Ring Difference	84
	Number of Slices	235
	Energy Window	400-600
	Coarse Coincidence Relation	1:5
	Fine Coincidence Relation	1:3
	Measurement time	600s

Table 4-4: Table of CT and PET aquisition parameters used for calibration measurements with ^{18}F

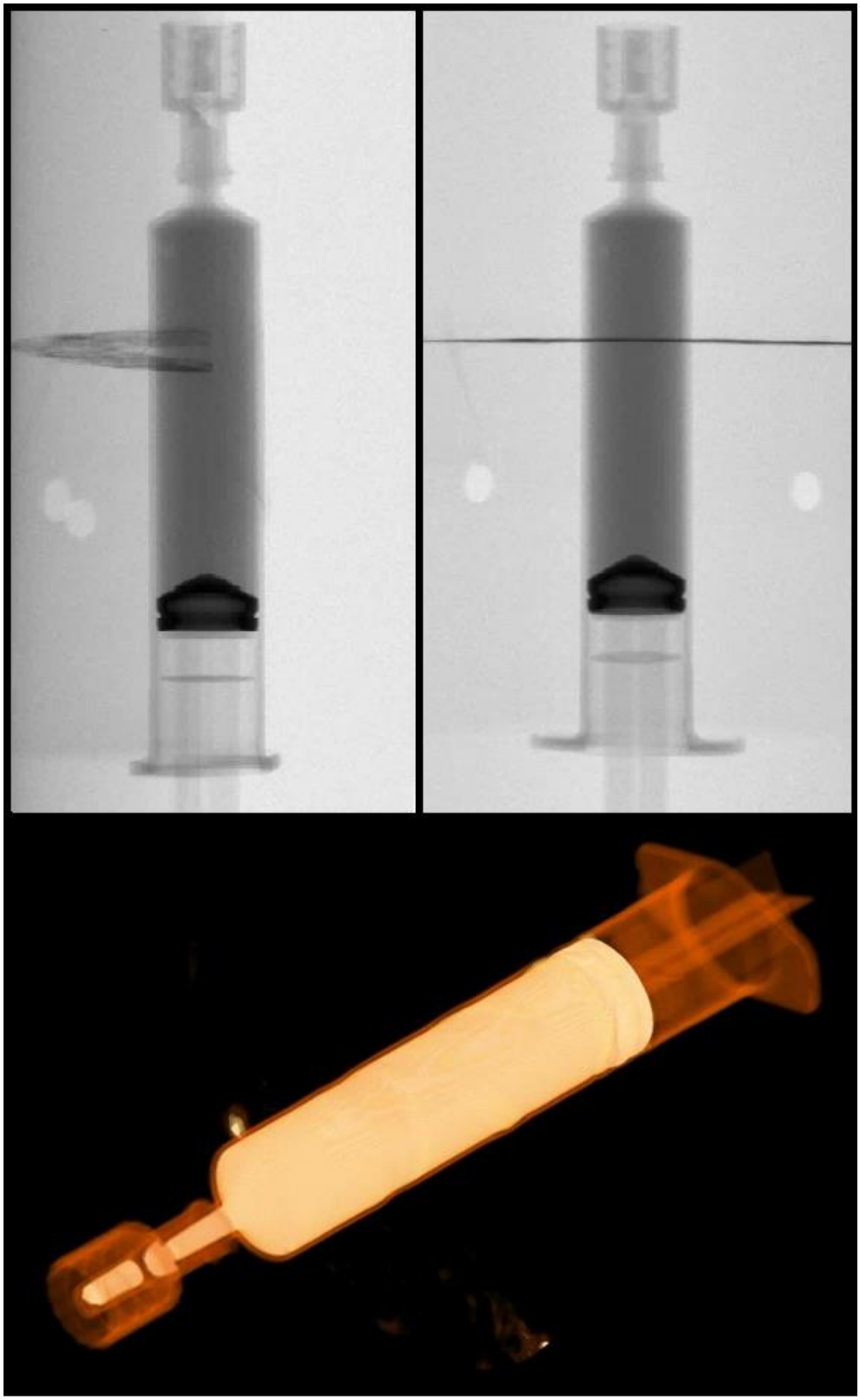

Figure 4-4: X-ray scout views (top) and CT 3D rendered image (bottom) showing typical syringe positioning within the scanner.

4.4.3 Equipment setup – Verification

For verification measurements, the three ^{89}Zr syringes were placed in a three-bed jig in a concentric ring such that they were equidistant from each other, and this ring was centred in the FOV. The QC source and IQ phantom were placed centrally in the FOV on a foam pad and secured with tape. The same PET and CT acquisition parameters were used, but the measurement time was increased to 60 minutes to account for the lower count rates that would be observed due to lower branching ratio and lower activity. The three syringes, QC source and IQ phantom were measured 6 times over a 23 day period (Table 4-5).

Measurement	Measurement Date	T-T0 (days)
1	27/02/2019 18:24	0.00
2	05/03/2019 17:15	5.95
3	08/03/2019 16:53	8.94
4	12/03/2019 10:27	12.67
5	18/03/2019 17:30	18.96
6	22/03/2019 09:36	22.63

Table 4-5: Measurement dates for ^{89}Zr verification measurements.

4.4.4 Activity measurements

For each experiment, a single PET/CT acquisition was performed for the sources as described above, and the images were processed using the manufacturer's protocol. In addition, further reconstructions were performed using the manufacturer's default settings as well as clinically used settings. This was done to determine the deviation of the calibration from a known activity value and its variation with different reconstruction methods. Manual volumes of interest (VOIs) were drawn on the images using the CT images as a guide, and recovered activities were decay corrected to common reference times using the half-life evaluated in Chapter 3 (78.361(39) hours). For the IQ phantom, a large region of interest (ROI) of diameter 20 mm was placed on a slice in the middle of the 'large volume' section. Furthermore, 5 individual ROIs of appropriate diameter (between 1 mm and 5 mm) were used to determine the recovery coefficients from the

rod portion of the phantom. QC measurements were performed using a solid ^{22}Na check source using a defined protocol which included a CT and PET image. Total counts in the QC source image were recorded, and no VOIs were drawn.

4.5 Results and discussion

4.5.1 QC measurements

The results from regular QC measurements are shown in Figure 4-5. The standard deviation of the residuals is 1.2%.

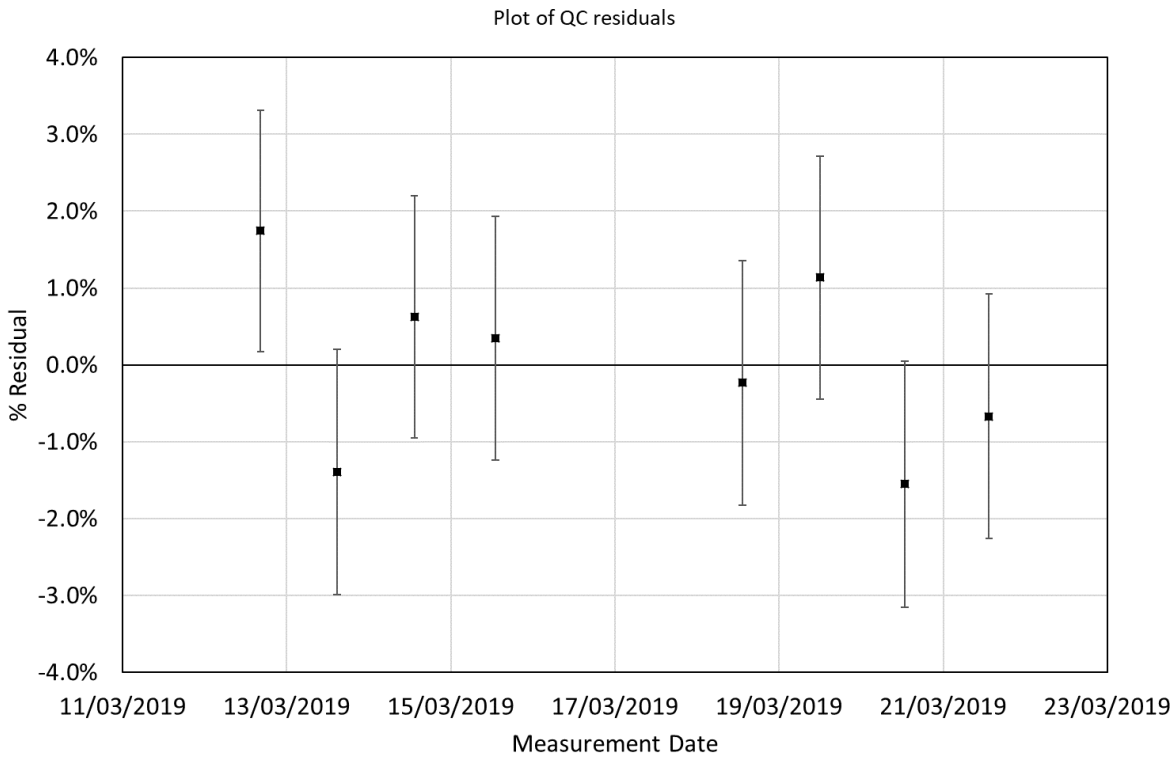

Figure 4-5: Plot of residuals from daily QC measurements covering the period between PC-C-1 and PC-C-2. Uncertainty bars are only statistical and calculated as the square root of the number of counts.

The plot includes uncertainties, which were determined using the square root of the number of counts. This is not mathematically correct since a degree of scaling and processing has been performed and, therefore, the total number of counts is not truly Poisson in nature. However, this gives a useful indication of whether the dataset is self-consistent. The measurements are in statistical agreement, which indicates the system is stable for the duration of the study. The variations are most likely caused by small

imperfections in the attenuation or scatter corrections applied, and the general drift of crystal sensitivity, which is to be expected from a crystal-based scintillating system. Since no VOIs are used, this provides a good overall indication of scanner performance and is less likely to be affected by human bias.

4.5.2 ^{18}F activity calibration

The activity calibrations were performed and the results from the subsequent verification checks are shown in Table 4-6. There is excellent agreement between recovered camera activity and the true ^{18}F activity when using the manufacturer recommended settings. Slightly greater variation becomes apparent when changing the number of subsets and iterations in the Teratomo reconstruction.

Experiment	Iterations	Subsets	Coincidence ratio	Image Activity (MBq)	Reference Activity (MBq)	Difference (%)
PC-C-1	4	6	1:3	12.42	12.28 (25)	0.10
	6	6	1:3	12.12	12.28 (25)	0.67
	4	3	1:3	12.41	12.28 (25)	0.23
	6	3	1:3	12.12	12.28 (25)	0.75
PC-C-2	2	6	1:3	4.96	4.941 (50)	-0.50
	2	6	1:3	4.96	4.941 (50)	-0.50
	4	6	1:3	4.93	4.941 (50)	0.10
	4*	6*	1:3	4.94	4.941 (50)	0.08
	6	2	1:3	4.93	4.941 (50)	0.25
	6	6	1:3	4.95	4.941 (50)	-0.20

*Table 4-6: Results from ^{18}F calibration verification measurments. Rows highlighted in green have been reconstructed using Mediso recommended clincial reconstruction settings. The * indicates that a new VOI was drawn to observe repeatability of the VOI placement process.*

To provide a true comparison between settings, the same CT-defined VOI was applied to each image within each experiment, allowing direct comparison without the confounding effect of inaccurate VOI drawing. The exception to this approach was the repeat drawing of a VOI in experiment PC-C-2 to limit the effect of user variability. Since the results are ultimately reliant on a human-drawn VOI, this is a limitation of this verification. The drawing of VOIs is a limitation of all imaging processes and much debate

can be found in literature relating to these issues (Ahlawat et al., 2016; Lambregts et al., 2011; Nogueira et al., 2015; Rusjan et al., 2006; Schaefer et al., 2016).

4.5.3 Verification of ^{89}Zr activity

Results from the verification measurements indicate that there is a positive bias to the recovered activity values for this scanner as compared to ^{18}F (Figure 4-6). The VOIs were drawn in the same way (using the CT images as a guide). They were drawn on the first image; the same VOIs were applied to all subsequent images and visually checked to ensure alignment. This was possible as the syringes were left on the bed and not removed during the campaign. Therefore, although individual scans were taken, the geometry remained very consistent. Across the campaign, the results show a slightly larger average difference for syringe 2 compared to syringe 1, which could be attributed to a problem during the filling or measurement of this syringe, such as an image artefact or VOI positioning error.

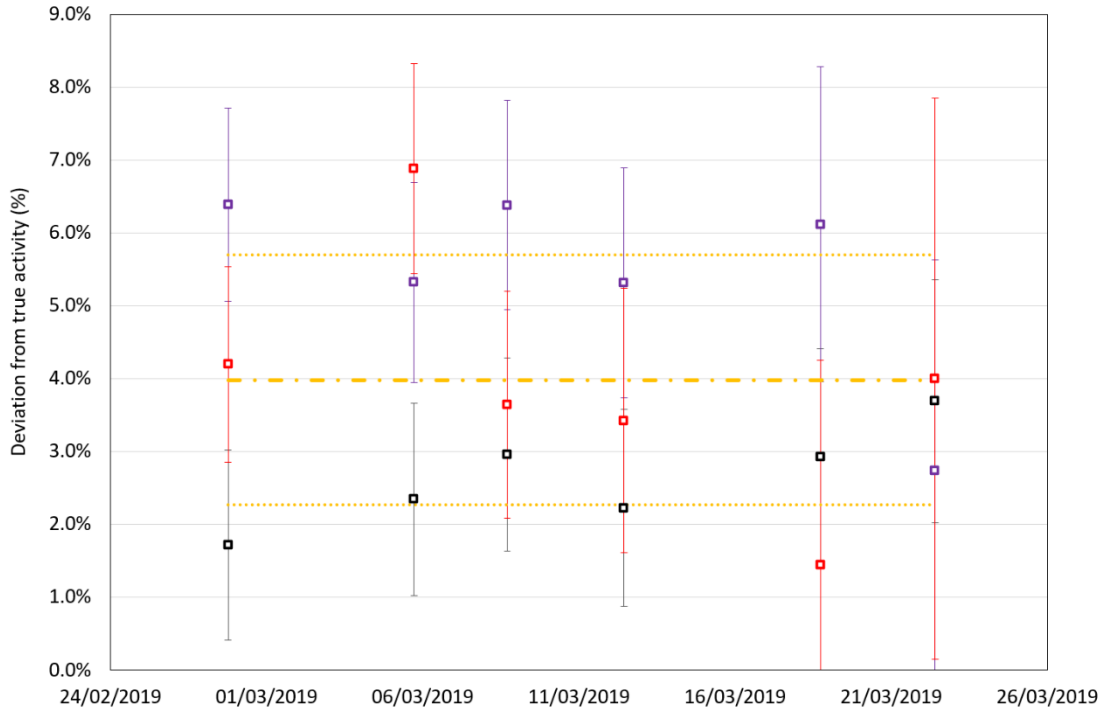

Figure 4-6: ^{89}Zr accuracy measurements presented by measurement date. The three syringes are denoted by the different colours series with the black squares representing the high activity syring, the purple representing the medium activity syringe and the red points the low activity syringe. The yellow lines show the mean and standard deviation of the combined data.

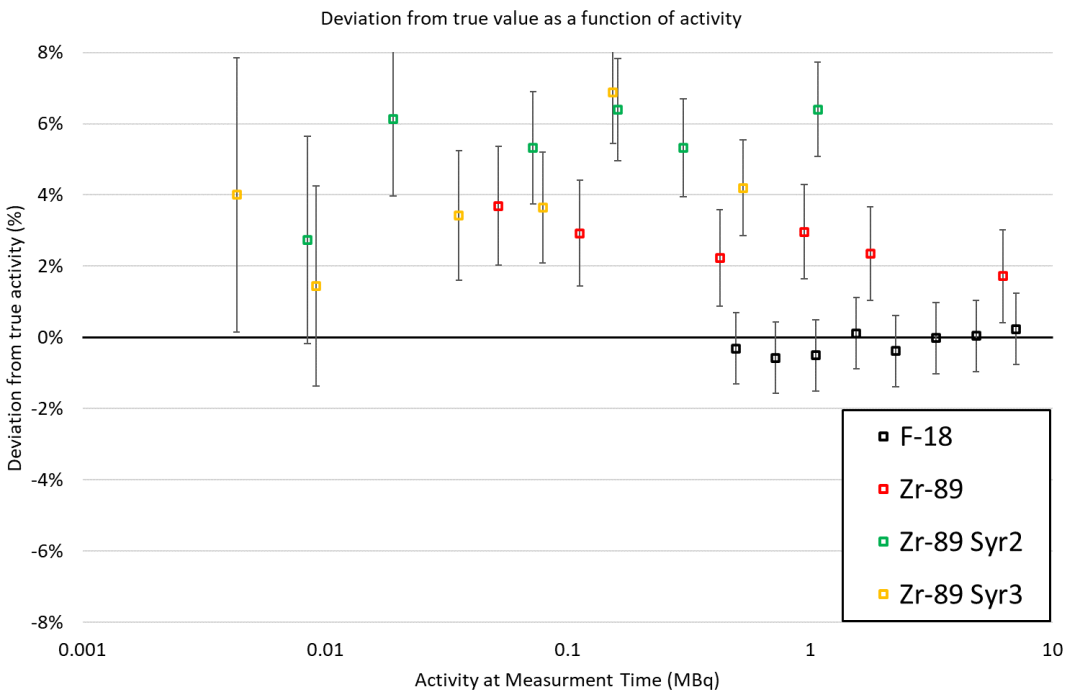

Figure 4-7: Activity recovery accuracy for ^{89}Zr in three syringes, plotted against activity at the measurement time. A similar dataset for a single ^{18}F syringe is shown for comparison.

Figure 4-7 shows accuracy as a function of activity at time of acquisition, plotted alongside the same results for ^{18}F. The ^{18}F data show far less variance; this is most likely due to the method of acquisition, which was done over a shorter time frame and only used a single CT scan with the source remaining static in the counter between measurements. The accuracy is consistent with the verification measurement presented earlier. The ^{89}Zr data indicate that there is no change in the accuracy for ^{89}Zr when imaging at lower activities. The reason for the bias in the ^{89}Zr data is, therefore, unclear and could be attributed to several components. The most likely components are a problem in the translation of the ^{18}F calibration to ^{89}Zr (via a branching ratio correction) and incorrect correction applied for additional random gamma events due to downscatter from the 909 keV gamma in ^{89}Zr. An experiment to investigate the latter effect is discussed in future work (section 6.5.5). The uncertainties are again taken from the square root of the number of counts within the VOI, combined in quadrature with the activity uncertainty to give an indication of whether the dataset is consistent.

4.5.4 Image quality phantom results

Only four of the six measurements made on the IQ phantom were used to determine recovery coefficients (RCs) for ^{89}Zr. This was due to issues with the application of attenuation correction on two images due to a problem with the CT acquisition. The aim was to determine if performance is comparable to other published data and whether there was an activity dependence on recovery coefficients.

The results (Figure 4-8) show that there is a slight reduction in the RC for the smallest rod as activity decreases. However, there are no statistically significant differences between the other rods. The RC values converge to a value of 1 for the two greatest rod sizes, with convergence at a maximum between the 3 mm and 4 mm rods. Work by Bradshaw et al. (2016) on a Siemens pre-clinical camera with the same radionuclide reported similar findings and, therefore, this is a good independent comparison to make. The RCs in this work are slightly higher and converge more quickly than values published by Gaitanis et al. (2017) for both ^{18}F and ^{68}Ge on a similar Mediso system. No explanation is given for the low values observed in the other work, however, advances in the reconstruction process could be a significant contributor to these differences.

The results show that the system is representative of a typical clinical imaging system and, when combined with the quantification accuracy they indicate that traceable activity measurements with ^{18}F and ^{89}Zr are possible provided the associated uncertainty budgets can be established.

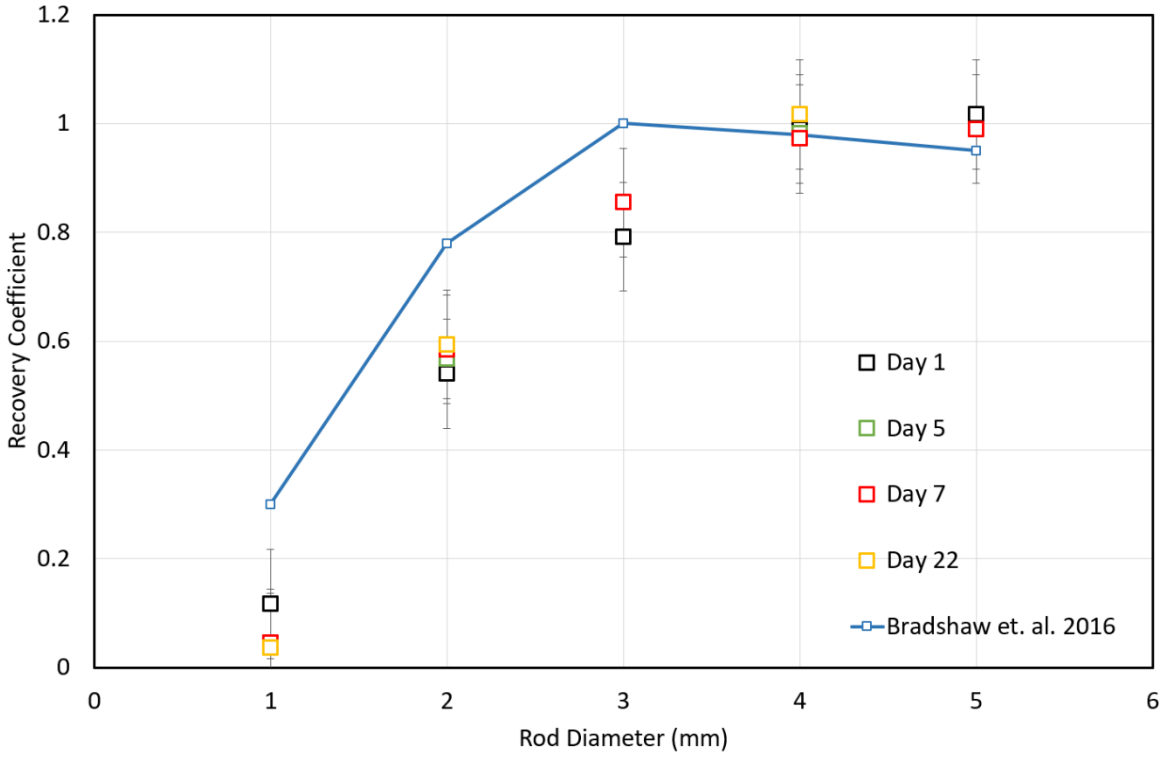

Figure 4-8: Recovery coefficients from Image Quality phantom measurements on days 1, 5, 7 and 22 plotted alongside values taken form a similar measurement by (Bradshaw et al., 2016).

4.7 Chapter summary

The quantification of activity in pre-clinical scanner images has been found to be relatively accurate for ^{18}F and ^{89}Zr, when missing uncertainty components are considered. This highlights that significant work should still be done to calibrate and validate a system prior to use. The accuracy was best for ^{18}F (<1 %), which is to be expected since this radionuclide is also used for calibration. When using ^{89}Zr, the system measured activity was, on average, 4 % higher than the true activity. This could be due to imperfect scatter or random correction since the system has been tuned specifically for ^{18}F. To better establish the cause of this bias, further work is required to define the uncertainty components.

The manufacturer's methods for calibration must be employed in conjunction with accurately calibrated activity measurement equipment, accurate half-life data and traceable methods of filling phantoms and test objects as described. The daily QC measurements may be used to quantify long-term stability of a scanner system and provide valuable uncertainty components. The type of reconstruction used is important when performing validation measurements and, therefore, these should be tested for accuracy before use. Image quality is not discussed in detail but, from the literature, it is clear that ^{89}Zr would benefit from an in-depth analysis of imaging characteristics using a traceably calibrated solution.

Chapter 5: Clinical PET imaging of ^{89}Zr

5.1 Introduction

Once pre-clinical studies have concluded and a radiopharmaceutical moves into the clinical testing realm (phase 3+ trials), the need for traceability follows. This chapter presents results from the activity calibration and verification of a clinical imaging system located in a research environment using typical clinical protocols, along with verification measurements performed on a clinical system located at PETIC. Clinical imaging systems must be calibrated using the manufacturer's protocols to ensure compliance with medical device legislation (The Medical Devices Regulations 2002), and this is typically performed using ^{18}F as a reference radionuclide. The translation of a calibration using a single radionuclide to other radionuclides means that traceability is more difficult to prove, and can leave the measurement open to errors caused by the use of incorrect nuclear data. The methods for translating a calibration with one radionuclide to another are rarely disclosed by manufacturers, which makes establishing traceability difficult. One potential solution to this problem is to perform measurements using a traceable solution of the radionuclide of interest to verify the accuracy of the translation, but there must also be a realistic assessment of the uncertainty components even if a device is to be deemed traceable. Ideally, devices would be calibrated independently for each radionuclide to reduce the chance of errors occurring, but this is not always practical in a clinical setting and some compromises must be made.

This chapter aims to:

- Calibrate a clinical PET camera using traceable solutions, following the manufacturer's protocol.
- Perform verification measurements to determine the activity accuracy when measuring traceable solutions of ^{89}Zr on systems at NPL and PETIC.

- Identify basic uncertainty components that could easily be measured in a clinical environment.
- Present a shortlist of requirements that are needed to verify a clinical system for the quantification of ^{89}Zr activity.

5.2 Equipment

5.2.1 Phantoms

5.2.1.1 Cylindrical phantom

For calibration and verification measurements at NPL, a cylindrical phantom with a diameter of 200 mm and fillable length of 170 mm constructed from PMMA was employed. This phantom was supplied by Mediso for use during calibration measurements and has a volume of approximately 4.5 l.

5.2.1.2 NEMA image quality phantom

For verification measurements at NPL and PETIC, the standard national electrical manufacturers association (NEMA) IQ phantom was employed. The NEMA IQ phantom contains six spheres ranging in size from 10mm to 37 mm diameter and has a removeable insert filled with water and polystyrene to mimic lung material (Figure 5-4). It also has a removeable stepped compartment containing di-potassium hydrogen orthophosphate (K_2HPO_4) which has a similar density to bone.

5.2.2 Mediso Anyscan Trio PET-CT

Figure 5-1: Mediso AnyScan Trio SPECT/CT/PET scanner at NPL

In 2017, NPL invested in a Mediso Anyscan-Trio SPECT/CT/PET system (Figure 5-1) to be used for SPECT and PET metrology. The purpose of obtaining this camera was to develop methodologies for improving the traceability of imaging measurements performed in clinical sites. The device is a full clinical system with PET time of flight capability and has all the clinical protocols required for scanning patients. The additional benefit of a close working relationship with the manufacturer provides details of commercially sensitive components that enable a more thorough assessment of uncertainty and accuracy. As a metrology organisation, NPL pays great attention to defining the traceability of all measurements, and this is difficult to achieve using a 'black-box' commercial system such as the Mediso clinical scanner. Therefore, independent reconstruction platforms (such as STIR (Thielemans et al., 2012a)) have been employed to process data acquired on the system and perform uncertainty assessment and propagation. Since this thesis is focussed on clinical implementation, only the clinical system and manufacturer supplied software have been used as this is all that is typically

available to a clinical site. This significantly limits the assessment of uncertainties in an efficient way, and these caveats are discussed in Chapter 6.

5.2.2.1 General overview of hardware

Figure 5-2 depicts the general hardware layout of the Mediso Anyscan Trio PET system at NPL. The detector is constructed of 24 modules, each consisting of 1026 cerium doped lutetium yttrium orthosilicate ($Ce_{2x}(Lu_{1-y}Y_y)_{2(1-x)}$) (Chai and Ji, 2003) crystals connected to an array of 12 photomultiplier tubes (PMTs). Each module has a dedicated analogue to digital converter (ADC), and 4 modules share a single DCS card which applies corrections to the recorded data. Events may be accepted or rejected based on energy and timing (coincidence window). Appropriate filtering for other effects, such as pileup rejection, are applied to accepted data at this point. Appropriate corrections for other effects, such as dead-time, are applied to accepted data at this point. The criteria for decision making are determined in factory testing and interim servicing. The FPGA and ADC cards are housed on a so-called digital acquisition card ('DCS') which, in turn, is connected to all other DCS cards in the system via high-speed cables. The DCS cards also facilitate communication with a real-time acquisition and processing PC ('Teratomo Real'), a post reconstruction PC ('Teratomo Post'). A graphical user interface (GUI) is hosted on a control PC ('Nucline'), which controls communication between the different computers. Within the system, there are many components which will contribute an uncertainty to each measurement. However, it is impractical for a clinical site to assess many of these. A more detailed discussion of these components is presented in Chapter 6.

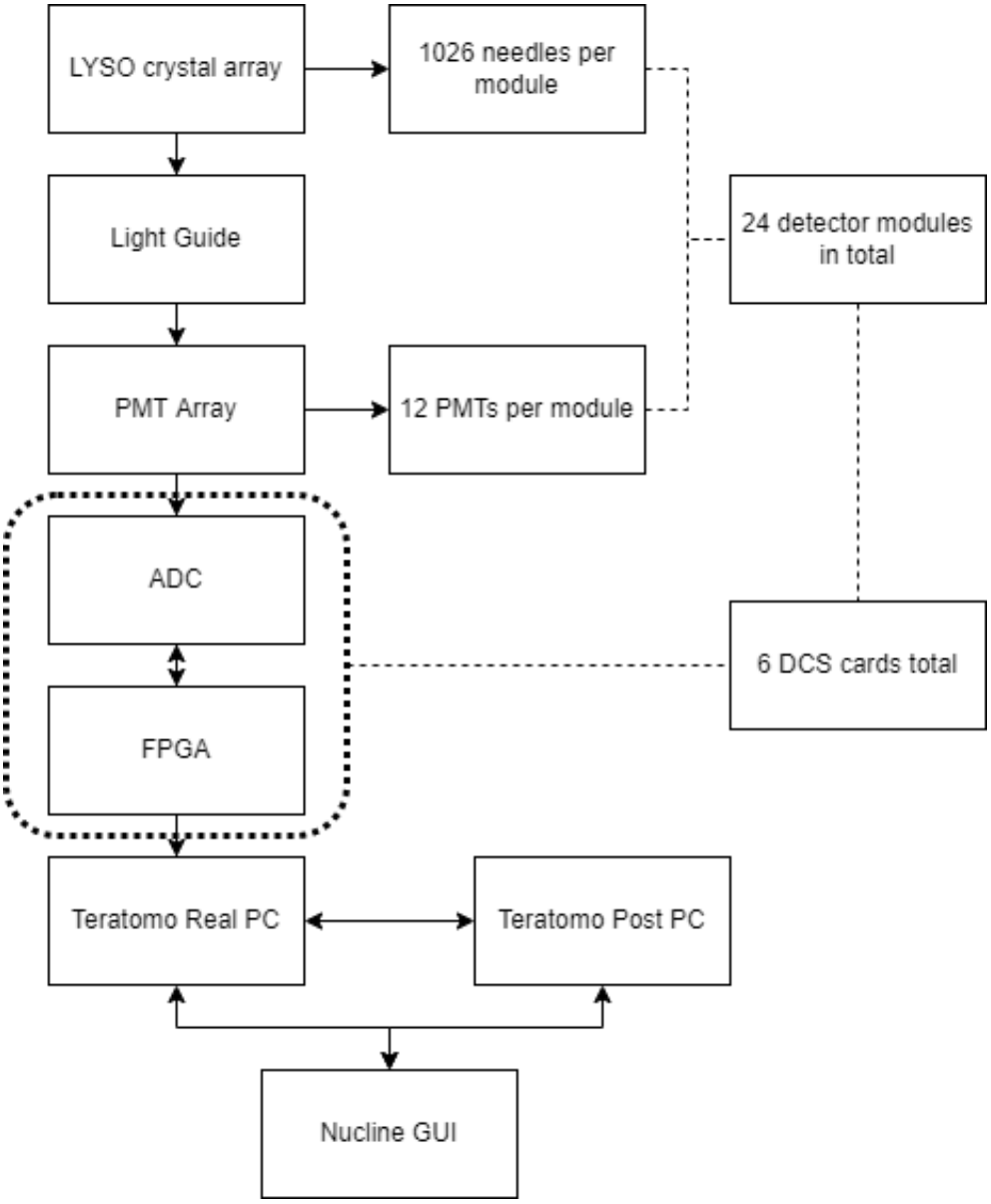

Figure 5-2: Overview of hardware relationships within the Mediso Anyscan PET-CT system. The boxed group are all contained on a single 'DCS' card and the dotted lines show the relationships within the hardware.

5.2.2.2 Data processing steps

When an event is recorded in a detector module, the first processing step is the accept/reject decision made by the leading edge (LE) discriminator of the ADC card. Once an event is accepted, pileup filtering is performed, time-stamp and energy information is given, and the event is recorded in a data package. These data packages are compared with other data packages from the other DCS s and a coarse coincidence

filtering is performed. These data are then sent to the Teratomo Real PC for further processing. On the Teratomo Real PC, the data packages are processed to determine position information, energy and time for each event, and this information can be outputted as list mode data. The Teratomo Real PC initially applies corrections and filtering for time, energy and position, coincidence mode using a series of lookup tables, ready for the next processing step. The binned data are then sent for reconstruction on the Teratomo Real or Teratomo Post reconstruction PCs with user defined reconstruction parameters.

5.2.2.3 Overview of manufacturer calibration protocol

All device manufacturers recommend and supply a protocol for creating and maintaining the calibration of the system. Some processes are typically performed by the manufacturer prior to installation or during routine servicing, and other processes must be performed on-site by the local physicists. Figure 5-3 details the extended procedure required for the calibration of the Mediso Anyscan Trio PET-CT camera.

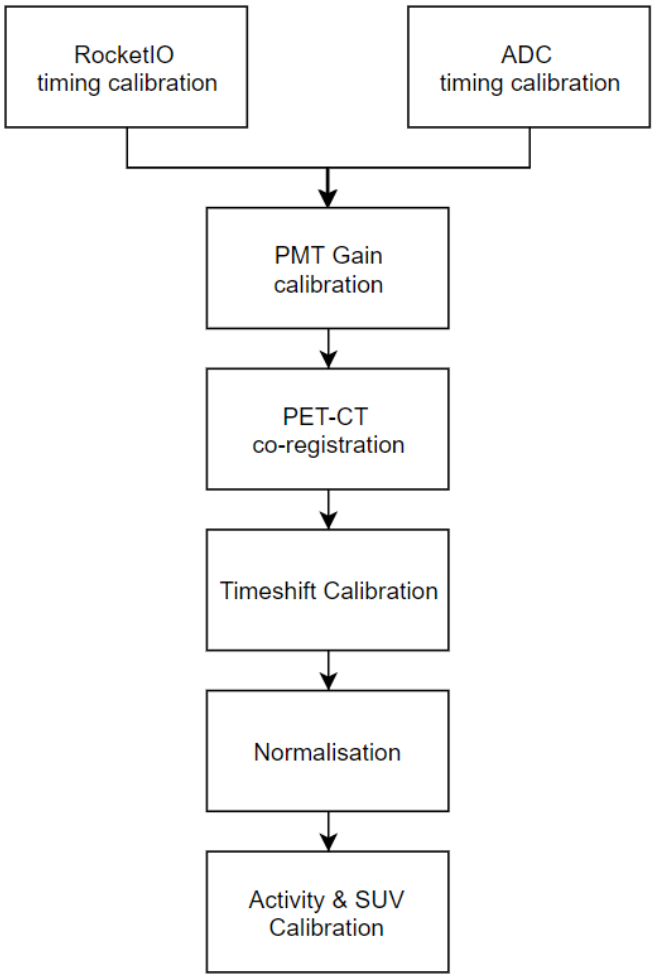

Figure 5-3: Manufacturer supplied calibration protocol for the Mediso Anyscan Trio PET-CT system. 'RocketIO' refers to the internal cabling system between the ADC boards.

5.2.2.4 'Rocket IO' calibration

The 'Rocket IO' calibration is performed in order to calculate the inherent delay in the communication between the different ADC modules within the detector ring through the 'RocketIO' cables. This is important to ensure that timing between the ADC modules is consistent and so that events can be binned correctly. A drift in the time delay imposed by the cabling would effectively lead to reduced efficiency as coincident events would be 'lost'. This could lead to incorrect coincidences being recorded, thus causing artefacts in the image. In reality, the timing calibration of the Rocket IO is unlikely to change significantly between service intervals without failure of hardware. The RocketIO system

calibration is performed automatically by sending test signals through it and calculating a table of correction factors.

5.2.2.5 ADC calibration

The ADC calibration determines corrections for the timing of the ADC cards to ensure proper timing. As with the Rocket IO, this calibration is unlikely to drift during routine use. Drift would lead to either lowered efficiency or incorrect coincidence filtering. The ADC calibration is performed automatically by the controlling PC by sending test signals through the ADC cards and calculating a table of correction factors to each one.

5.2.2.6 PMT gain calibration

The PMT arrays in each module must be tuned such that the output of the array is normalised to the same channel number (proportional to the energy) as the other PMT arrays in the PET ring. This is to ensure that the events within the selected window are normalised across the whole detector and are comparable. A drift in the PMT gain will cause a loss of counts as the primary photopeak drifts out of the selected energy window and, therefore, this is a critical calibration to maintain measurement accuracy. The gain calibration is performed using a customised acquisition protocol with a point source of any positron emitter, which is placed in the centre of the field of view. The emitter must have a ‘clean’ 511 keV energy peak (i.e. no other emissions between 300 and 700 keV).

5.2.2.7 PET-CT co-registration

Modality registration is critical to ensure accurate alignment of PET and CT images for attenuation correction, and for anatomical registration in clinical applications. Mis-registration of the two modalities can lead to image artefacts in reconstructed PET images, as well as severely affecting the accuracy of the activity distribution measurement. The modality registration should be confirmed regularly to ensure continued accuracy of the reported PET activity values.

The modality registration is performed by the measurement of a specialised phantom containing aluminium cups that can be filled with a positron emitter (typically ^{18}F). The phantom is scanned by CT followed by a PET acquisition, and automated software aligns the two modalities. The images can then be visually inspected in an viewer to confirm registration. If additional adjustments are required to improve registration, it is possible to manually edit the x, y and z offset values in the system calibration folder. This ability to edit values manually may be useful when assessing the contribution of mis-registration to overall uncertainty.

5.2.2.8 Time shift calibration

The time shift calibration calculates the detector timing characteristics of the crystal needle array. Since the RocketIO and ADC timing have already been determined, any residual coincidence delay must be due to differences in the timing of the detector crystals. It is determined by placing a large cylindrical phantom containing a clean positron emitter in the centre of the PET field of view and running an acquisition. A table of time delays is calculated and recorded in the system calibration file. The crystal delay is not likely to drift during usual operation; however, it is standard practice to perform a test during routine calibration operations.

5.2.2.9 Normalisation calibration

Normalisation calibration determines crystal sensitivity and creates a table of correction factors to normalise all crystals, and thus output homogeneous images. This is critical to ensure PET image quality and activity accuracy. To calculate the correction tables, a cylindrical phantom filled with a homogeneous solution of a clean positron emitter is placed in the centre of the field of view and data acquired to obtain more than 10,000 counts in each crystal (prior to normalisation). The normalisation test is performed regularly, and a certain amount of drift in the normalisation values is to be expected due to changes in environmental conditions or degradation of the crystals themselves.

5.2.2.10 Activity calibration

The final calibration is to determine a factor for the camera which will convert raw counts into activity (known as the activity factor). This is performed with ^{18}F and the activity factors for other radionuclides are determined using nuclear data rather than by direct calibration. The activity calibration is the most critical in terms of activity accuracy, as any error here will directly propagate to any future measurements. The activity accuracy is checked during daily QC to ensure consistency and is recalibrated as required.

To determine the activity factor, a cylindrical phantom homogenously filled with a traceable solution of ^{18}F is placed in the centre of the field of view. CT and PET scans of the phantom are performed, and images are reconstructed using several different reconstruction parameters to establish activity factors for the different reconstruction modes. The camera automatically determines count rate and determines a conversion (typically in cps/Bq) based on the activity inputted to the software. Therefore the accuracy of the injected activity directly affects the final activity factor. This phantom must be prepared in an accurate manner to ensure an accurate activity factor is determined.

5.2.2.11 Image quality phantom (NEMA)

The final measurement is a test rather than a calibration, but it provides good confirmation that the previous steps have all been performed successfully. The standard national electrical manufacturers association (NEMA) image quality phantom is ¼ filled with water before adding a standardised solution of ^{18}F with an activity of approximately 150 MBq. This is then mixed and drawn into a syringe to fill the 4 smallest spheres, and the residue is returned to the background cavity. The two remaining spheres are filled with inactive water and the background cavity is topped up with water, taking care to remove as many air bubbles as possible. This phantom can then be used to verify the activity accuracy, recovery coefficient curves (for partial volume effect), homogeneity and spill in/out values for water and lung material.

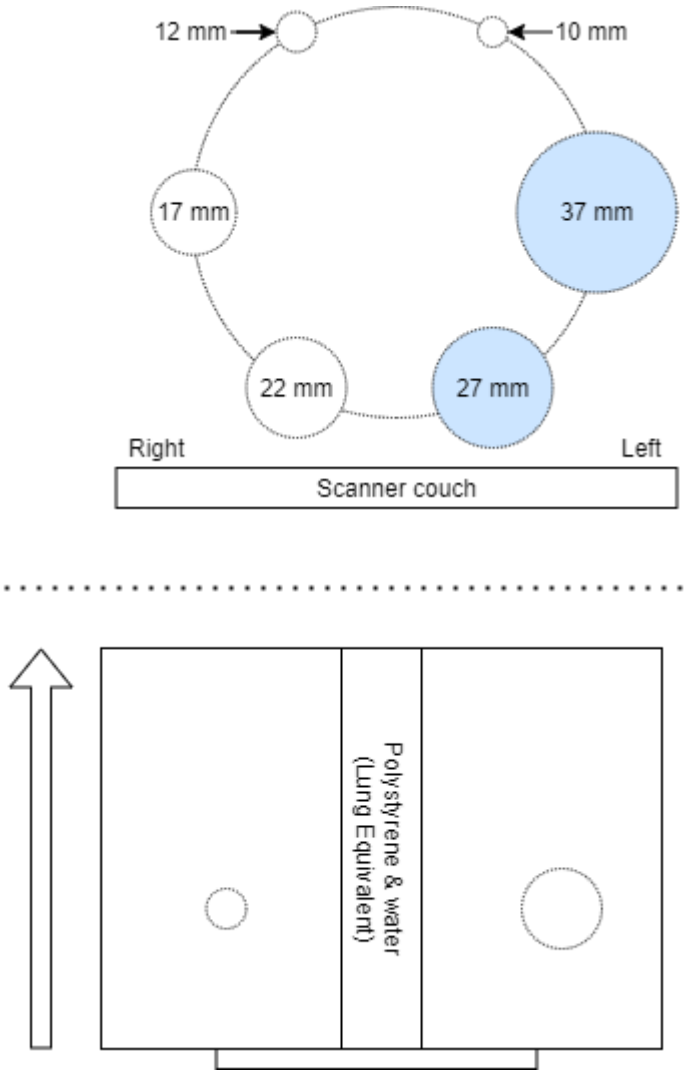

Figure 5-4: Nema Phantom setup for ^{18}F calibration measurments. The blue spheres (two largest) are filled with inactive water solution.

5.2.4 GE Discovery 690 PET/CT

In 2010 the Wales Research and Diagnostic PET Imaging Centre (PETIC) began scanning patients on a newly installed GE Discovery 690 PET/CT scanner. The device is a full clinical system with ToF capability. Unfortunately, there is no agreement with the manufacturer to share details of the internal workings of this device which will ultimately limit the ability create a complete uncertainty estimation in future. Much like the Mediso scanner described in section 5.4.1, the scanner consists of segmented LYSO crystals optically coupled to PMT arrays creating the equivalent of 13,824 individual crystals. The GE system is advertised as having a crystal size of 4.7 x 6.3 x 25 mm compared to the Mediso crystal size of 3.9 x 3.9 x 20 mm and an axial FOV of 157 mm compared to the Mediso system with 152 mm. The GE scanner has a larger imaging aperture than the mediso system (700 mm compared to 500 mm), but generally the two systems are comparable. As with the Mediso system, the data on the GE system is digitised and processed by the series of modules, which apply corrections for timing, dead time and amplitude. The modules create data packets which are converted to list-mode format to be reconstructed on a reconstruction computer. As PET is a relatively mature science area, it is likely that the steps described above for data handling within the Mediso system are very similar to the data handling steps within the GE system.

The typical reconstruction algorithm used for clinical work is a 3D OSEM-based reconstruction algorithm supplied by GE which includes ToF correction.

5.4 Measurements and methods

5.4.1 Mediso Anyscan Trio PET/CT

The first step in establishing a traceable calibration was to perform the manufacturer calibrations using traceable solutions. These were only performed on the NPL system due to limited access to the PETIC scanner. The Rocket IO, and ADC calibrations do not require any radioactivity and were performed according to the manufacturer guidance. For the gain calibration, a 1mm point source containing approximately 37 MBq ^{68}Ge (reference time 2019-06-01 18:00 UTC) was used instead of the manufacturer recommended 0.5 ml in a 2.5 ml syringe, as this is more convenient for the user. The PET/CT co-registration was then performed using a non-standardised high activity ^{18}F solution and the dedicated alignment phantom. For normalisation and activity calibration, a stock solution of ^{18}F was prepared and aliquots were measured directly on the NPL secondary standard ionisation chamber systems. The time-shift, normalisation and activity calibrations were performed using a traceable solution of ^{18}F. This was prepared as described in section 4.3 i.e. making a standardised stock solution which was then used to prepare calibration artefacts. The validation measurements using ^{89}Zr at NPL were performed using both a cylindrical phantom (to replicate the calibration geometry) and a NEMA image quality phantom to determine recovery coefficients (RCs) for partial volume effect (PVE). A series of measurements were performed over 21 days on these phantoms with both time of flight (ToF) enabled and disabled.

5.4.2 GE Discovery 690 PET/CT

Whilst the calibration measurements were not performed as part of this thesis, they were carried out by PETIC staff with access to a traceably calibrated radionuclide calibrator and followed the manufacturer's protocol. The verification measurements on the PETIC scanner were performed using a standard NEMA image quality (IQ) phantom with 6 spheres, lung insert and the bone equivalent cavity installed. The spheres were initially filled with active solution and a PET/CT image performed with a water-filled (inactive)

background. Subsequently, the background was filled with an active solution and further imaging was performed. This allowed the determination of recovery coefficients calculated with and without background spill in/out. All images on the PETIC scanner were performed with ToF enabled.

5.4.3 Source preparation

Source preparation for the calibration measurement at NPL was carried out using ^{18}F supplied as GMP-grade fluorodeoxyglucose ($C_6H_{11}{}^{18}FO_5$) by Alliance Medical. Samples were diluted using deionised water unless otherwise stated, and gravimetric dispensing steps were performed to determine the mass of solution in each artefact prepared. Verification measurements at NPL used ^{89}Zr supplied by Perkin Elmer as zirconium oxalate ($C_4O_8{}^{89}Zr$) which was then diluted using 1 mg g^{-1} diethylenetriamine pentaacetate (DTPA - $C_{14}H_{23}N_3O_{10}$) to act as a stable buffer solution. Verification measurements at PETIC used ^{89}Zr supplied by the PETIC cyclotron as zirconium oxalate, which was then diluted using 0.1 mol dm^{-3} hydrochloric acid containing 10 µg g^{-1} inactive zirconium carrier. This has the effect of converting the zirconium from oxalate to chloride ($^{89}ZrCl_4$) and maintaining a stable solution.

5.4.3.1 NPL ^{18}F calibration measurements

In August 2020, a solution of ^{18}F with a nominal activity of 1 GBq was delivered to NPL. The solution was diluted to create a stock solution and aliquots were measured on the NPL secondary standard ionisation chamber to provide an accurate activity concentration. This solution was then dispensed to a cylindrical phantom and NEMA image quality phantom; the activities and reference times are listed in Table 5-1.

Source ID	Source type	Activity (MBq)	Reference time (UTC)
P200027	Cylindrical phantom	45.51 (31)	2020-08-28 13:00
P200028	NEMA IQ phantom	51.88 (35)	2020-08-28 16:30

Table 5-1: Calibration phantom activities

5.4.3.2 NPL ^{89}Zr verification measurements

In December 2020, a solution of ^{89}Zr oxalate with a nominal activity of 220 MBq was delivered to NPL. The solution was diluted with a 1 mg g^{-1} solution of DTPA to a total weight of approximately 15g. This was gravimetrically dispensed to the calibration sources, the cylindrical phantom, and a dilution bottle for filling the spheres within the NEMA IQ phantom, which were set up in the configuration shown in Figure 5-6. All activities were determined using the NPL secondary standard ionisation chamber system, and the dilution was determined gravimetrically and verified using gamma spectrometry measurements. Since it was expected that the recovery coefficients for ^{89}Zr would be worse than those for ^{18}F, it was decided to fill all the spheres with activity to determine if the largest sphere would reach a recovery coefficient of 1. Aliquots of the solution were also analysed by gamma spectrometry to confirm activity values and to determine sample radionuclide purity. The activities of the verification phantoms are shown in Table 5-2 and a flowchart showing the preparation steps is given in Figure 5-5.

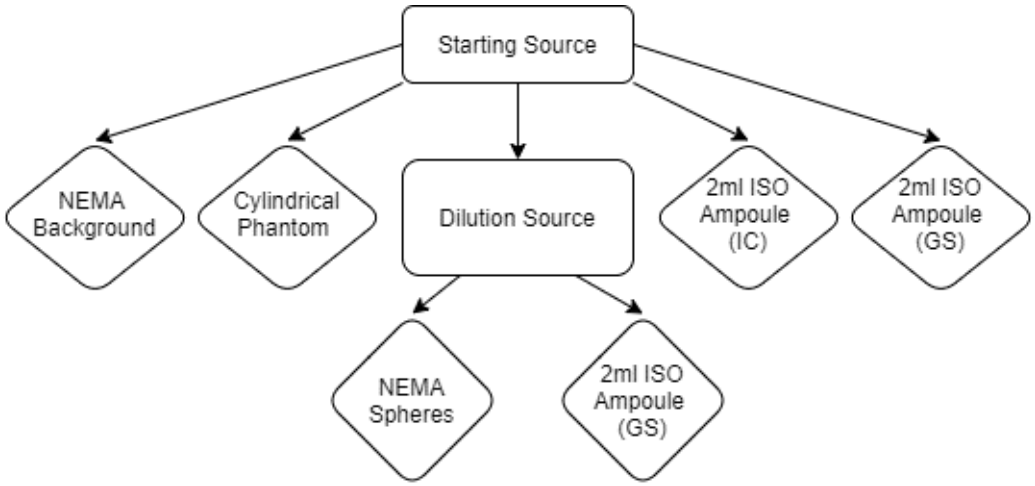

Figure 5-5: Flowchart showing the source preparation steps for the ^{89}Zr verification sources.

Source ID	Source type	Activity (MBq)	Reference time (UTC)
P200037	Cylindrical phantom	49.98 (37)	2020-12-15 12:00
P200028	NEMA IQ phantom (Background)	128.67 (96)	2020-12-15 12:00
P200028	NEMA IQ phantom (0.6 ml Sphere)	0.05763 (44)	2020-12-15 12:00
P200028	NEMA IQ phantom (1.2 ml Sphere)	0.11695 (90)	2020-12-15 12:00
P200028	NEMA IQ phantom (2.6 ml Sphere)	0.2605 (20)	2020-12-15 12:00
P200028	NEMA IQ phantom (5.6 ml Sphere)	0.5651 (44)	2020-12-15 12:00
P200028	NEMA IQ phantom (12 ml Sphere)	1.1624 (89)	2020-12-15 12:00
P200028	NEMA IQ phantom (27 ml Sphere)	2.671 (21)	2020-12-15 12:00

Table 5-2: Activities for the ^{89}Zr verification phantoms determined by ionisation chamber measurement.

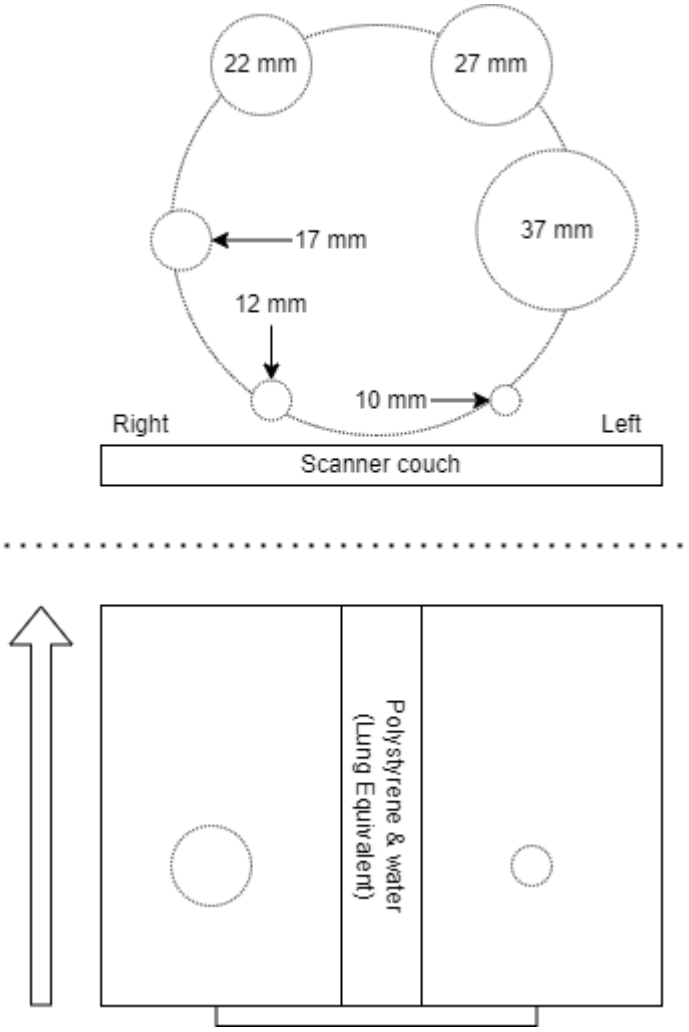

Figure 5-6: Setup of NEMA phantom used for the Mediso ^{89}Zr measurements performed at NPL. The arrow indicates direction into the scanner

5.4.3.3 PETIC ^{89}Zr verification measurements

In June 2016, approximately 200 MBq of ^{89}Zr oxalate was acquired from the PETIC cyclotron facility. An aliquot of this solution was diluted to create 50 ml of solution at 304.1 (30) kBq g^{-1}, which was standardised by measurement of a 4 ml aliquot in a 10 ml Schott vial on the UHW 'Fidelis' secondary standard calibrator. This solution was used to fill the 6 spheres of the NEMA phantom which was set up as shown in Figure 5-7. The background cavity (containing the lung insert, and a special section containing bone equivalent material) was then filled with water prior to the first imaging. Subsequently, the background cavity was emptied and ¾ filled with 0.1M HCl containing 10 µg g^{-1} Zr^{-},

before the addition of 131.1 (13) MBq of active solution. The contents of the cavity were mixed, and then it was completely filled with the same carrier leaving no significant air bubbles. A 2 ml aliquot of this solution was removed from the cavity and sent to NPL for measurement by gamma spectrometry to determine the background activity concentration and to determine sample radionuclide purity.

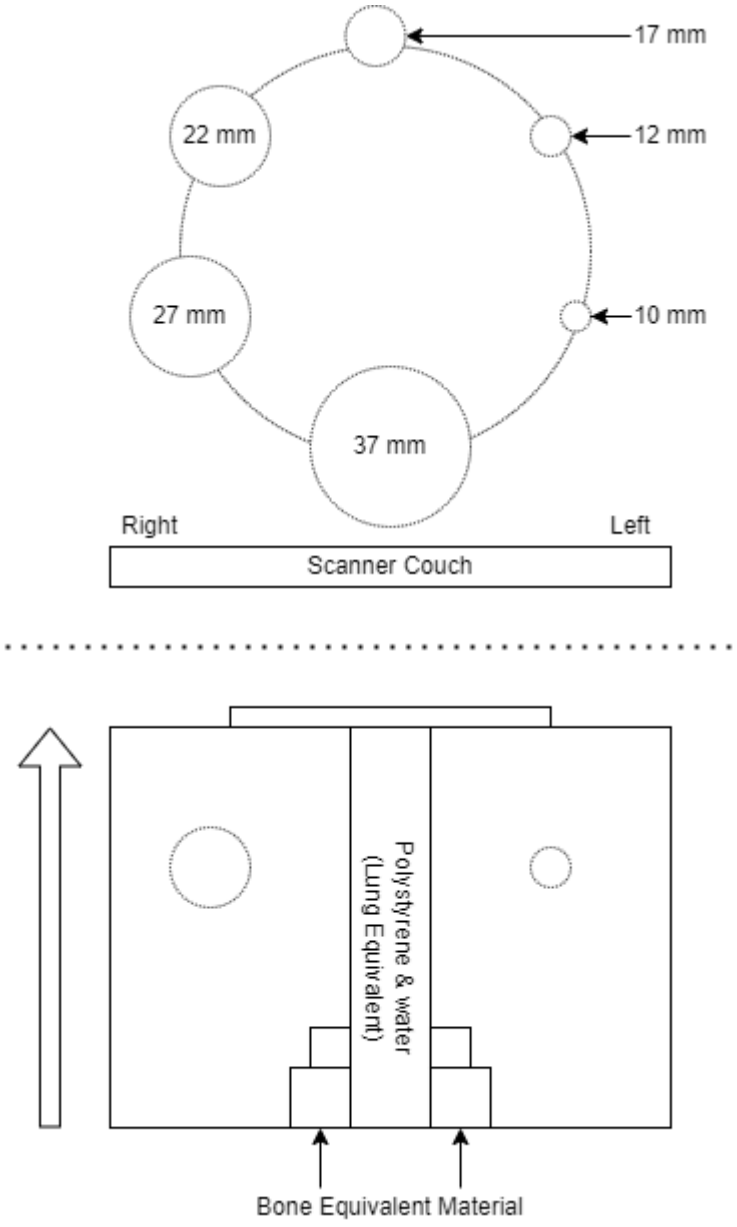

Figure 5-7: Layout of NEMA phantom used for ^{89}Zr verification measurements at PETIC.The arrow indicates direction into the scanner

5.4.4 NPL measurements

Calibration measurements at NPL were performed following the Mediso protocol as described previously. To enable later comparisons, the cylindrical and NEMA phantoms were measured using a standard clinical protocol after the calibration measurements. The two phantoms were placed at opposite ends of the patient bed (Figure 5-8) and scanned at intervals over a 21 day period. Measurements were taken with two frames covering the cylindrical phantom. Two measurements of the NEMA phantom were made, with a single frame centred over the spheres and a two-frame acquisition covering the whole phantom. Two CT measurements were performed on the phantoms prior to every PET acquisition, so that a 'high' and 'low' quality CT attenuation correction could be compared. The settings used for the CT and PET systems are listed in Table 5-3. Reconstructions were performed using the Mediso 'Teratomo 3D' OSEM-based algorithm using standard clinical settings. All nuclear data were checked prior to the beginning of the campaign and adjusted to the values presented in Chapter 3 where appropriate.

Modality	Parameter	Value (High Resolution)	Value (Low Resolution)
CT	Tube current	100 mA	50 mAs
	Tube voltage (kVp)	140 kV	80 kV
	Slice thickness	0.625 mm	1.25 mm
	Total collimation	10 mm	20 mm
	Single collimation	0.625 mm	1.25 mm
PET	Slice thickness	3.978 mm	
	Number of slices (1 frame / 2 frame)	38 / 63	
	Energy window	400-600 keV	
	Frame overlap	35 %	

Table 5-3: PET/CT acquisition parameters used for verification measurments on the NPL Mediso camera

To enable an assessment of long-term detector stability, a daily QC measurement was made using a solid ^{68}Ge cylindrical phantom throughout the course of the campaign.

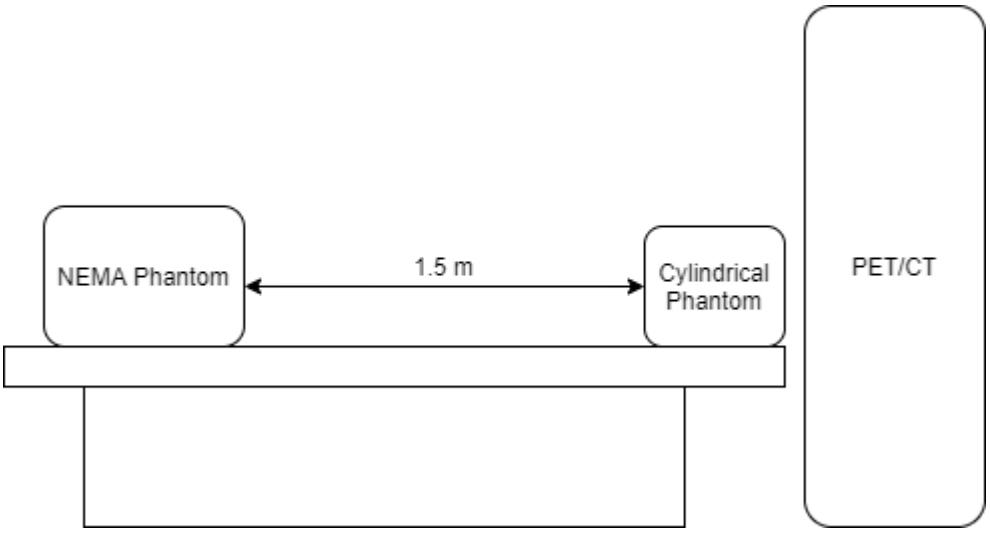

Figure 5-8: Positioning of the Verification phantoms on the Mediso scanner couch.

5.4.5 PETIC measurements

Both inactive and active background measurements were performed with the phantom placed on the end of the patient couch and centralised in the FOV. As a result of the camera dose optimisation capabilities, the tube current on the CT differs between the two measurements due to slight differences in the density of water and the carrier used. The PET acquisition parameters remained identical for both acquisitions and are summarised along with the CT acquisition parameters in Table 5-4. The nuclear data on the camera were checked prior to the measurements; a half-life of 78.41 h and a positron branching ratio of 22.7 % were noted which agree with accepted nuclear data evaluations. Images were reconstructed using the GE workstation, and the clinical 3D (ToF) OSEM based reconstruction with CT based attenuation correction was performed.

Modality	Parameter	Value (No Background)	Value (With Background)
CT	Tube current	122 mA	134 mA
	Tube Voltage (kVp)	120 kV	120 kV
	Slice Thickness	0.625 mm	1.25 mm
	Total collimation	10 mm	20 mm
	Single Collimation	0.625 mm	1.25 mm
PET	Slice thickness	3.27 mm	
	Number of Slices	83	
	Energy Window	400-600 keV	
	Measurement Time	30 minutes	

Table 5-4: PET/CT acquisition parameters for the PETIC verification measurements

5.5 Results and discussion

5.5.1 NPL stability checks

The daily QC measurements using the solid ^{68}Ge phantom showed that the PET system is nominally stable over many months. The standard deviation of the residuals was found to be 2.0 % and the individual measurements are shown in Figure 5-9. The uncertainties are estimated by taking the square root of the number of counts in each VOI.

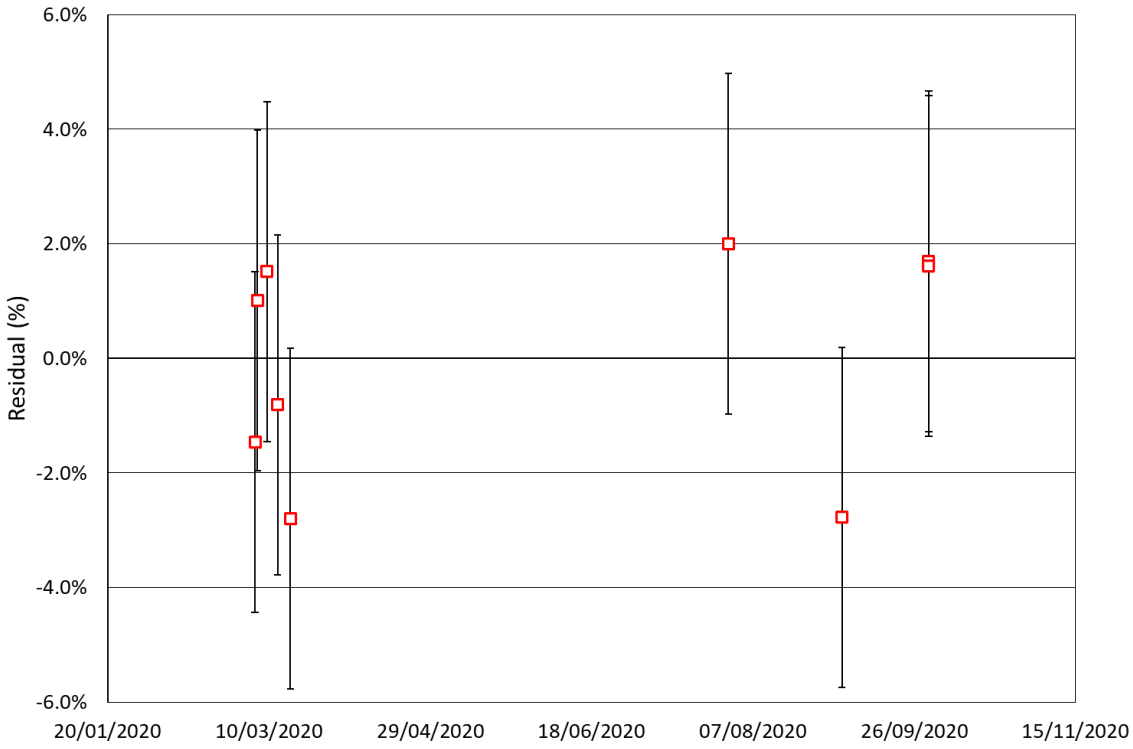

Figure 5-9: Plot of residuals from daily QC measurements using the solid ^{68}Ge cylindrical phantom.

5.5.2 NPL calibration measurements

The calibration results for RocketIO, ADC, gain, co-registration, timeshift and normalisation are not important in the context of this study, but it is important that they are performed correctly. The results from these calibration measurements will be used in future work when assessing uncertainties. The activity calibration determines an 'activity factor' for the system, which is used to convert counts per second into activity (of ^{18}F), and the results from this calibration were collated together with results from the previous year to determine consistency. Not enough is known about the uncertainties

relating to this factor. Therefore, the values are plotted on a control chart (Figure 5-10) without uncertainties but depicting the mean and standard deviation. The standard deviation of these results is 0.44 %, which indicates that the conversion of counts per second to activity on the system remains stable over long periods of time. Since this factor will be directly affected by the other calibrations, it implies that the system did not change significantly during the measurements in this study, which is further confirmed by the aforementioned consistency of the ^{68}Ge check source data.

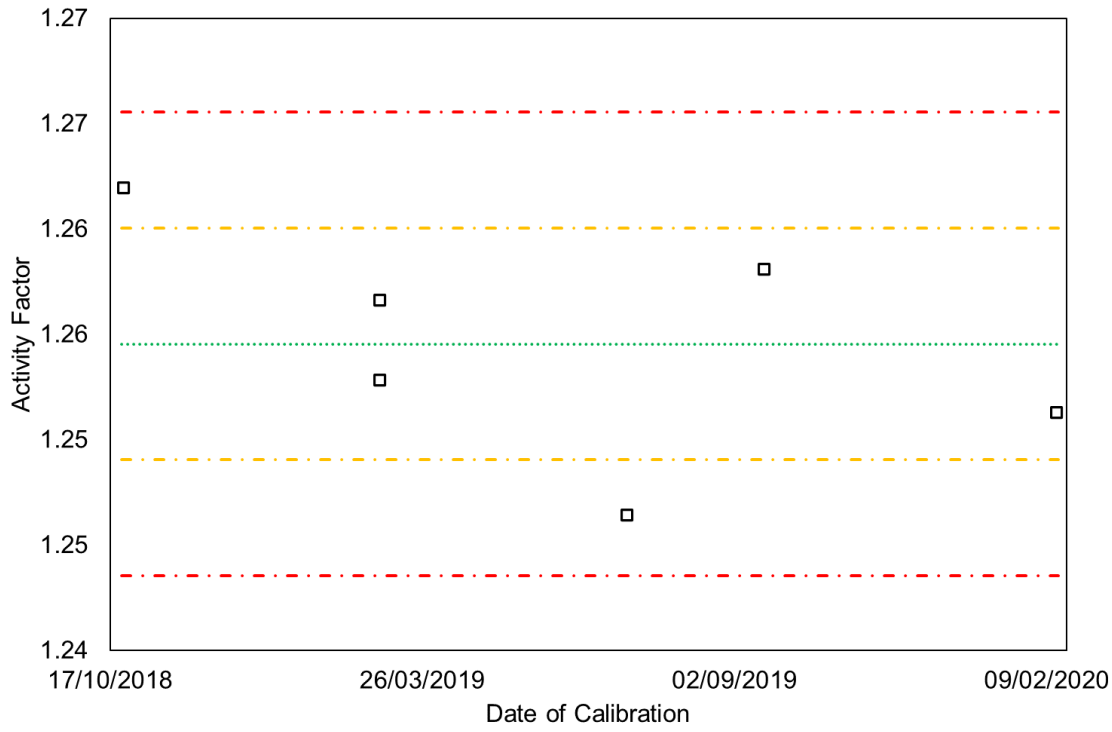

Figure 5-10: Control chart plotting activity factors for ^{18}F determined for the Mediso Anyscan PET/ system. The red lines represent 2 standard deviations from the mean, the orange lines represent 1 standard deviation and the mean is shown in green.

5.5.3 NPL verification measurements: cylindrical phantom

The activity recovery for ^{89}Zr was variable, depending on the method used. Mediso states that it does not support radionuclides other than ^{18}F, despite allowing the user to select a wide range of radionuclides within the software. To account for this, the images were processed by setting the radionuclide to both ^{89}Zr and ^{18}F. An additional manipulation was applied (offline) to the ^{18}F data to remove the branching ratio and decay corrections, and re-apply the appropriate corrections for ^{89}Zr.

When processed as ^{89}Zr the activity is 34-36% higher than expected (Figure 5-11). Good homogeneity throughout the multi-frame cylindrical phantom measurement indicates that the decay correction being applied seems acceptable, but there must be an error in branching ratio corrections. This was not caused by the inputted nuclear data since these were checked prior to measurement, and so it is likely this is a software problem.

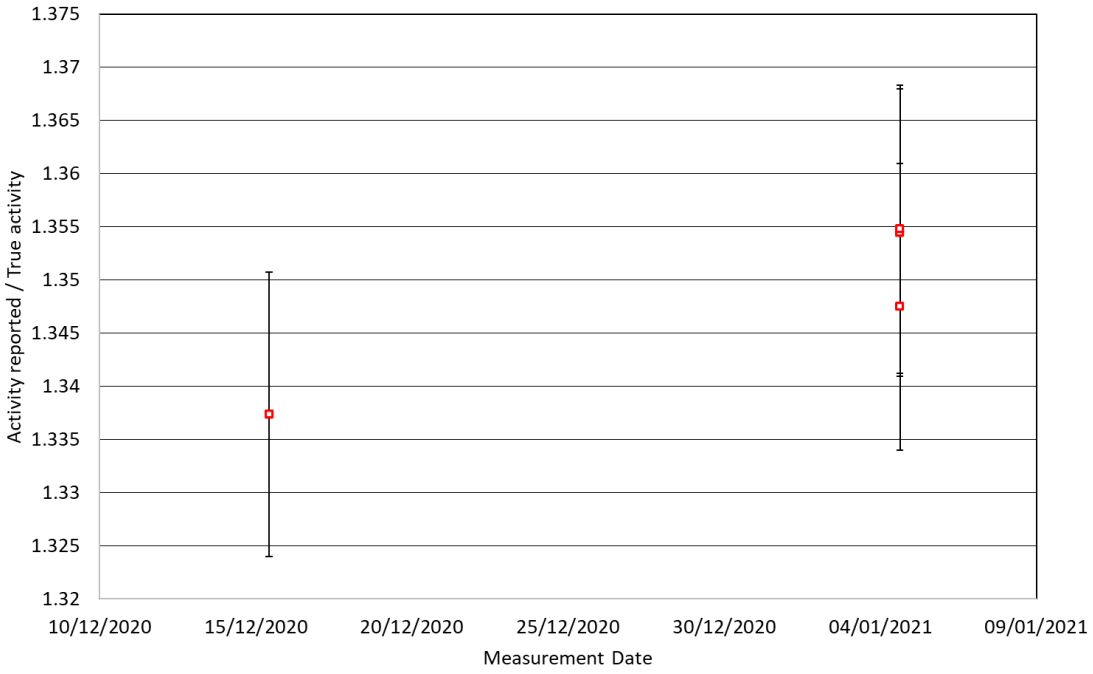

Figure 5-11: Activity recovery when setting radionuclide to ^{89}Zr and not applying any corrections to the data. .

Using the correction method previously mentioned, the values are in very good agreement with the true values, with a slightly low bias of around 4% (Figure 5-12). The limitations of this method are the need to process the data manually, and, if a multiple frame image is processed, the fact that the decay correction becomes difficult to apply throughout the overlap region. This is nicely demonstrated by the 1 hr multiple frame cylindrical phantom measurement (Figure 5-13), where a ratio of 1.20 (on average) is noted between the first and second frames (excluding the overlap region). The decay correction factor that would be applied to a 60 minute ^{18}F measurement is 1.20, and so

it is clear that this difference is due to the decay correction for ^{18}F being applied to a ^{89}Zr source which would decay very little during the measurement time.

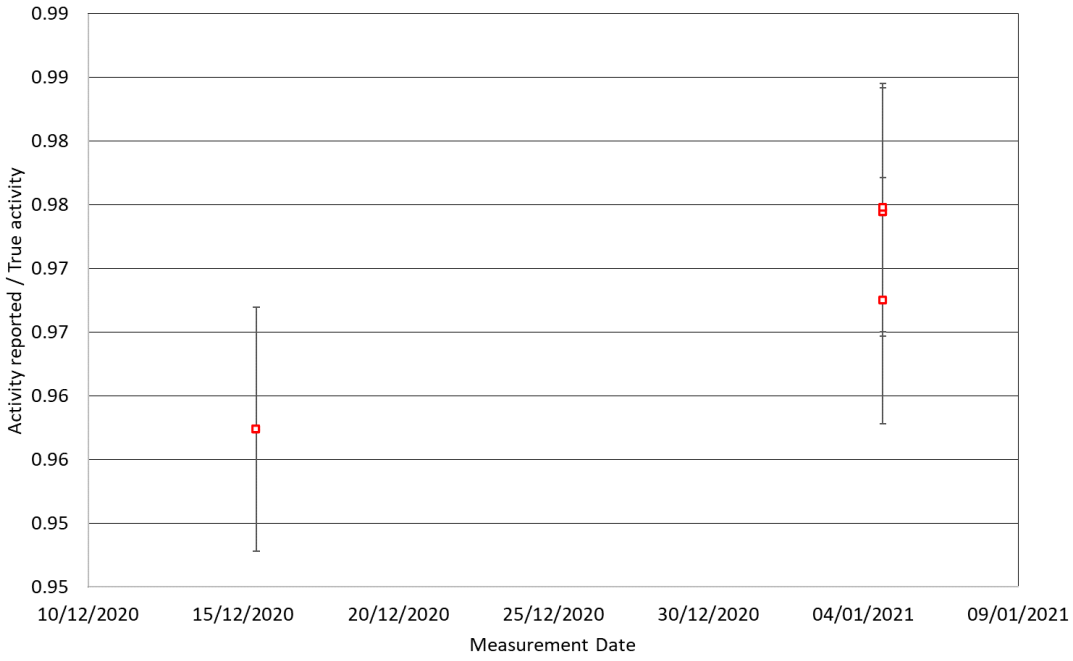

Figure 5-12: activity recovery when setting radionucldie to ^{18}F and applying manual (offline) corrections for decay and branching ratio.

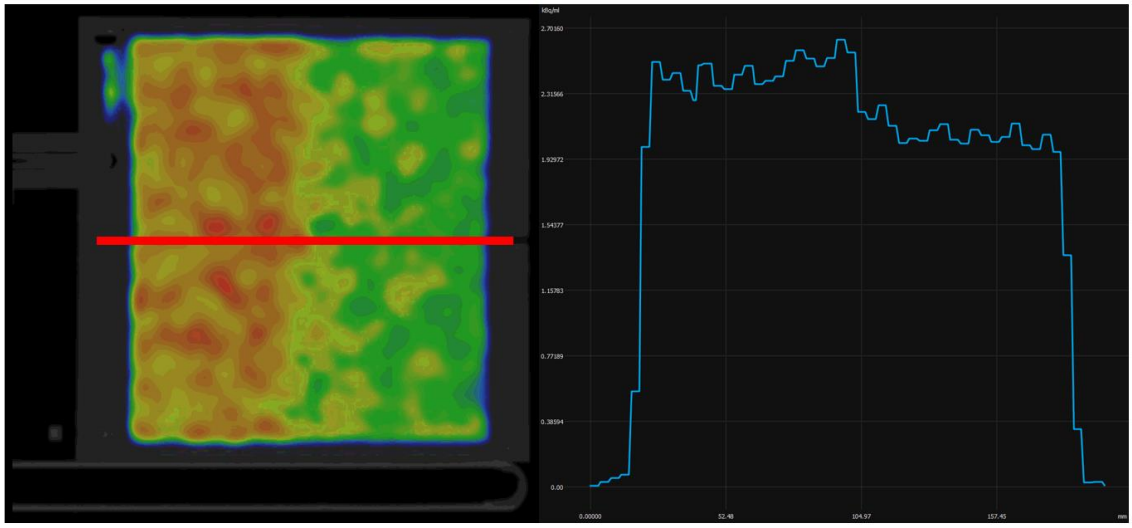

Figure 5-13: Profile drawn through cylindrical ^{89}Zr phantom with two frames when reconstructed using ^{18}F settings.

5.5.4 NPL verification measurements: NEMA phantom

The same bias between the manually corrected and software determined values for activity are present in the NEMA phantom, confirming the cylindrical phantom

measurement results. As expected from previous literature, the recovery curve for ^{89}Zr indicates that activity is measured lower for the smaller spheres compared with ^{18}F (Figure 5-14). As the ^{18}F calibration protocol only requires filling of the 4 smallest spheres, this dataset is normalised to a large VOI drawn in the background region of the phantom and compared to the true activity. For ^{89}Zr the values are shown relative to the largest sphere.

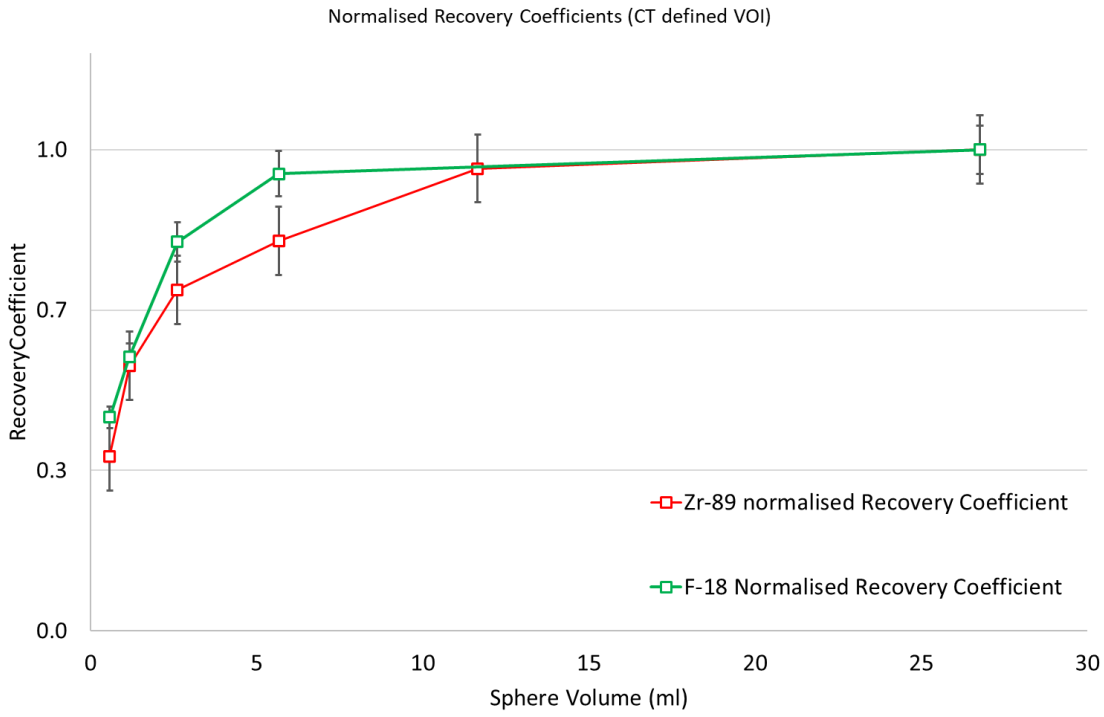

Figure 5-14: Recovery coefficient curves for ^{18}F and ^{89}Zr.

5.5.5 PETIC verification measurements

To determine scanner quantification accuracy, a large VOI (50 mm diameter) was drawn around the largest sphere in the inactive background scan, and four 50 mm diameter VOIs were drawn in the active background scan, with a mean taken to confirm homogeneity of the solution. The volume of the large 50mm sphere drawn in the active background was determined by multiplying the number of pixels within the VOI by the volume per pixel and assuming 1 ml was equivalent to 1 g of solution. The results showed that for the 50 mm VOI located around the large sphere with no background present, the

activity differed by 11 % from the standardised value. For the same size of VOI drawn in the background solution, the activity is on average 9.7 % different from the standardised value. These two values are in statistical agreement with each other (although not with standardised activity value) when considering the uncertainty on the activity values is 1 % for the activity in the Spheres and 1.5 % for the activity in the background cavity (Table 5-5). The percentage standard deviation of the four 50 mm spheres drawn in the active background was 0.90 %, indicating good homogeneity and reproducibility of the results in this region.

	Active mass (g)	Activity concentration (kBq g^{-1})	Difference
Inactive BG 50 mm VOI	26.523 (20)	338	11 %
Active BG 50 mm VOI	65.25 (20)	14.59	9.1 %
	65.23 (20)	14.60	11.1 %
	64.99 (20)	14.87	10.2 %
	65.13 (20)	14.65	9.5 %
Average (Active BG, 50mm VOI)	-	14.68	9.7 %

Table 5-5: Results from PETIC ^{89}Zr NEMA phantom verification measurements

Uncertainties arising from the imaging components are noticeably absent, and this is due to a lack of knowledge of detector performance. To enable an indicative budget to be determined, the uncertainty components listed in Table 5-6 were considered and included in the results. The statistical component was determined by converting activity to total counts and taking the square root. This is not mathematically correct due to the likelihood of scaling and other factors being applied during the reconstruction process, but it gives a useful indication of the statistical uncertainty. The scanner stability was taken from data previously acquired on the Mediso system, under the assumption that both would be similar. Attenuation correction uncertainty was estimated by taking the

difference in total image counts between the non-attenuation corrected image and the attenuation corrected image and assuming an uncertainty of 10 %. Notably missing components are those relating to the corrections for random coincidences and scatter; these are more challenging to estimate and so they have been omitted at this point.

Uncertainty Component	Value (%)
Statistical*	0.20
Scanner Stability*	2.0
Homogeneity	0.90
Activity Uncertainty	1.5
Decay (half-life)	0.10
Weighing	0.3
Attenuation Correction*	4.3
Combined uncertainty	5.1

Table 5-6: Example uncertainty budget for PETIC imaging measurments. The starred components have been estimated.

Image quality was assessed by inspecting recovery curves, which were established using both the active and inactive background phantoms. The results show that there is no significant difference between the two recovery curves when comparing values relative to the largest sphere (Figure 5-15). Comparison with the values from the NPL recovery curve measurements show a consistent trend between the two systems, with a slightly lower sensitivity being apparent on the GE system for most of the spheres Figure 5-16.

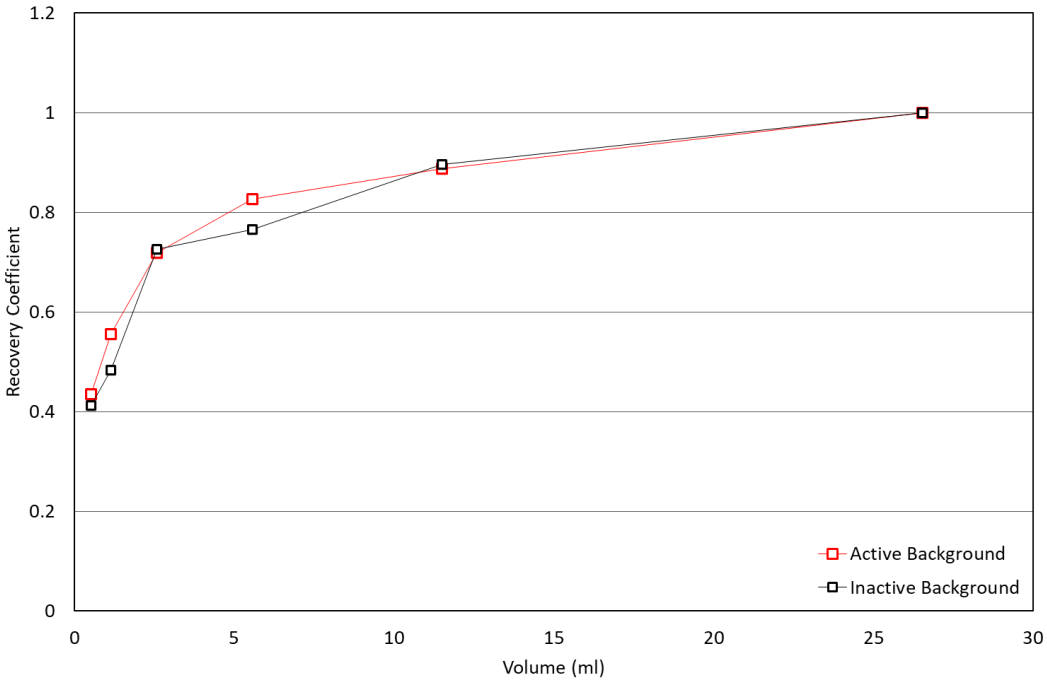

Figure 5-15: PETIC recovery curve normalised to the largest sphere with inactive background (black) and radioactive background (red).

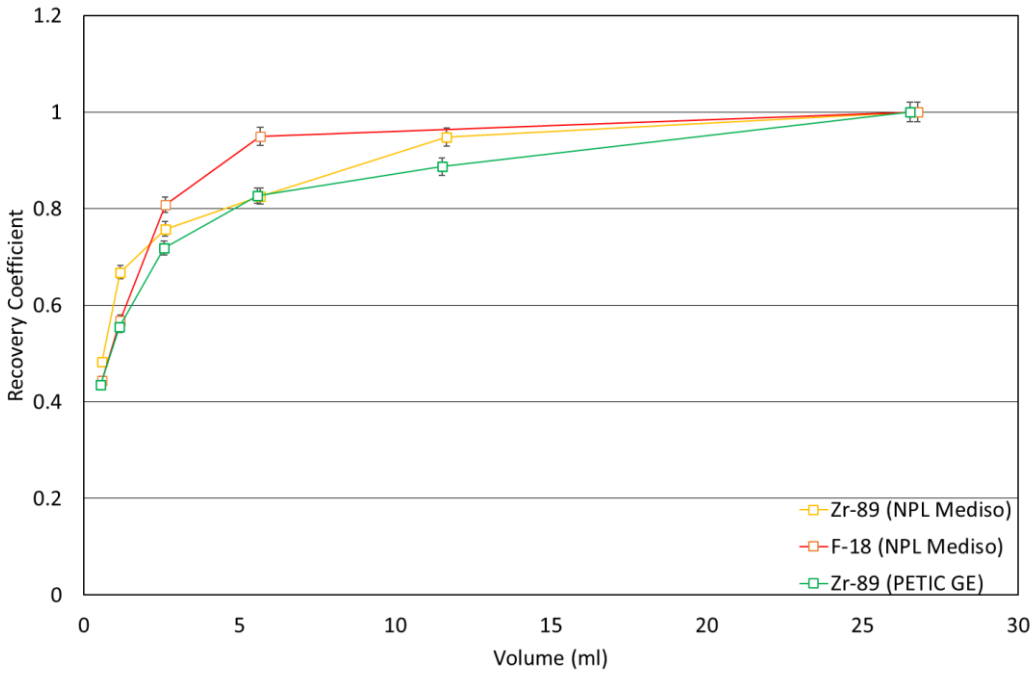

Figure 5-16: PETIC and NPL recovery curves relative to the largest sphere for ^{89}Zr and ^{18}F.

Figure 5-17 shows the PETIC and NPL data plotted alongside the Research for Life (EARL) accreditation limits for ^{89}Zr (Kaalep et al., 2018b). These recovery curve performance limits are used when setting up clinical trials to establish a baseline

equivalence between centres (not assessment of activity measurement accuracy). They are a good indicator that the two systems are performing adequately when measuring ^{89}Zr.

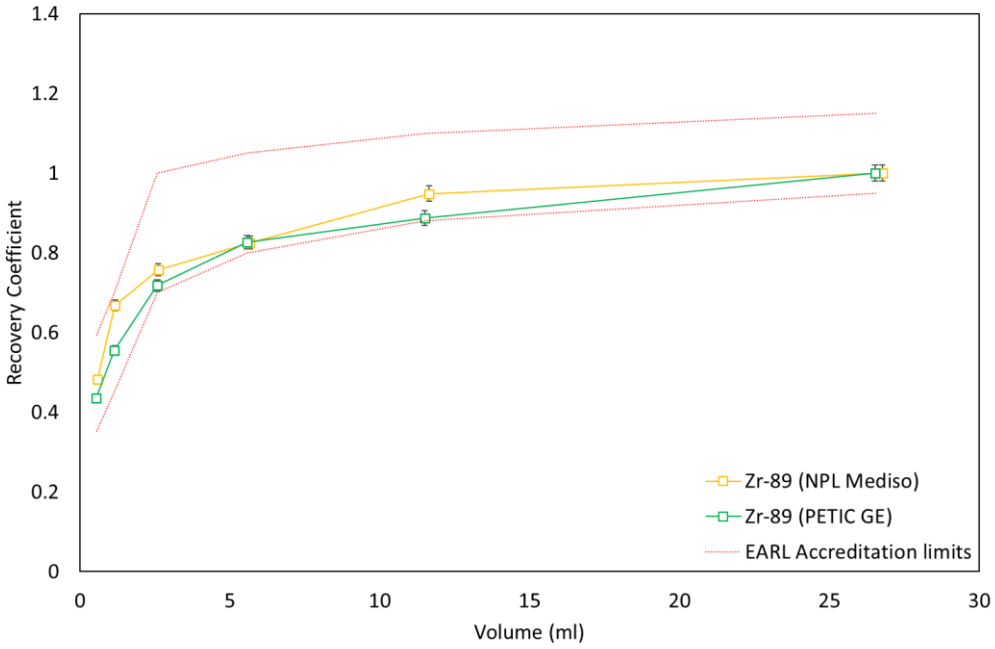

Figure 5-17: Graph showing both PETIC and NPL data alongside EARL accreditation limits

5.6 Chapter summary

The results show that activities in standard phantoms can be measured on clinical imaging systems to within 10 %, but care must be taken when using manufacturer software. A manual correction was applied to the ^{89}Zr data taken on the NPL Mediso system due the manufacturer not supporting quantitative imaging with radionuclides other than ^{18}F. This caused issues when trying to correct multiple-frame images due to the overlapping of frames. It was also found that a consistent difference was apparent in the datasets when reconstructed with ^{89}Zr settings, which indicates that the half-life correction may be being performed correctly. However, the conversion from ^{18}F to ^{89}Zr activity is flawed and this problem should be fixed by the vendor. An offline correction, whereby the decay and branching ratio of ^{18}F is removed and the same reapplied for

^{89}Zr, has been developed. Although not practical for routine clinical work, it is a valuable check when commissioning a system. in the verification measurements, the PETIC system showed a consistent 10% bias, which could indicate either a problem in the calibration or a problem with the conversion from ^{18}F to ^{89}Zr by the manufacturer software. Despite the lack of accuracy, both systems showed a consistency when measuring ^{89}Zr, which indicates that the use of correction factors would enable comparative measurements to be done.

Image quality (in terms of recovery coefficients) on both systems was shown to be within the published EARL accreditation limits.

Chapter 6: General discussion

The overall aim of this project was to establish traceability for ^{89}Zr imaging using pre-clinical and clinical systems. At the beginning of this project, there was no available activity standard of ^{89}Zr from a National Metrology Institute and, therefore, the first step was to perform a new primary standardisation of the radionuclide. Further research identified that the available nuclear data were discrepant, and so new measurements of nuclear data were required before proceeding with the primary standard. Determination of calibration factors and dial settings at NPL and at PETIC using this standard was essential due to the inconsistencies found in the literature. To complete the measurement chain, imaging on pre-clinical and clinical systems was performed. Standardised solutions were used to assess activity quantification accuracy when measuring simple test phantoms filled with ^{89}Zr, and these results were compared to similar measurements of ^{18}F (where possible) and international performance standards.

6.1 Standards and nuclear data

The primary standardisation focussed on the CIEMAT/NIST technique due to difficulties encountered with other methods. The CIEMAT/NIST technique relies on detector modelling using nuclear data. Therefore this led to a somewhat iterative process of performing a standardisation and determination of nuclear data followed by re-evaluation of the standard to determine the effect of changes in nuclear data. It was found that the new nuclear data did not significantly affect the results and, therefore, the existing nuclear data was used to avoid creating an incestuous cycle within the standardisation. It should be noted that the positron branching ratio was not remeasured due to the work that would be required to do this. Instead, the model was reassessed by varying the value of the positron branching ratio within the uncertainties quoted in the literature, and no significant variation in detector efficiency was noted. The differences in nuclear data are considered as part of the overall uncertainty budget.

The measurements by TDCR were not successful due to hardware problems with the operation of the TDCR counting system at NPL. The LHNB supplied ‘MAC-3’ unit, which is responsible for applying resolving times, dead time and for determining triple and double coincidences (using analogue electronics) was not functioning correctly at the time of the measurements. The system has since been updated and converted to a digital acquisition system, which is currently under testing at NPL for use in future. Despite this, the detector modelling was performed as part of this project in expectation of future requirements.

Measurements by 4πβ-γ coincidence counting using the NPL digital coincidence counting system were undertaken at various stages of the project with mixed success. Initial measurements demonstrated that by using a gate applied over the 511 keV positron emission, it was possible to extrapolate using a linear relationship and obtain a result for activity concentration by correcting for the branching ratio. This led to an overall standard uncertainty of approximately 3 % due to uncertainties in the branching ratio (1.2 %) and in the extrapolation itself caused by the relatively low efficiencies (80 % positron efficiency). To improve the efficiency, the high voltage was increased to make use of the Auger and x-ray emissions detected in the beta channel, in coincidence with a gate applied over the 1745 keV gamma emission. Once again, the calculated efficiencies were relatively low (85 %) and due to interference with conversion electrons and other non-coincident emissions, the extrapolation was not linear, and a series of polynomial fits were used. Compounding this problem was the low emission intensity of the coincident gamma (0.123 %), which led to data collection problems and poor statistics in the gamma channel. These problems led to large variations in results between samples, as can be expected when extrapolating a polynomial over such a range. Attempts were made to increase efficiency using different scintillation cocktails, increasing the high voltage in the beta channel and replacing the HPGe detector with a NaI detector in the gamma channel; however, the results remained inconclusive.

The half-life measurement was performed in 2015 and, at the time of the calculations, it was presented with an order of magnitude better uncertainty than all other half-life values quoted in the literature. The value was in statistical agreement with the evaluations of DDEP and ENSDF, however there were significant discrepancies in the dataset that was used. During the course of this project, an additional measurement was performed by CIEMAT in Spain (Garcia-Torano et al., 2018) and the result was close to the value determined in this work. It seemed prudent to perform a re-evaluation of the half-life to determine a new reference value, and assess if this had a significant impact on the other measurements performed during this project. The new value was in statistical agreement with the evaluation. However, the overall uncertainty has been dramatically reduced which, in-turn, will reduce the uncertainty due to decay correction in future work. This shows the importance of performing accurate half-life measurements using radiochemically pure solutions and carefully controlled equipment with a robust quality assurance system in place.

The results of the gamma emission intensity measurements highlight large deviations from those in the existing literature. The results presented were determined using equipment calibrated using 19 independent standards of radioactivity, creating 53 calibration points in the full-energy peak detection efficiency curve. No other publication in the existing literature can demonstrate such attention to detail in determining the efficiency curve, and this goes some way to explaining the difference in the final uncertainty values. Importantly, the absolute emission intensity of the 909 keV gamma emission (relative to which all other gamma emissions were expressed) was measured and compared to existing published data, and found to be in statistical agreement. This demonstrates that the existing data for this well-characterised emission are reliable and this is reflected in the small standard uncertainty attributed to them. Confirmation of gamma emission intensities by measurement using absolute means is an important step

in the chain of traceability, and will benefit the future uses of such data in modelling applications such as dosimetry or gamma spectrometry calculations.

Calibration factors were determined for the NPL secondary ionisation chamber systems, which are used for the dissemination of standards to the wider community. The derived calibration factors were validated by gamma spectrometry measurements and by using a Monte Carlo based model of the system, albeit for a slightly different geometry. The good agreement between these methods can be largely attributed to the well-known 909 keV gamma emission intensity, which will dominate the response in an ionisation chamber and hold the highest weighting when performing activity calculations by gamma spectrometry. The derivation of a dial setting for a clinically useful geometry (10 ml Schott vial) was immediately important when performing measurements in a clinical setting, and will allow any operator of a Fidelis radionuclide calibrator to be able to measure ^{89}Zr with confidence.

Dial settings were determined for Capintec and Atomlab radionuclide calibrators to give a point of reference for clinical users of this radionuclide. Unlike the Fidelis calibrator, these devices are not all identical, and a single setting cannot be applied to all units of the same make/model with a known degree of accuracy. However, unlike the available published data, the presented results are based on a primary standardisation and are in a clinically useful geometry. Therefore, they will provide a useful reference setting for sites that are starting out in performing measurements and can lead to a 10% improvement in activity measurement accuracy.

6.2 Pre-clinical imaging

The methodology used in this study aimed to provide a verification for ^{89}Zr activity quantification using means available in the preclinical setting. By using widely available phantoms and simple geometries, such as syringes, it was shown that traceable phantoms can be created and used for imaging. The only requirement is access to a

calibrated radionuclide calibrator or a calibrated source. This methodology is also readily transferrable to other radionuclides, provided the radionuclide has been standardised by a NMI, which can disseminate the information. The study showed that it is possible to obtain results for activity quantification within 5% of the true value for a simple syringe geometry, and that a typical pre-clinical system is repeatable over several half-lives, allowing long term observation of activity accumulation in animal studies. The creation of phantoms with traceable activity is important when performing calibration steps, and verification measurements demonstrate a system's capability in terms of quantification of activity.

The results showed an overall positive bias in the ^{89}Zr activity determination, which could be attributed to several different factors. Since there is limited knowledge of the methodology for converting the ^{18}F calibration to that of ^{89}Zr, it is possible that an error in this calculation is causing the bias. To minimise the effect of incorrect nuclear data, prior to reconstruction the half-life and other data were updated in the reconstruction software using the values supplied in this project (with the positron branching ratio taken from the evaluated literature). Another source of potential bias could be downscatter from the prevalent 909 keV gamma emission. The additional scattering into the 400-600 keV gamma window may lead to insufficient random coincidence correction if it is not properly accounted for in the software. To investigate this would require work outside the scope of this study; however, details of suggested future work can be found in section 6.5.5. This is the first time that quantification for ^{89}Zr has been demonstrated relative to a traceable activity measurement. Therefore, there is no suitable comparison in the published domain as yet, but it is hoped that this work will lead to further study in this area.

Long term stability of imaging systems can play an important role in some studies, as well as contributing to the overall uncertainty budget. This work has shown that the performance of the system tested is reproduceable over a 22 day period to within 2 %

for a standard check source. It did not intend to be an exhaustive investigation of image quality but did demonstrate that some aspects of image quality on this system are comparable to that in other publications.

This study has shown that establishing a traceable link for activity measurement is possible in the pre-clinical environment, provided care is taken in phantom preparation and testing is undertaken when novel radionuclides are being used. By performing the tests described, a pre-clinical site can reinforce conclusions drawn in quantitative studies and have greater confidence in results, which can accelerate progression of work into the clinical realm.

6.3 Clinical imaging

The approach taken in this study was akin to that taken in the pre-clinical work. Clinical imaging systems were assessed using methods that would typically be available to a clinical centre, with additional measurements being performed on the research scanner at NPL, which is not used clinically. The comparison between the NPL and PETIC systems used the same methods but additional imaging was possible at NPL to provide datasets for the future investigation of uncertainties. As with the pre-clinical work, it was shown that calibrated phantoms can be created using clinically available equipment and that the methodologies could be expanded to other radionuclides with ease.

The results show a slight disparity in quantitative accuracy between a system calibrated directly against a secondary standard ionisation chamber, and a clinical system calibrated against a field instrument. Since this study looked at equipment from two independent camera manufacturers, it is possible that this disparity is due to differences in corrections applied during acquisition or reconstruction, rather than the initial calibration. In any case, it demonstrates that a clinical system can quantify the activity of simple ^{89}Zr sources to within 10%. The Mediso scanner does not officially support quantification of ^{89}Zr activity and, therefore, it would be inappropriate to cast judgement

on the results shown in this study using the ^{89}Zr reconstructed data. However, it does highlight the need for clinical users to perform such measurements in order to determine the suitability of their system prior to performing imaging studies. As with the pre-clinical results, the activities on both systems were overestimated when using ^{89}Zr settings, which indicates that there may be errors in determining the activity. The offline corrections performed using NPL data, which were reconstructed as if they were ^{18}F, showed that it is possible to obtain a result very close to the true activity value, although overlapped FOV images are difficult to correct using this approach. The activities on the Mediso system using the correction were slightly underestimated and it is unclear why this should be the case. It is possible that the Mediso reconstruction software performs radionuclide specific corrections for things such as positron range, which will be affected by incorrect radionuclide settings for the reconstructions. The estimated uncertainties show that the results are in statistical agreement with the true value. However, since there are insufficient data to present a complete uncertainty budget, it would be inappropriate to make this claim at present.

Determining system stability on the Mediso system by the measurement of a long-lived check source and by monitoring changes in the derived activity factor, demonstrates that some simple measurements can be performed in order to assess aspects of the PET imaging uncertainty. However, a good deal of work is still required in this area before a full uncertainty budget can be realised.

Image quality results, in terms of volume recovery coefficients, were compared alongside international performance criteria and found to agree, which indicates that both systems are comparable in terms of image quality.

Overall, this work has shown that the application of standards of radioactivity in imaging is achievable for calibration and verification measurements on clinical imaging systems. Comparability in clinical trials, as well as in patient treatment, is critical and performing the validation measurements described will give greater confidence when drawing

conclusions. This work has also highlighted the importance of establishing traceability between a primary standard and the clinical site before proceeding to prepare phantoms to test the imaging systems. Ultimately, imaging measurements lead to a patient diagnosis, or for treatment staging, and therefore traceability should be an expectation rather than a luxury.

6.4 Uncertainties

This project highlights some important aspects of uncertainty analysis, which are missing from PET measurements in a clinical setting. When performing activity measurements using a radionuclide calibrator, there is clear guidance on the methodology required to establish an uncertainty budget (Gadd et al., 2006; Zanzonico, 2008; Zimmerman and Judge, 2007). Whilst in practice this may not be followed in every instance, there is a clear understanding of the required process and the work to establish an uncertainty budget is not beyond the capabilities of a clinical scientist. When considering PET imaging, there are several additional complications (such as the black-box nature of the software), which mean that the establishment of an uncertainty budget is far more challenging. The results in this study show that some components (such as long-term stability and overall accuracy) can nominally be assessed by the use of test objects. However, the more fundamental components (such as the effect of different corrections and calibrations) require a more complex approach to determine the contribution to a final uncertainty budget. To assess these components properly, it is almost certainly necessary to use open source software such as STIR (Thielemans et al., 2012b) combined with an iterative measurement process so that all aspects of the propagation can be examined and this is discussed in section 6.5.3.

6.5 Future work

This study covered a wide range of techniques in the measurement of ^{89}Zr activity and has opened the possibility of further investigations in a number of areas.

6.5.1 Positron branching ratio measurement

This study gave a comprehensive report of the primary standardisation and nuclear data. However, a notable omission was the measurement of the positron branching ratio, which has been identified as a key component in the uncertainty of PET imaging activity measurements. It would seem trivial to perform a gamma spectrometry measurement of the positron branching ratio using the equipment described in Section 3.6 in the same manner as the other gamma emissions, but this is not practical in reality. When measuring positrons, it is important to be aware of the positron range and the effect this has on sample geometry. For gamma spectrometry measurements, it is acceptable to assume that a particular photon emission occurs within the sample, and the use of a mixed radionuclide source to calibrate a system is commonplace. When positrons are emitted, their annihilation may occur within the sample, within the walls of a container, within the air surrounding a source or even within the detector itself. Since positron energy is nominally proportional to range, a system cannot be calibrated for positron emitters in an accurate manner. To tackle this problem, it is suggested to use a positron annihilation shield, typically constructed of metal or plastic, combined with a Monte Carlo model to determine the uncertainties attributed to the measurement. When combined with a primary standard, an absolute determination of the branching ratio can be performed. This is a significant piece of work, since it requires the calibration of a gamma spectrometry system for a unique geometry using a range of positron emitters, which themselves must be standardised, along with the creation of a suitable Monte Carlo simulation.

6.5.2 International comparison of ^{89}Zr activity measurements

It was attempted several times during this study to submit a ^{89}Zr standard to BIPM to enable comparison with other NMIs performing primary measurements. The reasons for not completing this were the logistical difficulties in receiving the sample at BIPM

(because of licensing issues on the part of the French authorities) and export control issues from the UK following the UK's departure from the European Union.

The international comparison of standards is important to ensure global harmonisation of measurement, and it has been proposed to the CCRI (II) working group that an international comparison exercise is performed with ^{89}Zr to allow multiple institutions to perform the standardisation and compare results. This would be done under the guise of a pilot study, whereby a single lab prepares multiple samples that are shipped to each organisation plus BIPM, and all results are compared to determine a key comparison reference value (KCRV).

6.5.3 Uncertainties in PET imaging

To establish baseline uncertainties in PET imaging requires access to raw event data from a PET scanner, along with detailed knowledge of how and when corrections are performed to these data during the reconstruction process. Typically, a measurement can be repeated multiple times in order to establish a variance, which can, in turn, be incorporated into an uncertainty budget. In the case of PET imaging, this would require hundreds of measurements being undertaken; this is impractical without a significant resource and time commitment. An alternative to this method is to use 'bootstrapping', whereby random samples of example datasets are used to determine the variance using software. This methodology can then be used to build probability density functions for individual components, which can later be combined to construct a full uncertainty budget. The calibrations mentioned in section 5.2.2 give a good starting point for this process, whereby creating a modified set of calibration tables for each measurement and running reconstructions would enable quantification of the variance caused by errors in each calibration. By performing this process using modified software such as STIR, it would then be possible to incorporate the uncertainties into the images. Since analysing all uncertainty components would be impractical for clinical users, it is important that the largest contributing components are identified and quantified to enable sites to focus

research on them. It is hoped that the results of such an uncertainty analysis would lead to manufacturers providing tools within proprietary software to enable reporting of uncertainties during routine clinical measurements.

6.5.4 Commissioning tests for quantification of novel radionuclides

When commissioning either a pre-clinical or clinical PET system, number of tests are performed to determine to operational parameters of a system (NEMA, 2008, 2012). These tests focus on imaging with ^{18}F and are an important part of any commissioning process, but there little further study is performed when considering other radionuclides. To improve the accuracy of measurements performed with non ^{18}F radionuclides, it is recommended that a study should be conducted prior to imaging projects to establish baseline performance of the system for these radionuclides. This would add confidence to results obtained and would go some way to establishing harmonisation for studies involving novel radionuclides. As a minimum, there should be a test to determine quantitative accuracy for a large volume and measurement of the standard NEMA test phantom to provide recovery coefficient curves for the system. Ideally, the full suite of NEMA tests would be carried out in order to provide information on image quality as well as quantitative accuracy, but it is accepted that this may not be practicable for many clinical sites.

6.5.5 Effects of downscatter in PET imaging

Several radionuclides in PET have high energy photon emissions, which will create downscatter into the imaging window (typically 400-600 keV). Following an extensive literature search, there is little evidence to be found regarding the effect of this increased Compton background on the quantification or image quality of PET images, and whether existing software performs any correction for such events. To better understand the effect, it is proposed to establish a Monte Carlo model of a PET camera and simulate measurements of radionuclides such as ^{89}Zr. By modifying the simulation to vary the intensity of the higher gamma emission in simple geometries, the effect can be quantified

and potential solutions for correction can be presented. Ideally the simulation would be verified against a real system to ensure that the results are realistic. Verification could be performed with a radionuclide such as ^{89}Zr as well as using a ‘clean’ positron emitter (such as ^{18}F) combined with another radionuclide which emits photons above 511 keV and does not have any other emission within the typical energy window (400-600 keV).

Chapter 7: Conclusion

This thesis has taken a novel radionuclide through the measurement chain from primary activity standardisation to clinical imaging systems in a traceable manner. Provision of accurate activity standards is key to these measurements and they are equally reliant on good knowledge of nuclear data such as half-life and gamma emission probabilities. The evaluation of nuclear data is important when performing decay corrections, Monte Carlo simulations and gamma spectrometry, and this work has contributed to the available data as well as recommending new evaluated values. Secondary standards and field instruments used in the clinical setting are valuable tools that can be readily calibrated to within 2 % for ^{89}Zr. The creation of imaging phantoms for calibration and verification in a clinical setting has shown that imaging systems are consistent and comparable in certain circumstances, but that care should be taken to evaluate the capabilities of these systems before clinical use. This work has brought traceability to patient imaging studies closer, but has not addressed the difficulties of incorporating uncertainties into clinical imaging. The number of future research opportunities, which are critical to the goal of traceable activity measurements in patient imaging, highlight the continued efforts required in this field. As this new era of metrology in clinical imaging is dawning, it is hoped that many more research institutes will engage with their clinical partners to take up the challenge and contribute to this emerging field, which will directly impact patients.

References

Adams, H., van de Garde, E.M., van Moorsel, C.H., Vugts, D.J., van Dongen, G.A., Grutters, J.C., Keijsers, R.G., 2019. [(89)Zr]Zr-rituximab PET/CT activity in patients with therapy refractory interstitial pneumonitis: a feasibility study. American journal of nuclear medicine and molecular imaging 9, 296-308.

Ahlawat, S., Khandheria, P., Del Grande, F., Morelli, J., Subhawong, T.K., Demehri, S., Fayad, L.M., 2016. Interobserver variability of selective region-of-interest measurement protocols for quantitative diffusion weighted imaging in soft tissue masses: Comparison with whole tumor volume measurements. Journal of Magnetic Resonance Imaging 43, 446-454.

Allred, K., Sanders, Q., Prince, M., Korn, R., Wilson, I., Le, W., Weiss, A., Abbott, A., Hays, D., 2021. Phase II, open label, multi-dose study of 89-Zr-Df-IAB22M2C (CD8 Immuno-PET Tracer): technical handling and injection instructions for optimal tracer administration.<sup/&gt. Journal of Nuclear Medicine 62, 3004.

Anger, H.O., 1958. Scintillation camera. Review of scientific instruments 29, 27-33.

Avila-Rodriguez, M.A., Selwyn, R.G., Hampel, J.A., Thomadsen, B.R., Dejesus, O.T., Converse, A.K., Nickles, R.J., 2007. Positron-emitting resin microspheres as surrogates of ^{90}Y SIR-Spheres: a radiolabeling and stability study. Nuclear Medicine and Biology 34, 585-590.

Baerg, A.P., 1973a. The efficiency extrapolation method in coincidence counting. Nuclear Instruments and Methods 112, 143-150.

Baerg, A.P., 1973b. Pressurized proportional counters for coincidence measurements. Nuclear Instruments and Methods 112, 95-99.

Baerg, A.P., Bowes, G.C., Adams, R.J., 1966. Calibration of Radionuclides with a Coincidence System using a Pressurised Proportional 4π ß-Detector paper SM-79/12, I.A.E.A. Symposium on Standardisation of Radionuclides. IAEA.

Barnothy, J., Forro, M., 1951. Coincidence Methods of Measuring Disintegration Rates of Radioactive Sources. Review of Scientific Instruments 22, 415.

Bateman, H., 1910. Solution of a system of differential equations occurrig in the theory of radioactive transformations. Proceedings of the Cambridge Philosophical Society.

Baur, B., Andreolli, E., Al-Momani, E., Malik, N., Machulla, H.-J., Reske, S.N., Solbach, C., 2014. Synthesis and labelling of Df-DUPA-Pep with gallium-68 and zirconium-89 as new PSMA ligands. J Radioanal Nucl Chem 299, 1715-1721.

Bé, M.-M., Chisté, V., Dulieu, C., Browne, E., Chechev, V., Kuzmenko, N., Kondev, F., Luca, A., Galán, M., Pearce, A., Huang, X., 2008. Table of Radionuclides (Vol. 4). Bureau International des Poids et Mesures.

Bé, M.M., Chisté, V., Dulieu, C., Browne, E., Baglin, C., Chechev, V., Kuzmenko, N., Helmer, R., Kondev, F., MacMahon, D., Lee, K.B., 2006. Table of Radionuclides (Vol.3). Bureau International des Poids et Mesures.

Bé, M.M., Chiste, V., Dulieu, C., Browne, E., Chechev, V., Kumenko, N., Helmer, R., Nichols, A., Schonfeld, E., Dersh, R., 2004. Table of Radionuclides (Vol. 1). Bureau International des Poids et Mesures, Paris.

Bé, M.M., Chisté, V., Dulieu, C., Kellett, M.A., Mougeot, X., Arinc, A., Chechev, V.P., Kuzmenko, N.K., Kibédi, T., Luca, A., Nichols, A.L., 2016. Table of Radionuclides (Vol. 8). Monographie BIPM-5 8.

Beattie, B.J., Pentlow, K.S., O'Donoghue, J., Humm, J.L., 2014. A recommendation for revised dose calibrator measurement procedures for ^{89}Zr and ^{124}I. PLoS One 9, e106868.

BIPM, 2006. Le Système international d'unités in: Mètre, O.I.d.l.C.d. (Ed.), The International System of Units, 8 ed. BIPM, Paris.

BIPM, IEC, IFCC, ISO, IUPAC, IUPAP, OIML, 2008. Evaluation of measurement data - Guide to the expression of uncertainty in measurement, in: Metrology, W.G.o.t.J.C.f.G.i. (Ed.), JCGM 100:2008. BIPM, Online.

Börjesson, P.K.E., Jauw, Y.W.S., Boellaard, R., de Bree, R., Comans, E.F.I., Roos, J.C., Castelijns, J.A., Vosjan, M.J.W.D., Kummer, J.A., Leemans, C.R., Lammertsma, A.A., van Dongen, G.A.M.S., 2006. Performance of Immuno–Positron Emission Tomography with Zirconium-89-Labeled Chimeric Monoclonal Antibody U36 in the Detection of Lymph Node Metastases in Head and Neck Cancer Patients. Clinical Cancer Research 12, 2133-2140.

Bradshaw, T.J., Voorbach, M.J., Reuter, D.R., Giamis, A.M., Mudd, S.R., Beaver, J.D., 2016. Image quality of Zr-89 PET imaging in the Siemens microPET Focus 220 preclinical scanner. Mol Imaging Biol 18, 377-385.

Broda, R., 2003. A review of the triple-to-double coincidence ratio (TDCR) method for standardizing radionuclides. Appl Radiat Isotopes 58, 585-594.

Capintec, I., 2009. CRC®-25R Owners manual, in: Capintec, I. (Ed.), Rev. C ed. Capintec, Ramsey, NJ.

Cassette, P., Ahn, G.H., Alzitzoglou, T., Aubineau-Lanièce, I., Bochud, F., Garcia Torano, E., Grau Carles, A., Grau Malonda, A., Kossert, K., Lee, K.B., Laedermann, J.P., Simpson, B.R.S.,

van Wyngaardt, W.M., Zimmerman, B.E., 2006. Comparison of calculated spectra for the interaction of photons in a liquid scintillator. Example of ^{54}Mn 835 keV emission. Appl Radiat Isotopes 64, 1471-1480.

Chai, B., Ji, Y., 2003. LUTETIUM YTTRIUM ORTHOSILICATE SINGLE CRYSTAL SCINTILLATOR DETECTOR, in: Office, U.P. (Ed.), STARS - University of Central Florida, GOlT 1/202; C09K 11/08 ed. University of Central Florida, USA.

Collins, S., Keightley, J., Ivanov, P., Arinc, A., Fenwick, A., Pearce, A., 2019a. The potential radio-immunotherapeutic α-emitter ^{227}Th–part II: Absolute γ-ray emission intensities from the excited levels of ^{223}Ra. Appl Radiat Isotopes 145, 251-257.

Collins, S.M., Keightley, J.D., Ivanov, P., Arinc, A., Fenwick, A.J., Pearce, A.K., 2019b. The potential radio-immunotherapeutic α-emitter 227Th – part II: Absolute γ-ray emission intensities from the excited levels of 223Ra. Appl Radiat Isotopes 145, 251-257.

Collins, S.M., Pearce, A.K., Ferreira, K.M., Fenwick, A.J., Regan, P.H., Keightley, J.D., 2015. Direct measurement of the half-life of 223Ra. Appl Radiat Isotopes 99, 46-53.

Currie, L.A., 1968. Limits for qualitative detection and quantitative determination. Application to radiochemistry. Analytical Chemistry 40, 586-593.

D'Arienzo, M., 2013. Emission of β+ Particles Via Internal Pair Production in the 0+ – 0+ Transition of 90Zr: Historical Background and Current Applications in Nuclear Medicine Imaging. Atoms 1, 2-12.

Dejesus, O.T., Nickles, R.J., 1990. Production and purification of ^{89}Zr, a potential PET antibody label. International Journal of Radiation Applications and Instrumentation. Part A. Applied Radiation and Isotopes 41, 789-790.

Deri, M.A., Zeglis, B.M., Francesconi, L.C., Lewis, J.S., 2013. PET imaging with ^{89}Zr: From radiochemistry to the clinic. Nuclear Medicine and Biology 40, 3-14.

Dunworth, J.V., 1940. The Application of the Method of Coincidence Counting to Experiments in Nuclear Physics. Review of Scientific Instruments 11, 167.

Eckerman, K.F., Westfall, R.J., Ryman, J.C., Cristy, M., 1994. Availability of Nuclear Decay Data in Electronic Form, Including Beta Spectra not Previously Published. Health Phys 67, 338-345.

Fenwick, A.J., Collins, S.M., Evans, W.D., Ferreira, K.M., Paisey, S.J., Robinson, A.P., Marshall, C., 2020. Absolute Standardisation and Determination of the Half-life and Gamma Emission Intensities of ^{89}Zr. Appl Radiat Isot.

Gadd, R., Baker, M., Nijran, K.S., Owens, S., Thomson, W., Woods, M.J., Zananiri, F., 2006. Measurment Good Practice Guide No. 93: Protocol for Establishing and Maintaining the Calibration of Medical Radionuclide Calibrators and their Quality Control. National Physical Laboratory

Gaitanis, A., Kastis, G.A., Vlastou, E., Bouziotis, P., Verginis, P., Anagnostopoulos, C.D., 2017. Investigation of Image Reconstruction Parameters of the Mediso nanoScan PC Small-Animal PET/CT Scanner for Two Different Positron Emitters Under NEMA NU 4-2008 Standards. Mol Imaging Biol 19, 550-559.

Garcia-Torano, E., Peyres, V., Roteta, M., Mejuto, M., Sanchez-Cabezudo, A., Romero, E., 2018. Standardisation and half-life of ^{89}Zr. Appl Radiat Isot 134, 421-425.

Garcia-Torano, E., Romero, E.S., Ortega, A.M., 2019. Determination of activity meter settings for the PET nuclides ^{44}Sc and ^{89}Zr. Appl Radiat Isot 153, 108829.

Gunther, E., 2002. Determination of the activity of radionuclidic sources emitting beta and gamma radiation using the CIEMAT/NIST method. LSC 2001, Advances in Liquid Scintillation Spectrometry.

Hoegl, A., Schwerdtel, E., 1963. Gerat zum Messen der Aktivitat niederenergetischer Betastrahler in einem flussigen Szintillator, FRG patent.

Hohn, A., Zimmermann, K., Schaub, E., Hirzel, W., Schubiger, P.A., Schibli, R., 2008. Production and separation of "non-standard" PET nuclides at a large cyclotron facility: the experiences at the Paul Scherrer Institute in Switzerland. The Quarterly Journal of Nuclear Medicine and Molecular Imaging 52, 145-150.

Howe, D.A., Langer, L.M., Wortman, D., 1962. Search for a 92+ level at 1.5 MeV in ^{89}Y. Nuclear Physics 37, 476-481.

Hyde, E.K., O'Kelley, G.D., 1951. Radiochemical and Spectrometer Studies of Several Neutron-Deficient Zirconium Isotopes and Their Decay Products. Physical Review 82, 944-951.

ISO, 2010. Injection equipment for medical use -- Part 1: Ampoules for injectables, ISO 9187-1:2010.

Ivanov, P.I., Jerome, S.M., Bozhikov, G.A., Maslov, O.D., Starodub, G.Y., Dmitriev, S.N., 2014. Cyclotron production and radiochemical purification of ^{88,89}Zr via α-particle induced reactions on natural strontium. Appl Radiat Isotopes 90, 261-264.

Kaalep, A., Huisman, M., Sera, T., Vugts, D., Boellaard, R., on behalf of, E., Eatris, the, T.C., 2018a. Feasibility of PET/CT system performance harmonisation for quantitative multicentre 89Zr studies. EJNMMI Physics 5, 26.

Kaalep, A., Sera, T., Oyen, W., Krause, B.J., Chiti, A., Liu, Y., Boellaard, R., 2018b. EANM/EARL FDG-PET/CT accreditation - summary results from the first 200 accredited imaging systems. Eur J Nucl Med Mol I 45, 412-422.

Katz, L., Baker, R.G., Montalbetti, R., 1953. The Photoneutron Cross Sections of ^{87}Rb, ^{90}Zr, and ^{92}Mo. Canadian Journal of Physics 31, 250-261.

Keightley, J.D., Park, T.S., 2007. Digital coincidence counting for radionuclide standardization. Metrologia 44, S32-S35.

Keightley, J.D., Watt, G.C., 2002. Digital coincidence counting (DCC) and its use in the corrections for out-of-channel events in 4(pi)(beta)-(gamma) coincidence counting. Appl Radiat Isotopes 56, 205-210.

Knoll, G.F., 2010. Radiation Detection and Measurement, 4th Edition, 4 ed. Wiley.

Kossert, K., Carles, A.G., 2010. Improved method for the calculation of the counting efficiency of electron-capture nuclides in liquid scintillation samples. Appl Radiat Isot 68, 1482-1488.

Lambregts, D.M., Beets, G.L., Maas, M., Curvo-Semedo, L., Kessels, A.G., Thywissen, T., Beets-Tan, R.G., 2011. Tumour ADC measurements in rectal cancer: effect of ROI methods on ADC values and interobserver variability. Eur Radiol 21, 2567-2574.

Lebeda, O., Štursa, J., Ráliš, J., 2015. Experimental cross-sections of deuteron-induced reaction on 89Y up to 20MeV; comparison of natTi(d,x)48V and 27Al(d,x)24Na monitor reactions. Nuclear Instruments and Methods in Physics Research Section B: Beam Interactions with Materials and Atoms 360, 118-128.

Levin, S.G., Young, R.W., Stohler, R.L., 1992. Estimation of median human lethal radiation dose computed from data on occupants of reinforced concrete structures in Nagasaki, Japan. Health Phys 63, 522-531.

Link, J.M., Krohn, K.A., Eary, J.F., Kishore, R., Lewellen, T.K., Johnson, M.W., Badger, C.C., Richter, K.Y., Nelp, W.B., 1986. 89Zr for antibody labeling and positron emission tomography. Journal of Labelled Compounds and Radiopharmaceuticals 23, 1297-1298.

Malonda, A.G., 2001. A Description of the CIEMAT/NIST Method. LNHB.

Malonda, A.G., Garcia-Toraño, E., 1982. Evaluation of counting efficiency in liquid scintillation counting of pure β-ray emitters. The International Journal of Applied Radiation and Isotopes 33, 249-253.

McKnight, B.N., Viola-Villegas, N.T., 2018. ^{89}Zr-ImmunoPET companion diagnostics and their impact in clinical drug development. J Labelled Comp Radiopharm 61, 727-738.

Mediso, 2016. Quality Control Guide: nanoScan®PET Subsystem v1.6, v1.6 ed. Mediso Medical Imaging Systems, p. 15.

Meijs, W.E., Herscheid, J.D.M., Haisma, H.J., Wijbrandts, R., van Langevelde, F., Van Leuffen, P.J., Mooy, R., Pinedo, H.M., 1994. Production of highly pure no-carrier added 89Zr for the labelling of antibodies with a positron emitter. Appl Radiat Isotopes 45, 1143-1147.

MHRA, 2002. Medical Devices Regulations 2002 (UK MDR 2002), SI 2002 No 618, as amended. UK Government.

Michotte, C., Nonis, M., Alekseev, I.V., Kharitonov, I.A., Tereshchenko, E.E., Zanevskiy, A.V., Keightley, J.D., Fenwick, A., Ferreira, K., Johansson, L., Capogni, M., Carconi, P., Fazio, A., De Felice, P., 2016. Comparison of ^{18}F activity measurements at the VNIIM, NPL and the ENEA-INMRI using the SIRTI of the BIPM. Appl Radiat Isotopes 109, 17-23.

Michotte, C., Nonis, M., Bergeron, D., Cessna, J., Fitzgerald, R., Pibida, L., Zimmerman, B., Fenwick, A., Ferreira, K., Keightley, J., 2017a. Activity measurements of the radionuclides 18F and 64Cu for the NIST, USA in the ongoing comparisons BIPM. RI (II)-K4. F-18 and BIPM. RI (II)-K4. Cu-64. Metrologia 54.

Michotte, C., Nonis, M., Bergeron, D., Cessna, J., Fitzgerald, R., Pibida, L., Zimmerman, B., Fenwick, A., Ferreira, K., Keightley, J., Da Silva, I., 2017b. Activity measurements of the radionuclides ^{18}F and ^{64}Cu for the NIST, USA in the ongoing comparisons BIPM.RI(II)-K4.F-18 and BIPM.RI(II)-K4.Cu-64. Metrologia 54, https://doi.org/10.1088/0026-1394/1054/1081a/06011.

Michotte, C., Nonis, M., Rooy, M.W.V., Staden, M.J.V., Lubbe, J., 2017c. Activity measurements of the radionuclides 18F and 99mTc for the NMISA, South Africa in the ongoing comparisons BIPM.RI(II)-K4.F-18 and BIPM.RI(II)-K4.Tc-99m. Metrologia 54, 06001.

NEMA, 2008. Performance measurements of small animal positron emission tomographs NEMA Standards Publication NU 4-2008. Rosslyn, VA: NEMA 23.

NEMA, 2012. NEMA standards publication NU 2-2012: performance measurements of positron emission tomographs. Rosslyn, VA: National Electrical Manufactures Association.

Nogueira, L., Brandão, S., Matos, E., Nunes, R.G., Ferreira, H.A., Loureiro, J., Ramos, I., 2015. Region of interest demarcation for quantification of the apparent diffusion coefficient in breast lesions and its interobserver variability. Diagn Interv Radiol 21, 123-127.

Pochwalski, K., Broda, R., Radoszewski, T., 1988. Standardization of pure beta emitters by liquid-scintillation counting. International Journal of Radiation Applications and Instrumentation. Part A. Applied Radiation and Isotopes 39, 165-172.

Pochwalski, K., Radoszewski, T., 1979. Disintegration rate determination by liquid scintillation counting using the triple to double coincidence ratio (TDCR) method. IBJ Report, INR 1848/OPiDI/E/A.

Pommé, S., Camps, J., Van Ammel, R., Paepen, J., 2008. Protocol for uncertainty assessment of half-lives. J Radioanal Nucl Chem 276, 335-339.

Pommé, S., Keightley, J., 2015. Determination of a reference value and its uncertainty through a power-moderated mean. Metrologia 52, S200-S212.

Putman, J., Siegbahn, K., 1955. Chapter 26: Beta-and Gamma-Ray Spectroscopy. Interscience, New York.

Ratel, G., 2007. The Systeme International de Reference and its application in key comparisons. Metrologia 44, S7-S16.

Rusjan, P., Mamo, D., Ginovart, N., Hussey, D., Vitcu, I., Yasuno, F., Tetsuya, S., Houle, S., Kapur, S., 2006. An automated method for the extraction of regional data from PET images. Psychiatry Research: Neuroimaging 147, 79-89.

Rytz, A., 1978. International Coherence of Activity Measurements. Environment International 1, 15-18.

Rytz, A., 1983. Tne International Reference System For Activity Measurements of γ-ray Emitting Nuclides. Appl Radiat Isot 34, 1047-1056.

Sagane, R., Kojima, S., Miyamoto, G., Ikawa, M., 1938. Preliminary Report on the Radioactivity Produced in Y, Zr, and Mo. Physical Review 54, 542-543.

Sagane, R., Kojima, S., Miyamoto, G., Ikawa, M., 1940. Artificial Radioactivity Induced in Zr and Mo. Physical Review 57, 1179-1180.

Sahagia, M., Luca, A., Antohe, A., Ioan, M.-R., 2019. Standardization of the emerging medical positron emitter ^{89}Zr. J Radioanal Nucl Chem, 1-7.

Schaefer, A., Vermandel, M., Baillet, C., Dewalle-Vignion, A.S., Modzelewski, R., Vera, P., Massoptier, L., Parcq, C., Gibon, D., Fechter, T., Nemer, U., Gardin, I., Nestle, U., 2016. Impact of consensus contours from multiple PET segmentation methods on the accuracy of functional volume delineation. Eur J Nucl Med Mol Imaging 43, 911-924.

Schönfeld, E., Janßen, H., 2000. Calculation of emission probabilities of X-rays and Auger electrons emitted in radioactive disintegration processes. Appl Radiat Isotopes 52, 595-600.

Schwarz, S.W., Decristoforo, C., 2019. US and EU radiopharmaceutical diagnostic and therapeutic nonclinical study requirements for clinical trials authorizations and marketing authorizations. EJNMMI Radiopharm Chem 4, 10-10.

Selwyn, R.G., Nickles, R.J., Thomadsen, B.R., DeWerd, L.A., Micka, J.A., 2007. A new internal pair production branching ratio of 90Y: The development of a non-destructive assay for 90Y and 90Sr. Appl Radiat Isotopes 65, 318-327.

Shure, K., Deutsch, M., 1951. Radiations from ^{89}Zr. Physical Review 82, 122-122.

Singh, B., 2013. Nuclear Data Sheets for A = 89. Nuclear Data Sheets 114, 1-208.

Smith, D., 1975. An Improved Method of Data Collection for 4(pi)(beta)-(gamma) Coincidence Measurements. Metrologia 11, 73-77.

Smith, D., 1987. Some developments in the Cox-Isham theory of coincidence corrections, including the extension to the computer-discrimination method. International Journal of Radiation Applications and Instrumentation. Part A. Applied Radiation and Isotopes 38, 813-821.

Smith, D., Chen, Y., 1985. The 4pb coincidence method for parent-daughter decay in non-equilibrium: the measurement of the disintegration rates of 47Ca-47Sc, 45Ca. Nuclear Instruments and Methods A 236, 321-329.

Svensson, C., 2008. Production of ^{89}Zr for labelling of antibodies to be evaluated preclinically with micro-PET for radioimmunodiagnostics of prostate cancer. Lund.

TELIX, 2021. First U.S. Patients Dosed in Phase III ZIRCON Trial of Renal Cancer Imaging Product. TELIX, Online, p. ZIRCON trial.

Thielemans, K., Tsoumpas, C., Mustafovic, S., Beisel, T., Aguiar, P., Dikaios, N., Jacobson, M.W., 2012a. STIR: software for tomographic image reconstruction release 2. Physics in Medicine and Biology 57, 867-883.

Thielemans, K., Tsoumpas, C., Mustafovic, S., Beisel, T., Aguiar, P., Dikaios, N., Jacobson, M.W., 2012b. STIR: software for tomographic image reconstruction release 2. Physics in Medicine & Biology 57, 867.

Tsoulfanidis, N., Landsberger, S., 2015. Measurement and Detection of Radiation, Fourth Edition, 4 ed. CRC Press, Taylor and Francis Group Oakville.

USDoH, U.S.D.o.H.a.H.S., 2014. Guidance for Industry and FDA Staff, Qualification Process for Drug Development Tools. Center for Drug Evaluation and Research (CDER), Silver Spring, MD.

Van Patter, D.M., Shafroth, S.M., 1964. Decay of 78.4 h Zr-89 and 4.18 min Zr-89m. Nuclear Physics 50, 113-135.

Verel, I., Visser, G.W.M., Boellaard, R., Stigter-van Walsum, M., Snow, G.B., van Dongen, G.A.M.S., 2003. ^{89}Zr Immuno-PET: Comprehensive Procedures for the Production of ^{89}Zr-Labeled Monoclonal Antibodies. Journal of Nuclear Medicine 44, 1271-1281.

Wooten, A.L., Lewis, B.C., Szatkowski, D.J., Sultan, D.H., Abdin, K.I., Voller, T.F., Liu, Y., Lapi, S.E., 2016. Calibration setting numbers for dose calibrators for the PET isotopes ^{52}Mn, ^{64}Cu, ^{76}Br, ^{86}Y, ^{89}Zr, ^{124}I. Appl Radiat Isotopes 113, 89-95.

Zanzonico, P., 2008. Routine quality control of clinical nuclear medicine instrumentation: a brief review. Journal of nuclear medicine : official publication, Society of Nuclear Medicine 49, 1114-1131.

Zimmerman, B.E., Judge, S., 2007. Traceability in nuclear medicine. Metrologia 44, S127.

Appendix 1: MICELLE2 input files

In order to use the MICELLE2 Monte-Carlo programme, it is necessary to prepare input files relating to the decay chain of concern as described in (Kossert and Carles, 2010). The following pages show screenshots of the input files used.

```
                    'Zr89a'

''                  BASIC DATA

'Decay scheme (1-14)          :'        3
'Atomic data                  :'        'Y__ATOM.DAT'



''                  EC DECAY

'PK,PL1,PL2,PM+               :'          0.8575,
0.1165,0.00,0.026 | EC01
''                  BETA DECAY

'Endpoint energy                    ='             0.
'Mass number                        ='             0.
'Daughter nucl. atomic number       ='             0.
'Forbiddenness                      ='             0
'Shape factor coefficients          ='          0.,0.,0.
''                  GAMMA TRANSITIONS

'PGAM,EGAM (1)                :'        1.,1713.1
| Ga01, no ICCs
'PIK,PIL1,PIL2,PIL3,PIM (1)   :'        0.0,0.0,0.0,0.0,0.0
'PGAM,EGAM (2)                :'        0.,0.0
'PIK,PIL1,PIL2,PIL3,PIM (2)   :'        0.0,0.0,0.0,0.0,0.0
'PGAM,EGAM (3)                :'        0.0,0.0
'PIK,PIL1,PIL2,PIL3,PIM (3)   :'        0.0,0.0,0.0,0.0,0.0



----
DECAY SCHEME
      1    PURE EC
      3    EC-IC/GAMMA
      5    IC/GAMMA
      6    EC-IC/GAMMA-IC/GAMMA
      7    IC/GAMMA-IC/GAMMA
      8    BETA-IC/GAMMA
      9    BETA-IC/GAMMA-IC/GAMMA
     10    PURE BETA
     11    EC-IC/GAMMA-IC/GAMMA-IC/GAMMA
     12    IC/GAMMA-IC/GAMMA-IC/GAMMA
     13    PURE BETA+
     14    BETA+-IC/GAMMA
```

Data figure 1: Input data for decay pathway 'A'

```
                    'Zr89b'

''                  BASIC DATA

'Decay scheme (1-14)          :'        3
'Atomic data                  :'        'Y__ATOM.DAT'


''                  EC DECAY

'PK,PL1,PL2,PM+               :'          0.8615,
0.1134,0.00,0.0251      | EC02
''                  BETA DECAY

'Endpoint energy                    ='              0.
'Mass number                        ='              0.
'Daughter nucl. atomic number       ='              0.
'Forbiddenness                      ='              0
'Shape factor coefficients          ='          0.,0.,0.
''                  GAMMA TRANSITIONS

'PGAM,EGAM (1)                :'        1.,1657.58
| Ga02, no ICCs
'PIK,PIL1,PIL2,PIL3,PIM (1)   :'        0.0,0.0,0.0,0.0,0.0
'PGAM,EGAM (2)                :'        0.,0.0
'PIK,PIL1,PIL2,PIL3,PIM (2)   :'        0.0,0.0,0.0,0.0,0.0
'PGAM,EGAM (3)                :'        0.0,0.0
'PIK,PIL1,PIL2,PIL3,PIM (3)   :'        0.0,0.0,0.0,0.0,0.0


----
DECAY SCHEME
       1    PURE EC
       3    EC-IC/GAMMA
       5    IC/GAMMA
       6    EC-IC/GAMMA-IC/GAMMA
       7    IC/GAMMA-IC/GAMMA
       8    BETA-IC/GAMMA
       9    BETA-IC/GAMMA-IC/GAMMA
      10    PURE BETA
      11    EC-IC/GAMMA-IC/GAMMA-IC/GAMMA
      12    IC/GAMMA-IC/GAMMA-IC/GAMMA
      13    PURE BETA+
      14    BETA+-IC/GAMMA
```

Data figure 2: Input data for decay pathway 'B'

```
                    'Zr89c'

''                  BASIC DATA

'Decay scheme (1-14)        :'        3
'Atomic data                :'        'Y__ATOM.DAT'



''                  EC DECAY

'PK,PL1,PL2,PM+             :'          0.8632,
0.1120,0.00,0.0248    | EC03
''                  BETA DECAY

'Endpoint energy                    ='              0.
'Mass number                        ='              0.
'Daughter nucl. atomic number       ='              0.
'Forbiddenness                      ='              0
'Shape factor coefficients          ='          0.,0.,0.
''                  GAMMA TRANSITIONS

'PGAM,EGAM (1)              :'        1.,1620.83
| Ga03, no ICCs
'PIK,PIL1,PIL2,PIL3,PIM (1) :'        0.0,0.0,0.0,0.0,0.0
'PGAM,EGAM (2)              :'        0.,0.0
'PIK,PIL1,PIL2,PIL3,PIM (2) :'        0.0,0.0,0.0,0.0,0.0
'PGAM,EGAM (3)              :'        0.0,0.0
'PIK,PIL1,PIL2,PIL3,PIM (3) :'        0.0,0.0,0.0,0.0,0.0



----
DECAY SCHEME
      1    PURE EC
      3    EC-IC/GAMMA
      5    IC/GAMMA
      6    EC-IC/GAMMA-IC/GAMMA
      7    IC/GAMMA-IC/GAMMA
      8    BETA-IC/GAMMA
      9    BETA-IC/GAMMA-IC/GAMMA
     10    PURE BETA
     11    EC-IC/GAMMA-IC/GAMMA-IC/GAMMA
     12    IC/GAMMA-IC/GAMMA-IC/GAMMA
     13    PURE BETA+
     14    BETA+-IC/GAMMA
```

Data figure 3: Input data for decay pathway 'C'

```
                    'Zr89d'

''                BASIC DATA

'Decay scheme (1-14)        :'        1
'Atomic data                :'        'Y__ATOM.DAT'



''                EC DECAY

'PK,PL1,PL2,PM+             :'          0.8731,
0.1041,0.00,0.0228   | EC05
''                BETA DECAY

'Endpoint energy                  ='             0.
'Mass number                      ='             0.
'Daughter nucl. atomic number     ='             0.
'Forbiddenness                    ='             0
'Shape factor coefficients        ='          0.,0.,0.
''                GAMMA TRANSITIONS

'PGAM,EGAM (1)              :'        1.,0.
'PIK,PIL1,PIL2,PIL3,PIM (1) :'        0.0,0.0,0.0,0.0,0.0
'PGAM,EGAM (2)              :'        0.,0.0
'PIK,PIL1,PIL2,PIL3,PIM (2) :'        0.0,0.0,0.0,0.0,0.0
'PGAM,EGAM (3)              :'        0.0,0.0
'PIK,PIL1,PIL2,PIL3,PIM (3) :'        0.0,0.0,0.0,0.0,0.0



----
DECAY SCHEME
       1    PURE EC
       3    EC-IC/GAMMA
       5    IC/GAMMA
       6    EC-IC/GAMMA-IC/GAMMA
       7    IC/GAMMA-IC/GAMMA
       8    BETA-IC/GAMMA
       9    BETA-IC/GAMMA-IC/GAMMA
      10    PURE BETA
      11    EC-IC/GAMMA-IC/GAMMA-IC/GAMMA
      12    IC/GAMMA-IC/GAMMA-IC/GAMMA
      13    PURE BETA+
      14    BETA+-IC/GAMMA
```

Data figure 4: Input data for decay pathway 'D'

```
                    'Zr89e'

''                BASIC DATA

'Decay scheme (1-14)        :'        13
'Atomic data                :'        'Y__ATOM.DAT'



''                EC DECAY

'PK,PL1,PL2,PM+             :'          0., 0.,0.,0.
''                BETA DECAY

'Endpoint energy                    ='            902.
'Mass number                        ='             89.
'Daughter nucl. atomic number       ='             39.
'Forbiddenness                      ='              0
'Shape factor coefficients          ='          0.,0.,0.
''                GAMMA TRANSITIONS

'PGAM,EGAM (1)              :'        1.,0.0
'PIK,PIL1,PIL2,PIL3,PIM (1) :'        0.0,0.0,0.0,0.0,0.0
'PGAM,EGAM (2)              :'        0.,0.0
'PIK,PIL1,PIL2,PIL3,PIM (2) :'        0.0,0.0,0.0,0.0,0.0
'PGAM,EGAM (3)              :'        0.0,0.0
'PIK,PIL1,PIL2,PIL3,PIM (3) :'        0.0,0.0,0.0,0.0,0.0



----
DECAY SCHEME
       1    PURE EC
       3    EC-IC/GAMMA
       5    IC/GAMMA
       6    EC-IC/GAMMA-IC/GAMMA
       7    IC/GAMMA-IC/GAMMA
       8    BETA-IC/GAMMA
       9    BETA-IC/GAMMA-IC/GAMMA
      10    PURE BETA
      11    EC-IC/GAMMA-IC/GAMMA-IC/GAMMA
      12    IC/GAMMA-IC/GAMMA-IC/GAMMA
      13    PURE BETA+
      14    BETA+-IC/GAMMA
```

Data figure 5: Input data for decay pathway 'E'

```
                    'Zr89f'

''                  BASIC DATA

'Decay scheme (1-14)          :'        3
'Atomic data                  :'        'Y__ATOM.DAT'



''                  EC DECAY

'PK,PL1,PL2,PM+               :'          0.8677,
0.1082,0.00,0.0241        | EC04
''                  BETA DECAY

'Endpoint energy                    ='             0.
'Mass number                        ='             0.
'Daughter nucl. atomic number       ='             0.
'Forbiddenness                      ='             0
'Shape factor coefficients          ='          0.,0.,0.
''                  GAMMA TRANSITIONS

'PGAM,EGAM (1)                :'         0.9996,1744.74
| Ga04
'PIK,PIL1,PIL2,PIL3,PIM (1) :'
0.4508,0.0474,0.0006,0.0007,0.5005
'PGAM,EGAM (2)                :'         0.,0.0
'PIK,PIL1,PIL2,PIL3,PIM (2) :'         0.0,0.0,0.0,0.0,0.0
'PGAM,EGAM (3)                :'         0.0,0.0
'PIK,PIL1,PIL2,PIL3,PIM (3) :'         0.0,0.0,0.0,0.0,0.0



----
DECAY SCHEME
       1    PURE EC
       3    EC-IC/GAMMA
       5    IC/GAMMA
       6    EC-IC/GAMMA-IC/GAMMA
       7    IC/GAMMA-IC/GAMMA
       8    BETA-IC/GAMMA
       9    BETA-IC/GAMMA-IC/GAMMA
      10    PURE BETA
      11    EC-IC/GAMMA-IC/GAMMA-IC/GAMMA
      12    IC/GAMMA-IC/GAMMA-IC/GAMMA
      13    PURE BETA+
      14    BETA+-IC/GAMMA
```

Data figure 6: Input data for decay pathway 'F'

```
''                    CONTROL DATA
'DECAY EVENTS (1-20000) KK: 210000                :'
5000
'R,H,NSUC                                         :'
1.25,3.158,5000
'FIN,FFIN,DINC                                    :'
0.1,4.0,0.025
'SCINTILLATOR (1-5)                               :'
5
'IONIZATION QUENCHING (1-4) 6=KK,75               :'
4
'LARKINS CORRECTION (1=YES,2)                     :'
2
'TDCR (1,2)                                       :'
1
'CIEMAT/NIST                                      :'
'ADD.COMP. (1) / NO (2)  (fuer Gamma-WW)          :'
1
'SPECTRUM 100 CH (1) / 2000 CH (2)                :'
2
'MICELLE CORRECTION (1=YES,2)                     :'
2
'SPH. RAD. (0.2 nm-1 mm)                          :'
2.0
'CENT. SOURCE(1) / RADOMLY DIST.(2)               :'
2
'AV. DSB COMPUTATION (1,2)                    :'          1
'AV. SSB FOR I-125 IN THE T&B STRANDS             :'
3.7,1.5
'AV. SSB FOR I-125 IN UNIFORM DNA (ssb Da/eV)     :'
16.67

----
DECAY SCHEME
      1    PURE EC
      2    EC-GAMMA
      3    EC-IC/GAMMA
      4    NON COINCIDENT EC-IC/GAMMA
      5    IC/GAMMA
      6    EC-IC/GAMMA-IC/GAMMA
      7    IC/GAMMA-IC/GAMMA
      8    BETA-IC/GAMMA
      9    BETA-IC/GAMMA-IC/GAMMA
     10    PURE BETA
     11    EC-IC/GAMMA-IC/GAMMA-IC/GAMMA
     12    IC/GAMMA-IC/GAMMA-IC/GAMMA

SCINTILLATOR
      1    TOLUENE
      2    INSTAGEL
      3    HISAFE II
      4    DIOXANE-NAPHTHALENE
      5    ULTIMAGOLD

IONIZATION QUENCHING
      1    OLD Q(E) EXPRESSION CPC 23(1981)385
      2    POLYNOMIAL QUOTIENT
      3    STOPPING POWER FROM TABLE STO.DAT         [STP.DAT]
      4    STOPPING POWER FROM FUNCTION STOL(T)
[SCINTI.DAT]

CIEMAT/NIST METHOD
      1    YES
           With additional components
[EFFCOMP.DAT]
      2    NO
MICELLE CORRECTION
      1    YES
      2    NO
      SOURCE
            1    Centered sources
[MICELLE_C.DAT]
            2    Randomly distributed sources
[MICELLE_R.DAT]
```

Data figure 7: Example of 'Control' file used to vary parameters during the simulation. The values in this file were adjusted as appropriate during the work.

```
'Additional components into the scintillator'
'Number of extra components          :'       4
'Efficiency for H-3                  :'       0.500
'                 Percent    Num.    d (gcm-3)       Comp.'
'                 -------    ---     ---------     --------'
'CCl4'                .0     2        1.59
                                                    'C'  1
                                                    'Cl' 4
'H2O'               2.91  2          1.000
                                                    'H'  2
                                                    'O'  1
'CH3NO2'              .0     4        1.14
                                                    'C'  1
                                                    'H'  3
                                                    'N'  1
                                                    'O'  2
'HCl'               0.0036  2         1.000
                                                    'H'  1
                                                    'Cl' 1
```

Data figure 8: Datafile showing adjustments to elemental composition of scintillator

```
   'UGAB TX'     5           0.0075       .9800
' '
' ' ATOM      NUM     Z         A      EXCITATION ENERGY
' ' ----      ---    ---       ---     ----------------
    'C'      18.66   6.      12.001          7.8E-5
    'H'      28.25   1.       1.0079         1.92E-5
    'O'       2.53   8.      15.9993         9.5E-5
    'P'       0.01  15.      30.9737        17.3E-5
    'N'       0.02   7.      14.0067         8.2E-5
' '
```

Data figure 9: Extract from liquid scintillation composition datafile

The following pages contain the yttrium atomic data file required for the simulation:

```
'Atomic number (daughter)   :'        39
'WK,WL1,WL2,WL3             :'      0.710, 0.006, 0.026, 0.028
'F12,F13,F23                :'      0.260, 0.520, 0.126

'PKL1L1,L2,L3,M1,M2,M3,M4,M5:'
0.0695,0.0786,0.1238,0.0216,0.0125,0.0197,0.0010,0.0013
'PKL1N1,N2,N3,O1,O2,O3      :'
0.0034,0.0017,0.0026,0.0000,0.0000,0.0000
'PKL2L2,L3,M1,M2,M3,M4,M5   :'
0.0128,0.2869,0.0102,0.0037,0.0385,0.0013,0.0047
'PKL2N1,N2,N3,N5,O1,O3      :'
0.0016,0.0005,0.0049,0.0000,0.0000,0.0000
'PKL3L3,M1,M2,M3,M4,M5      :'
0.1545,0.0165,0.0393,0.0431,0.0058,0.0059
'PKL3N1,N2,N3,N4,N5,O1,O2,O3:'
0.0026,0.0054,0.0060,0.0002,0.0000,0.0001,0.0000,0.0000
'PKM1M1,M2,M3,N1,N2,N3      :'
0.0017,0.0017,0.0027,0.0006,0.0002,0.0004
'PKM2M3,N1,N2               :'     0.0054,0.0003,0.0007
'PKM3M3,M4,M5,N1,N2,N3      :'
0.0030,0.0006,0.0006,0.0004,0.0008,0.0008

'PL1L2M1,M2,M3,M4,M5        :'
0.0000,0.0000,0.0000,0.1700,0.4730
'PL1L2N1..N7,O1..O6,P1..P3  :'
0.1409,0.0826,0.1088,0.0117,0.0000,0.0000,0.0000,0.0130,0.0000,0.00
00,0.0000,0.0000,0.0000,0.0000,0.0000,0.0000,0.0000
'PL1L3M1,M2,M3,M4,M5        :'
0.0000,0.0000,0.0779,0.3381,0.4936
'PL1L3N1..N7,O1..O7,P1..P3  :'
0.0375,0.0145,0.0303,0.0067,0.0000,0.0000,0.0000,0.0013,0.0000,0.00
00,0.0000,0.0000,0.0000,0.0000,0.0000,0.0000,0.0000,0.0000

'PL1M1M1,M2,M3,M4,M5        :'
0.0386,0.0744,0.1424,0.1047,0.1530
'PL1M1N1..N7,O1..O5,P3      :'
0.0105,0.0097,0.0184,0.0030,0.0000,0.0000,0.0000,0.0010,0.0000,0.00
00,0.0000,0.0000,0.0000,0.0000
'PL1M2M3..M5,N1..N7,O1,O5   :'
0.0032,0.0020,0.0347,0.0085,0.0001,0.0000,0.0008,0.0034,0.0312
'PL1M3M3,M4,M5,N1,N2,N4,O1  :'
0.0000,0.0000,0.0221,0.0162,0.0007,0.0006,0.0015
'PL1M4M4,M5,N1..N7,O1,O5    :'
0.0048,0.2054,0.0116,0.0004,0.0039,0.0003,0.0000,0.0000,0.0000,0.00
10,0.0000
'PL1M5M5,N1..N7,O1..O5      :'
0.0574,0.0168,0.0042,0.0028,0.0047,0.0000,0.0000,0.0000,0.0016,0.00
00,0.0000,0.0000
'PL1N1N1,N2,N4,N2N4,O1,N4N4 :'
0.0007,0.0011,0.0021,0.0003,0.0000,0.0000,0.0000,0.0002,0.0000,0.00
00

'PL2L3M4,M5,N1..N7,O1..O5,P2:'
0.0000,0.0000,0.1467,0.4827,0.1885,0.1683,0.0000,0.0000,0.0000,0.01
38,0.0000,0.0000,0.0000,0.0000,0.0000
```

```
'PL2M1M1..M5,N2..N4,O2      :'
0.0020,0.0424,0.0037,0.0026,0.0059,0.0041,0.0004,0.0000,0.0000
'PL2M2M2,M3,M4,M5           :'     0.0397,0.1319,0.0657,0.1196
'PL2M2N1..N7,O1..O5,P2      :'
0.0067,0.0091,0.0167,0.0019,0.0000,0.0000,0.0000,0.0000,0.0000,0.00
00,0.0000,0.0000,0.0000
'PL2M3M3..M5,N1..N5,O2,O4   :'
0.0036,0.0795,0.0110,0.0005,0.0132,0.0008,0.0021,0.0000,0.0000,0.00
00
'PL2M4M4,M5,N1..N7,O2..O5   :'
0.0701,0.3089,0.0004,0.0066,0.0098,0.0036,0.0000,0.0000,0.0000,0.00
00,0.0000,0.0000,0.0000
'PL2M5M5,N2..N6,O2,O4       :'
0.0146,0.0110,0.0013,0.0072,0.0000,0.0000,0.0000,0.0000
'PL2N1N2,N2N2,N4,N4N4       :'
0.0007,0.0005,0.0017,0.0002,0.0000,0.0000,0.0000,0.0003,0.0000,0.00
00,0.0000

'PL3M1M1..M5,N3..N7,O3      :'
0.0021,0.0015,0.0420,0.0039,0.0044,0.0041,0.0000,0.0000,0.0000,0.00
00
'PL3M2M3..M5,N1,N3,N5,N7,O3 :'
0.0686,0.0044,0.0395,0.0068,0.0000,0.0000,0.0000
'PL3M3M3,M4,M5,N1           :'     0.0989,0.0914,0.1393,0.0066
'PL3M3N2,N4,O1,O2           :'
0.0086,0.0224,0.0025,0.0000,0.0000,0.0000,0.0000,0.0000,0.0000,0.00
00,0.0000
'PL3M4M4,M5,N1..N7,O3,O5    :'
0.0122,0.2387,0.0006,0.0006,0.0087,0.0006,0.0000,0.0000,0.0000,0.00
00,0.0000
'PL3M5M5,N1,N2,N4,O2        :'
0.1625,0.0007,0.0048,0.0144,0.0063,0.0000,0.0000,0.0000,0.0000,0.00
00,0.0000,0.0000
'PL3N1N3,N2N3,N5,N3N4,N5,.. :'
0.0007,0.0009,0.0000,0.0013,0.0003,0.0000,0.0000,0.0000,0.0000,0.00
00,0.0000,0.0000,0.0000,0.0000

'PM1M2M4..,PM1M3..          :'
0.0000,0.0000,0.0727,0.0655,0.1523,0.0053,0.0063,0.0000,0.0000,0.00
00,0.0000,0.0000,0.0000,0.0000,0.1397,0.1335,0.2484,0.0050,0.0090,0
.0000,0.0118,0.0000,0.0000
'PM1M4M4..,PM1M5..          :'
0.0156,0.0108,0.0000,0.0000,0.0000,0.0000,0.0258,0.0766,0.0182,0.00
13,0.0023,0.0000,0.0000,0.0000,0.0000,0.0000,0.0000

'PM2M3N4..,PM2M4..          :'
0.0035,0.0086,0.0000,0.0081,0.0000,0.0000,0.0000,0.0000,0.0327,0.12
25,0.1080,0.1405,0.2401,0.0043,0.0041,0.0000,0.0135,0.0000,0.0000,0
.0000,0.0000
'PM2M5M5..                  :'
0.0258,0.0222,0.1919,0.0261,0.0016,0.0011,0.0000,0.0017,0.0000,0.00
87,0.0064,0.0220,0.0024,0.0041,0.0000,0.0000,0.0000

'PM3M4M4..                  :'
0.0079,0.0986,0.0304,0.0221,0.1175,0.0016,0.0013,0.0000,0.0032
'PM3M5M5..,PM3N1            :'
0.0796,0.1311,0.1335,0.2963,0.0028,0.0078,0.0000,0.0169,0.0000,0.00
```

```
00,0.0000,0.0000,0.0109,0.0103,0.0203,0.0033,0.0000,0.0000,0.0046,0
.0000,0.0000
'PM4M5N6..,PM4N1..,PM4N2..  :'
0.0000,0.0000,0.0000,0.0000,0.0335,0.1520,0.1962,0.1020,0.0201,0.00
00,0.0248,0.1282,0.0700,0.0081
'PM4N3N3..,PM4N4..          :'
0.0542,0.1672,0.0089,0.0000,0.0000,0.0094,0.0220,0.0000,0.0000,0.00
00,0.0000,0.0000,0.0000,0.0035,0.0000,0.0000,0.0000,0.0000,0.0000

'PM5N1N1..                  :'
0.0339,0.0931,0.2588,0.0136,0.1098,0.0000,0.1030,0.0878,0.1012,0.00
92,0.1575,0.0000,0.0000,0.0014,0.0163,0.0000,0.0000,0.0146,0.0000,0
.0000,0.0000,0.0000,0.0000,0.0000,0.0000,0.0000,0.0000

'PN1..                      :'
0.0000,0.0000,0.0000,0.0000,0.0000,0.0000,0.0000,0.0000,0.0000,0.00
00,0.0000,0.0000,0.0000,0.0000,0.0000,0.0000
'PN2..N5                    :'
0.0000,0.0000,0.0000,0.0000,0.0000,0.0000,0.0000,0.0000,0.0000,0.00
00,0.0000,0.0000,0.0000,0.0000

'PKL2,L3,M2,M3,M4,M5        :'
0.2940,0.5641,0.0428,0.0829,0.0003,0.0159
'PL1M2,M3,M4,M5             :'     0.3587,0.5022,0.0000,0.1392
'PL2M1,PL2M2,PL2M3,PL2M4,M5 :'
0.0455,0.0000,0.0000,0.9545,0.0000
'PL3M1,PL3M2,PL3M3,PL3M4,M5 :'
0.0416,0.0000,0.0000,0.0968,0.8616

'EK,L1..L3,M1..M5           :'      17038.4,  2372.5,  2155.5,
2080.0,   393.6,   312.4,   300.3,   159.6,   157.4
'EN1..N7,O1..O7             :'         45.4,    25.6,    25.6,
2.4,     2.4,     0.0,     0.0,     0.0,     0.0,     0.0,     0.0,
0.0,     0.0,     0.0
'EP1..P5                    :'          0.0,     0.0,     0.0,
0.0,     0.0


''                  NUCLEAR DATA
'PK,PL1,PL2,PM              :'
'PGAM,EGAM (1)              :'
'PIK,PIL1,PIL2,PIL3,PIM (1) :'
'PGAM,EGAM (2)              :'
'PIK,PIL1,PIL2,PIL3,PIM (2) :'
'PGAM,EGAM (3)              :'
'PIK,PIL1,PIL2,PIL3,PIM (3) :'



''                  BETA DECAY

'Endpoint energy                ='            0.
'Mass number                    ='            0.
'Daughter nucl. atomic number   ='            0.
'Forbiddenness                  ='            0
'Shape factor coefficients      ='         0.,0.,0.
```

```
''                  PROCESSES
'WK','WL1','WL2','WL3'
'F12','F13','F23'
'KL1L1','KL1L2','KL1L3','KL1M1','KL1M2','KL1M3','KL1M4','KL1M5'
'KL1N1','KL1N2','KL1N3','KL1O1','KL1O2','KL1O3'
'KL2L2','KL2L3','KL2M1','KL2M2','KL2M3','KL2M4','KL2M5'
'KL2N1','KL2N2','KL2N3','KL2O1','KL2O3','KL2N5'
'KL3L3','KL3M1','KL3M2','KL3M3','KL3M4','KL3M5'
'KL3N1','KL3N2','KL3N3','KL3N4','KL3N5','KL3O1','KL3O2','KL3O3'
'KM1M1','KM1M2','KM1M3','KM1N1','KM1N2','KM3N3'
'KM2M3','KM2N1','KM2N3'
'KM3M3','KM3M4','KM3M5','KM3N1','KM3N2','KM3N3'

'L1L2M1','L1L2M2','L1L2M3','L1L2M4','L1L2M5'
'L1L2N1','L1L2N2','L1L2N3','L1L2N4','L1L2N5','L1L2N6','L1L2N7','L1L
2O1','L1L2O2','L1L2O3','L1L2O4','L1L2O5','L1L2O6','L1L2P1','L1L2P2'
,'L1L2P3'
'L1L3M1','L1L3M2','L1L3M3','L1L3M4','L1L3M5'
'L1L3N1','L1L3N2','L1L3N3','L1L3N4','L1L3N5','L1L3N6','L1L3N7','L1L
3O1','L1L3O2','L1L3O3','L1L3O4','L1L3O5','L1L3O6','L1L3O7','L1L3P1'
,'L1L3P2','L1L3P3'

'L1M1M1','L1M1M2','L1M1M3','L1M1M4','L1M1M5'
'L1M1N1','L1M1N2','L1M1N3','L1M1N4','L1M1N5','L1M1N6','L1M1N7','L1M
1O1','L1M1O2','L1M1O3','L1M1O4','L1M1O5','L1M1P2'
'L1M2M3','L1M2M4','L1M2M5','L1M2N1','L1M2N4','L1M2N5','L1M2N7','L1M
2O1','L1M2O5'
'L1M3M3','L1M3M4','L1M3M5','L1M3N1','L1M3N3','L1M3N4','L1M3O1'
'L1M4M4','L1M4M5','L1M4N1','L1M4N2','L1M4N3','L1M4N4','L1M4N5','L1M
4N6','L1M4N7','L1M4O1','L1M4O5'
'L1M5M5','L1M5N1','L1M5N2','L1M5N3','L1M5N4','L1M5N5','L1M5N6','L1M
5N7','L1M5O1','L1M5O2','L1M5O4','L1M5O5'
'L1N1N1','L1N1N2','L1N1N3','L1N1N4','L1N1N5','L1N1O3','L1N2N5','L1N
3O1','L1N4N5','L1N5N5'

'L2L3M4','L2L3M5','L2L3N1','L2L3N2','L2L3N3','L2L3N4','L2L3N5','L2L
3N6','L2L3N7','L2L3O1','L2L3O2','L2L3O3','L2L3O4','L2L3O5','L2L3P2'

'L2M1M1','L2M1M2','L2M1M3','L2M1M4','L2M1M5','L2M1N2','L2M1N3','L2M
1N4','L2M1O2'
'L2M2M2','L2M2M3','L2M2M4','L2M2M5'
'L2M2N1','L2M2N2','L2M2N3','L2M2N4','L2M2N5','L2M2N6','L2M2N7','L2M
2O1','L2M2O2','L2M2O3','L2M2O4','L2M2O5','L2M2P2'
'L2M3M3','L2M3M4','L2M3M5','L2M3N1','L2M3N2','L2M3N3','L2M3N4','L2M
3N5','L2M3O2','L2M3O4'
'L2M4M4','L2M4M5','L2M4N1','L2M4N2','L2M4N3','L2M4N4','L2M4N5','L2M
4N6','L2M4N7','L2M4O2','L2M4O3','L2M4O4','L2M4O5'
'L2M5M5','L2M5N2','L2M5N3','L2M5N4','L2M5N5','L2M5N6','L2M5O2','L2M
5O4'
'L2N1N2','L2N2N2','L2N2N3','L2N2N4','L2N2N5','L2N2O2','L2N2O3','L2N
3N4','L2N3O2','L2N4N4','L2N4N5'

'L3M1M1','L3M1M2','L3M1M3','L3M1M4','L3M1M5','L3M1N3','L3M1N4','L3M
1N5','L3M1N7','L3M1O3'
'L3M2M3','L3M2M4','L3M2M5','L3M2N3','L3M2N5','L3M2N7','L3M2O3'
'L3M3M3','L3M3M4','L3M3M5','L3M3N1'
```

```
'L3M3N2','L3M3N3','L3M3N4','L3M3N5','L3M3N6','L3M3N7','L3M3O1','L3M
3O2','L3M3O3','L3M3O4','L3M3O5'
'L3M4M4','L3M4M5','L3M4N1','L3M4N2','L3M4N3','L3M4N4','L3M4N5','L3M
4N6','L3M4N7','L3M4O3','L3M4O5'
'L3M5M5','L3M5N1','L3M5N2','L3M5N3','L3M5N4','L3M5N5','L3M5N6','L3M
5N7','L3M5O2','L3M5O3','L3M5O4','L3M5O5'
'L3N1N3','L3N2N3','L3N2N5','L3N3N3','L3N3N4','L3N5N5','L3N3O3','L3N
4N5','L3N5N5','L3N5N6','L3N5N7','L3N5O3','L3N5O4','L3N5O5'

'M1M2M4','M1M2M5','M1M2N1','M1M2N2','M1M2N3','M1M2N4','M1M2N5','M1M
2N6','M1M2O1','M1M2O2','M1M2O3','M1M2O5','M1M3M4','M1M3M5','M1M3N1'
,'M1M3N2','M1M3N3','M1M3N4','M1M3N5
','M1M3N6','M1M3O1','M1M3O2','M1M3O3'
'M1M4M4','M1M4M5','M1M4N1','M1M4N4','M1M4N5','M1M4N6','M1M5M5','M1M
5N1','M1M5N3','M1M5N4','M1M5N5','M1M5N6','M1N1N4','M1N1N5','M1N1N6'
,'M1N5N6','M1N6N6'

'M2M3N4','M2M3N5','M2M3N6','M2M3O1','M2M3O2','M2M3O3','M2M3O4','M2M
3O5','M2M4M4','M2M4M5','M2M4N1','M2M4N2','M2M4N3','M2M4N4','M2M4N5'
,'M2M4N6','M2M4O1','M2M4O2','M2M4O3
','M2M4O4','M2M4O5'
'M2M5M5','M2M5N1','M2M5N2','M2M5N3','M2M5N4','M2M5N5','M2M5N6','M2M
5O1','M2M5O2','M2N1N2','M2N2N2','M2N2N3','M2N2N4','M2N2N5','M2N2N6'
,'M2N3N6','M2N6N6'

'M3M4M4','M3M4M5','M3M4N1','M3M4N2','M3M4N3','M3M4N4','M3M4N5','M3M
4N6','M3M4O1'
'M3M5M5','M3M5N1','M3M5N2','M3M5N3','M3M5N4','M3M5N5','M3M5N6','M3M
5O1','M3M5O2','M3M5O3','M3M5O4','M3M5O5','M3N1N3','M3N2N3','M3N3N3'
,'M3N3N4','M3N3N5','M3N3N6','M3N4N4
','M3N5N6','M3N6N6'

'M4M5N6','M4M5O3','M4M5O4','M4M5O5','M4N1N1','M4N1N2','M4N1N3','M4N
1N4','M4N1N5','M4N1N6','M4N2N2','M4N2N3','M4N2N4','M4N2N5'
'M4N3N3','M4N3N4','M4N3N5','M4N3N6','M4N3O4','M4N4N4','M4N4N5','M4N
4N6','M4N4O1','M4N4O2','M4N4O3','M4N4O4','M4N4O5','M4N5N5','M4N5N6'
,'M4N5O4','M4N6N6','M4N6O4','M4N6O5
'

'M5N1N1','M5N1N2','M5N1N3','M5N1N4','M5N1N5','M5N1N6','M5N2N3','M5N
2N5','M5N3N3','M5N3N4','M5N3N5','M5N3N6','M5N3O5','M5N4N4','M5N4N5'
,'M5N4N6','M5N4O5','M5N5N5','M5N5N6
','M5N5O1','M5N5O2','M5N5O3','M5N5O4','M5N5O5','M5N6N6','M5N6O4','M
5N6O5'

'N1N2N4','N1N2N5','N1N2N6','N1N2O1','N1N2O2','N1N2O3','N1N2O4','N1N
2O5','N1N3N4','N1N3N5','N1N3N6','N1N3O1','N1N3O2','N1N3O3','N1N3O4'
,'N1N3O5'
'N2N4N4','N2N4N5','N2N4N6','N2N4O1','N2N4O2','N2N4O3','N2N5N6','N2N
6O2','N3N4N5','N3N4N6','N3N5N5','N3N5O3','N4N6N6','N5N6N6'

'KL2','KL3','KM2','KM3','KM4','KM5'
'L1M2','L1M3','L1M4','L1M5'
'L2M1','L2M2','L2M3','L2M4','L2M5'
'L3M1','L3M2','L3M3','L3M4','L3M5'

'EK','EL1','EL2','EL3'
'EM1','EM2','EM3','EM4','EM5'
```

```
'EN1','EN2','EN4','EO1','EO2'

'PK','PL1','PL2','PM'
'PGAM_1','EGAM_1'
'PIK_1','PIL1_1','PIL2_1','PIL3_1','PIM_1'
'PGAM_2','EGAM_2'
'PIK_2','PIL1_2','PIL2_2','PIL3_2','PIM_2'
'PGAM_3','EGAM_3'
'PIK_3','PIL1_3','PIL2_3','PIL3_3','PIM_3'

----
DECAY SCHEME
      1    PURE EC
      3    EC-IC/GAMMA
      5    IC/GAMMA
      6    EC-IC/GAMMA-IC/GAMMA
      7    IC/GAMMA-IC/GAMMA
      8    BETA-IC/GAMMA
      9    BETA-IC/GAMMA-IC/GAMMA
     10    PURE BETA
     11    EC-IC/GAMMA-IC/GAMMA-IC/GAMMA
     12    IC/GAMMA-IC/GAMMA-IC/GAMMA
```